DESIGN, ANALYSIS AND PROTOTYPING OF A HIGH SPEED SURFACE MOUNTED PERMANENT MAGNET MACHINE

Prepared by:

Maxas Ng'onga

NGNMAX001

Prepared for:

Professor Mohammed Azeem Khan

Thesis submitted to the Department of Electrical Engineering, University of Cape Town, in complete fulfilment of the requirements for the degree of Master of Science.

August 2018

Department of Electrical Engineering

Faculty of Engineering & the Built Environment

University of Cape Town

Declaration

This dissertation is submitted to the Department of Electrical Engineering, University of Cape Town, in complete fulfilment of the requirements for the degree of Master of Science. It has not been submitted before for any degree or examination at this or any other university. The author confirms that this thesis is based on his own work. Portions of this work have been published in peer-reviewed journals and at refereed international conferences.

"I know the meaning of plagiarism and declare that all the work in the document, save for that which is properly acknowledged, is my own. This thesis/dissertation has been submitted to the Turnitin module (or equivalent similarity and originality checking software) and I confirm that my supervisor has seen my report and any concerns revealed by such have been resolved with my supervisor."

Signed by candidate

M. NG'ONGA

18 August 2018

Acknowledgements

First and foremost, I would like to give thanks to the Almighty God for his continuous grace and mercies throughout this entire journey. The completion of this work would not have been possible without him.

I would also like to extend a special thank you to my family, especially my father and mother who have worked tirelessly to support my education and wellbeing. To you both I owe everything I am today. To my siblings, Daniel and Natasha, thank you for supporting me and cheering me on.

To my supervisor, Professor Azeem Khan, I would like to say thank you for your invaluable guidance throughout the entire project. Your insight into this research work was indispensable.

And to my friends in Cape Town, you became family. Thank you for making my stay in Cape Town nothing short of amazing. I would also like to add a special mention to my colleagues in the AMES research group at the University of Cape Town. Each one of you played a part in realizing this entire project.

To mention everyone who played a part in helping me would be impossible. To those not mentioned, I am grateful and humbled by all the help and support shown.

Abstract

Over the recent years, there has been a rise in the demand for high speed and high power density machines for various applications in industry ranging from basic household power tools to the flight controls for aircrafts in the aerospace sector. There have also been advancements in the power electronics and controls for these machines to deal with the higher operating frequencies. The rise in demand for high speed machines has been driven by the industry's requirement for cost reductions, increased robustness and higher power densities. This thesis aims to contribute to the design and development of a high-speed surface mounted permanent magnet machine.

A numerical procedure for the detailed sizing of a high-speed surface mounted permanent magnet (SPM) machine is outlined in this dissertation. An analytical per phase model is formulated to examine the performance parameters of the machine. The analytical model is validated against results obtained from Ansys Electromagnetics Finite Element Analysis (FEA) software.

The estimation of core losses in high-speed machines is also of critical importance during electromagnetic design. An immense amount of research has been conducted on the estimation of core losses in machines. However, not much has been done to cover the estimation of high-speed core losses as compared to the traditional low-speed machines.

As part of the development of the high-speed machine, the numerical estimation of the high-speed core losses was examined and validation performed using FEA software. On average, there was a difference of about 3-11% between the analytical results and FEA results of the eddy current loss and hysteresis loss. These results demonstrate that the analytical method used to estimate core losses is reasonably accurate when compared to FEA results obtained from ANSYS Maxwell.

The prototyping of a high-speed surface mounted permanent magnet machine is investigated. Focus is placed on the major components of the machine whilst highlighting the use of precision machining and the need to maintain high accuracy during manufacturing and assembly of the machine prototype.

Contents

Declaration ... ii

Acknowledgements ... iii

Abstract ... iv

1 Introduction ... 1

1.1 Background ... 1

1.2 Literature Review ... 3

1.2.1. Competing Topologies for High Speed Applications ... 6

1.2.2. Other Topologies for High Speed Applications ... 9

1.2.3. Applications ... 11

1.2.4. Materials ... 15

1.2.5. Bearings ... 18

1.2.6. Thermal Challenges ... 21

1.2.7. Cooling of High Speed Machines ... 23

1.3 Research Questions and Objectives ... 24

1.4 Dissertation Overview and Contributions ... 25

1.5 Limitations ... 26

1.6 Structure ... 27

2 Topology Selection ... 28

2.1 Radial Flux versus Axial Flux PM Machines ... 28

2.2 Selection of Design Topology ... 32

3 Material Selection and Machine Sizing ... 33

3.1 Material Selection ... 33

3.2 Winding Design ... 37

3.3 Machine Sizing ... 39

3.4 Magnet Dimensions ... 41

3.5 Stator Dimensions ... 42

3.6 Rotor Retaining Sleeve Dimensions ... 44

3.7 Design Parameters ... 46

4 Analytical Model of High Speed PM Machine 47
4.1 Analytical Model of High Speed PM Machine 47
4.1.1. Flux Density 48
4.1.2. Excitation Voltage 50
4.1.3. Synchronous Reactance 52
4.1.4. Armature Resistance 53
5 Finite Element Analysis 55
5.1 Distribution of Flux Density within Generator 57
5.2 Phasor Study – Operation in DQ Plane 60
5.2.1. Current Excitation 60
5.3 Electromagnetic Performance 64
5.3.1. Torque 64
5.3.2. Voltage and Current 65
5.3.3. Machine Losses 66
5.3.4. Output Power 67
5.3.5. Comparison of analytical and simulated results 68
6 Iron Loss Modeling 70
6.1 Overview of Iron Losses 70
6.2 Iron Loss Model Review and Analysis 71
6.2.1. Original Steinmetz's Two-Term Model 71
6.2.2. Modified Steinmetz's Two-Term Model 74
6.2.3. Bertotti's Three-Term Model 76
6.3 Estimation of Core Loss in a Machine 79
6.3.1. Tooth Eddy Current Loss Model 80
6.3.2. Simplified Tooth Eddy Current Loss Model 83
6.3.3. Effect of Machine Dimensions on Tooth Loss 84
6.3.4. Circumferential Component of Flux Density on Eddy Current Loss 89
6.3.5. Yoke Eddy Current Loss Model 92
6.3.6. Effect of Machine Dimensions on Yoke Eddy Current Loss 94
6.3.7. Hysteresis Loss Model 98
7 Prototyping of the High Speed SPM Machine 100
7.1 Stator and Rotor Laminations 101
7.2 Stator Winding 102

7.3 Machine Shaft **103**
7.4 Housing Structure **105**
8 Prototype Testing **107**
8.1 Stator Winding Coils **107**
8.1.1. Open Circuit Voltage 108
9 Conclusions and Recommendations **110**
9.1 Conclusions **110**
9.2 Recommendations **111**
References **113**
Appendix A **122**
Appendix B **123**
Assessment of Ethics in Research Projects **128**

List of Figures

Figure 1-1: Global New Investment in Renewable Energy ($bn) 2004-2015 1

Figure 1-2: Layout of CHP system [2] 2

Figure 1-3: Summary of machine topologies recorded for HS applications [4] 3

Figure 1-4: Existing HS machines in literature [11]–[16] 5

Figure 1-5: Induction machine rotor structures [21] 6

Figure 1-6: Rated powers and speeds of existing high-speed machines [25] 8

Figure 1-7: Cutaway view of microturbine [36] 11

Figure 1-8: Comparison of core loss and yield strength for different high-performance electrical steels [18] 15

Figure 1-9: Bearings used for high-speed machines [51] 19

Figure 1-10: Typical layout of SPM rotor [61] 21

Figure 2-1: Axial Flux PM Machine Configuration [67] 29

Figure 2-2: AFPM machine topologies 29

Figure 2-3: Radial Flux Machine Configurations 30

Figure 3-1: Machine dimensions [66] 42

Figure 4-1: Per-phase equivalent circuit model 47

Figure 5-1: FEA Electrical Circuit 55

Figure 5-2: 2D Model of SPM Machine 56

Figure 5-3: No load airgap flux density 57

Figure 5-4: No Load Stator tooth flux density waveforms 58

Figure 5-5: No Load Stator yoke flux density waveforms 58

Figure 5-6: Phasor diagram (motor mode) 61

Figure 5-7: Torque vs. current angle 61
Figure 5-8: Winding currents & induced EMF waveforms 62
Figure 5-9: 3D FEA - Torque vs. time 64
Figure 5-10: Induced phase voltage vs. time 65
Figure 5-11: Phase currents vs. time 65
Figure 5-12: 3D Loss plot 66
Figure 5-13: Output power vs. time 67
Figure 6-1: Iron loss vs. Flux density 72
Figure 6-2: Iron loss vs. flux density at two frequencies 73
Figure 6-3: Steinmetz model comparison at 200 Hz and 1000 Hz 75
Figure 6-4: Bertotti's three-term model comparison at 200 Hz and 1000 Hz 77
Figure 6-5: Bertotti vs. Steinmetz's model at 200 Hz and 1000 Hz 78
Figure 6-6: Linear PM motor flux distribution [89] 79
Figure 6-7: Movement of flux lines in SPM 80
Figure 6-8: Radial flux density waveform in tooth 81
Figure 6-9: Tooth flux density for varying slot opening widths 84
Figure 6-10: Tooth eddy current loss vs. slot opening width 85
Figure 6-11: Radial flux density in tooth for varying pole-arc 86
Figure 6-12: dB/dt vs. magnet pole-arc 87
Figure 6-13: Correction factor k_q - varying magnet thickness and airgap height 88
Figure 6-14: Correction factor k_c for varying slot closure [89] 90
Figure 6-15: Circumferential flux density in stator yoke 92
Figure 6-16: Flux density in stator yoke for varying pole embrace 95
Figure 6-17: Radial flux density in Stator yoke 96

Figure 7-1: Assembled rotor core 101

Figure 7-2: Stator winding 102

Figure 7-3: Machine shaft 103

Figure 7-4: Complete rotor with shaft & retaining sleeve 103

Figure 7-5: Dynamic balancing of shaft 104

Figure 7-6: Housing structure 105

Figure 7-7: Pressure testing of housing structure 106

Figure 8-1: Open circuit voltage waveform and fft 108

Figure 8-2: Induced EMF vs. rotational speed 109

Figure A-1: Stator slots (a) open rectangular slot (b) semi-closed rectangular slot (c) semi-closed trapezoidal slot (d) semi-closed oval slot (e) semi-closed oval slot for internal stators (f) semi-closed round slot 122

Figure B-1: Shaft assembly 123

Figure B-2: Rotor laminations 124

Figure B-3: Stator laminations 125

Figure B-4: HS Machine Prototype – Drawing Section 126

Figure B-5: CHP System Dimensions 127

List of Tables

Table 1-1: Summary of Applications for HS machines in the automotive industry. 13

Table 1-2: Pros and cons of different bearing types [51]..... 18

Table 1-3: Comparison of cooling methods..... 23

Table 2-1: Advantages and disadvantages of SPM machines 31

Table 2-2: Comparison of RFPM and AFPM topologies 32

Table 3-1: Classification of materials for HS applications..... 33

Table 3-2: Properties of laminated steel 34

Table 3-3: Selected NdFeB magnet properties 35

Table 3-4: Slot/Pole Combination for 4 Pole Design 37

Table 3-5: Design parameters for estimation of l/D ratio 40

Table 3-6: Stress on retaining sleeve for different thicknesses..... 45

Table 3-7: Initial design parameters 46

Table 5-1: Comparison of analytical and FEA results..... 68

Table 6-1: Approximation of waveform rise time 82

Table 6-2: Approx. Tooth Eddy Current Loss at 1000Hz 91

Table 6-3: Effect of variation of slot opening width on circumferential flux density 94

Table 6-4: Eddy current loss - stator yoke..... 97

Table 6-5: Comparison of Hysteresis loss model with FEA..... 98

Table 6-6: Comparison of overall core loss using analytical model..... 99

Table 8-1: Comparison of PM flux linkage 109

List of Abbreviations

AFPM	Axial Flux Permanent Magnet
CHP	Combined Heat and Power
CNC	Computer Numerical Control
d-axis	Direct axis
Dy	Dysprosium
EMC	Electro Chemical Machining
FEA	Finite Element Analysis
FFT	Fast Fourier Transform
HS	High Speed
HSEM	High Speed Electrical Machines
IM	Induction Machines
IPM	Interior Permanent Magnet
MMF	Magneto Motive Force
NdFeB	Neodymium-Iron-Boron
PM	Permanent Magnet
q-axis	Quadrature axis
QC	Quality Control
RFPM	Radial Flux Permanent Magnet
SF	Safety Factor
SiFe	Silicon-Iron
SmCo	Samarium-Cobalt
SPM	Surface Permanent Magnet
SR	Switched Reluctance
SyR	Synchronous Reluctance

List of Symbols

Symbol	Unit	Definition
a		Number of parallel paths
A_{cond}	m^2	Cross sectional area of a single conductor
A_g	m^2	Airgap area
A_m	A/m	Electric loading
A_m	m^2	Magnet area
A_s	m^2	Slot area
B_{1max}	T	Peak value of fundamental harmonic of flux density
B_g	T	Airgap flux density
BH_{max}	kJ/m^3	Energy Product
B_{mg}	T	Magnetic loading
B_r	T	Remanence flux density
B_{sy}	T	Stator yoke flux density
B_t	T	Tooth flux density to avoid saturation
C		Rated load of bearing
C_ϕ		Flux concentration factor
D	m	Stator inner diameter
D_{1in}	m	Rotor diameter
d_{sht}	m	Height of stator tooth fillet
Ea	V	Induced voltage
E_f	V	Fundamental value of induced voltage (RMS)
Ɛ		Ratio of induced EMF to input voltage
f	Hz	Frequency
g	m	Airgap height
g_e	m	Effective airgap length
H_c	kA/m	Coercivity
h_m	m	Magnet height
h_s	m	Slot height
h_{sy}	m	Stator yoke height
I	A	Current

Symbol	Unit	Definition
L_{10}	rev	Ball bearing lifetime
l_{ph}	m	Total length of phase winding
L_s	H	Synchronous inductance
N_{rev}	rev	Base revolution number
n_s	rev/min	Synchronous speed
N_s		Number of slots
P	N	Applied load
p		Number of pole pairs
P	W	Power
PC		Permeance coefficient
P_{gen}	W	Airgap apparent power
q		Number of slots per pole per phase
r	m	radius of round wire
R_{ac}	Ω	AC armature resistance
R_{dc}	Ω	DC armature resistance
R_{ro}	m	Rotor outer radius
R_{si}	m	Stator inner radius
R_{so}	m	Stator outer radius
S_{elm}	W	Airgap electromagnetic power
T	Nm	Torque
T_c		Turns per coil
T_{ph}		Turns per phase
w_s	m	Slot width
W_{sy}	m	Width of stator yoke
W_{tb}	m	Width of tooth body
X_l	Ω	Leakage reactance
X_m	Ω	Magnetizing reactance
X_s	Ω	Synchronous reactance
α		Pole arc to pole pitch ratio
δ	m	Skin depth
$\lambda_{end\ winding}$		End winding permeance coefficient
λp	m	Pole pitch

Symbol	Unit	Definition
λs	m	Slot pitch
λ_{slot}		Slot leakage permeance coefficient
$\lambda_{tooth\text{-}top}$		Tooth-top permeance coefficient
μ		Permeability
μ_0		Permeability of free space
μ_r		Recoil permeability
ρ	Ωm^{-1}	Resistivity
σ_{cu}	S/m	Conductivity of copper
$\boldsymbol{\tau}_c$		Coil pitch
ϕ_p	Wb	Flux per pole
ω	rad/s	Angular frequency

Chapter 1

1 Introduction

1.1 Background

It is undoubtedly evident that power, as obtained from the various energy sources, drives economic development and is key in enhancing human progress. The growing environmental concerns as a result of emissions produced from power generation have resulted in an emphasis on the use of "green" energy sources. This has seen an increase in investments in wind, solar as well as biomass technologies. According to [1], global investments in renewables has seen a rise of about 5% over the last five years to $285.9 billion, which is more than six times the figure set in 2004. In terms of gigawatts capacity added as of 2015, about 53.6% of the entire power generation capacity came from renewable energy sources (excluding hydro-power) commissioned that year.

Figure 1-1 below shows the investments in renewables compiled by UNEP and Bloomberg New Energy Finance [1];

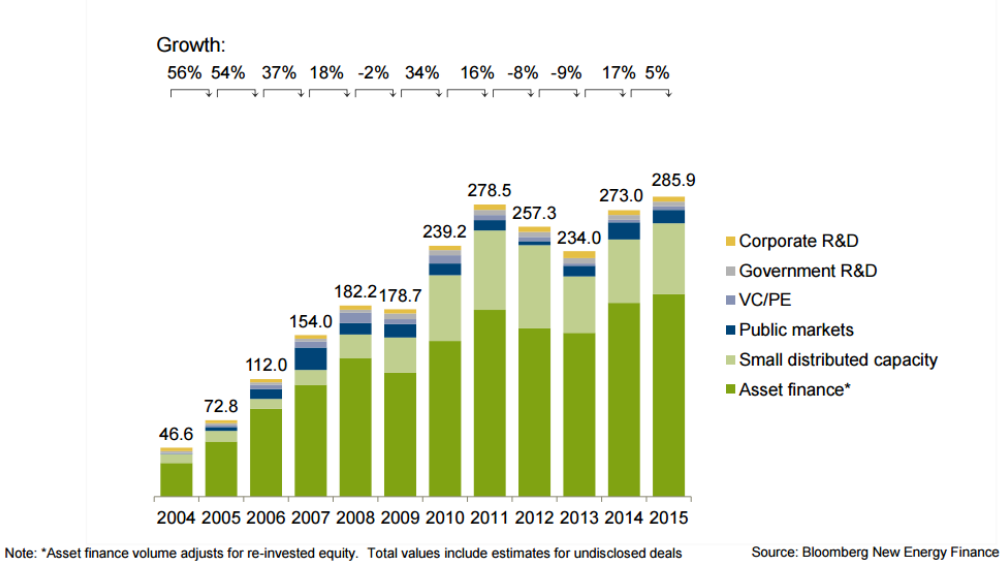

Figure 1-1: Global New Investment in Renewable Energy ($bn) 2004-2015

Another solution to the rising global power demands has been to produce energy more efficiently. This has led to the realization of High Speed (HS) and high power density machines for use in various sectors ranging from basic household power tools to microturbines in Combined Heat and Power (CHP) systems.

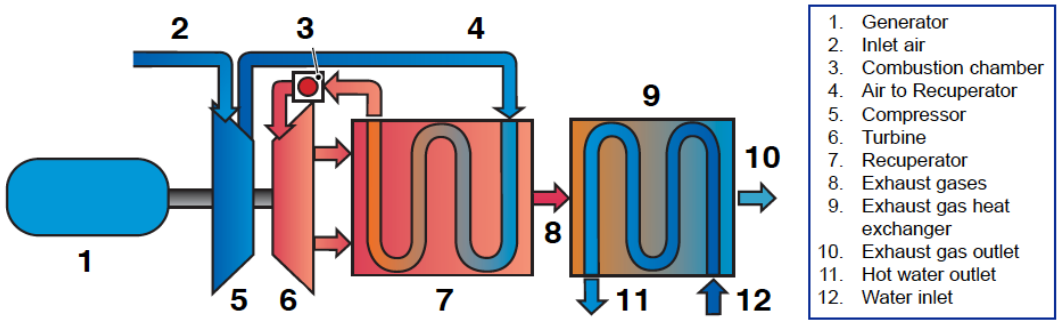

Figure 1-2: Layout of CHP system [2]

These machines offer numerous advantages such as smaller size, light weight, easy maintenance as well as high torque and power density [3]. In addition, high speed machines have also displayed higher robustness, higher efficiencies and significant cost reductions as compared to the traditional low speed machines with gearboxes. This has been fuelled by advancements in materials, power-electronic devices, control methods etc. [4].

However, there are still challenges that exist in the development of High Speed Electrical Machines (HSEM). Several papers in literature have reviewed the design and analysis of HSEMs but very few of these have actually considered the challenges in the development of these machines. Some of these challenges include but are not limited to; high frequency losses i.e. core and copper losses, friction and windage losses, bearing selection, cooling and rotor dynamics [5]. For high operating speeds, the machine sizes become smaller resulting in a lower thermal mass. And as such, removal of heat from within the machine becomes a huge challenge. Therefore, an effective cooling system must be considered during the design to facilitate operation at high speeds without the risk of catastrophic failure [6].

1.2 Literature Review

Over the recent years, there has been a rise in the demand for high speed and high power density machines for various applications in industry ranging from basic household power tools to the flight controls for aircrafts in the aerospace sector. The aerospace sector has attracted even more attention through the increased use of unmanned aerial vehicles (UAVs) for various applications such as data acquisition, search and rescue, forest fire detection etc. [7]. The increase in demand for high speed machines has been driven by the industry's requirement for cost reductions, increased robustness and reduced weight but to mention a few. This has also seen advancements in the power electronics and controls for these machines to deal with the high operating frequencies. Other applications for high speed machines include turbo compressors, pumps, small power plants and energy storage flywheels.

The HS topology selection largely depends on the type of application as well as the required speed and output power. Topologies recorded in literature for high speed applications include; Permanent Magnet (PM) Machines, Induction Machines (IM), Synchronous Machines, Switched Reluctance (SR) Machines, Claw Pole Machines, Homo-Polar Machines and Synchronous Reluctance (SyR) Machines [4].

A graph displaying prototyped and/or manufactured high speed machine topologies is shown below in Figure 1-3;

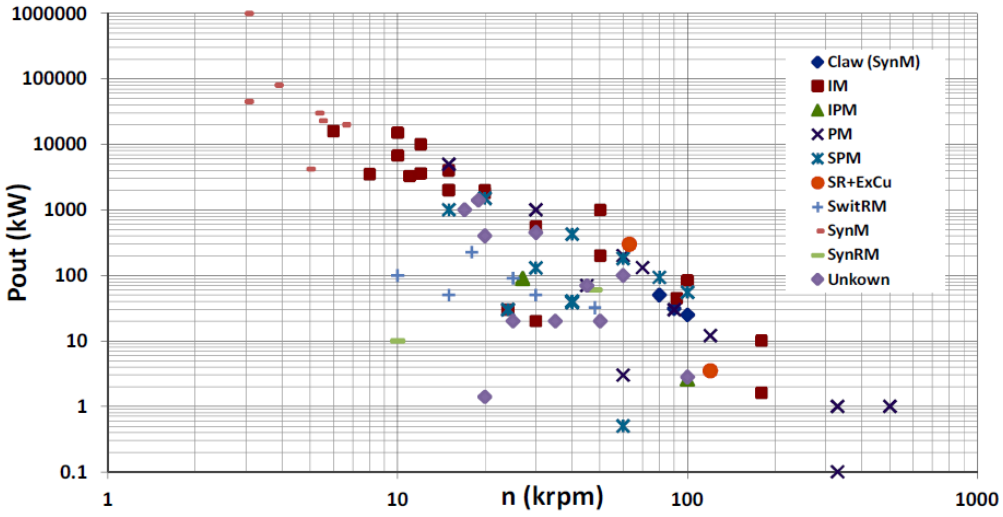

Figure 1-3: Summary of machine topologies recorded for HS applications [4]

PM machines have shown more success in most aspects i.e. power density and efficiency. In addition, the cost of permanent magnets has significantly reduced over the years, allowing the realization of PM machines in more demanding sectors like aerospace and military [8].

HS machines are limited by physical parameters and thermal limits. The physical parameters i.e. centrifugal forces and rotor dynamics associated with machines at such high speeds become the breaking point for design. This would determine how fast the machine can be allowed to operate safely without any damage to the components. With the reduced size of the machine, cooling becomes another consideration during the design stage as it becomes more challenging to avoid demagnetization [9]. This is due to a reduction in the cooling surface area for delivery of the same power.

The limitations of high speed machines is a topic that is still being carefully considered by researchers. According to [10], the problem is that most of the research being done on the limitations of HS machines is focused on particular examples that have either already been published or a specific challenge speed and or power. [10] also records that a majority of research papers on the limits of high speed machines has only focused on the electrical constraints thereby giving an incomplete investigation into the practical mechanical limits of high speed machines.

Figure 1-4 shows existing high-speed machines plotted against their rotational speeds [11]–[16]. The graph is based on machines that have been designed and prototyped successfully.

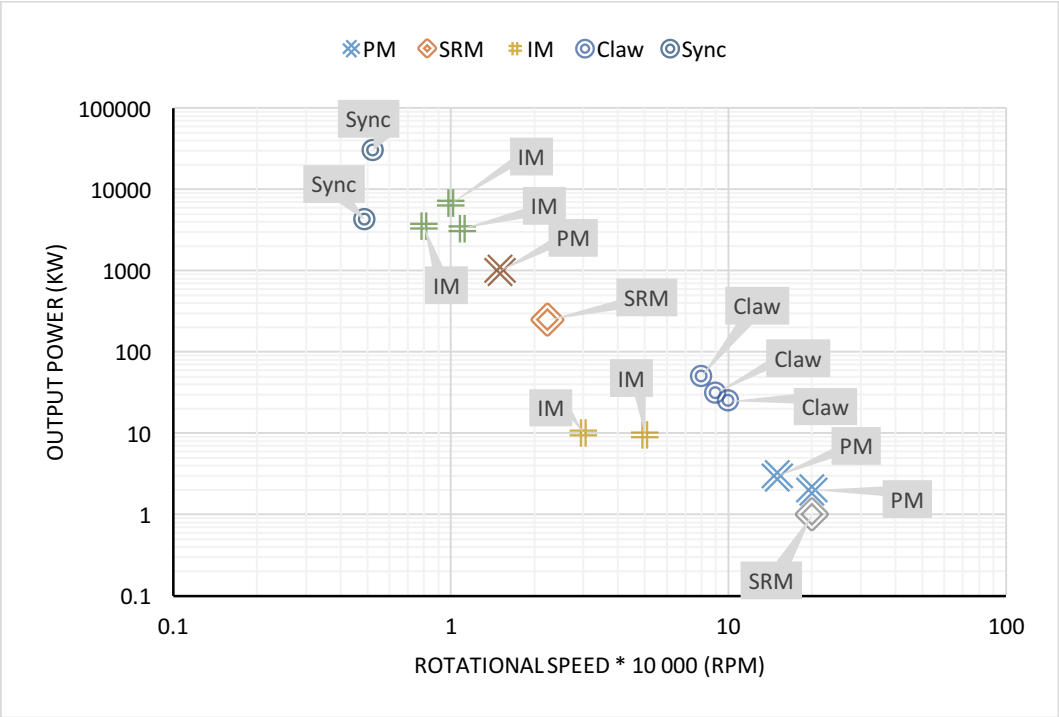

Figure 1-4: Existing HS machines in literature [11]–[16]

From Figure 1-4, it can be observed that possible rotational speeds begin to decrease at high output power. According to [16], high speed machines are under a power limit and this numerical limit can be obtained as proposed in [17].

There are various factors that limit the advancement of high speed electrical machines i.e. electromagnetic, mechanical and thermal constraints. It should be noted that these constraints will differ depending on the machine topology. These are discussed later in this chapter.

1.2.1. Competing Topologies for High Speed Applications

As mentioned in the previous section, the selection of a suitable topology primarily depends on the type of application, required output power and operational speed of the machine. Of the various topologies that have been reviewed from literature, the induction machine and the permanent magnet machine show clear dominance in high speed applications. In particular, the PM machine was seen as suitable for higher speed, low power applications whereas the IM was favourable for lower speeds and higher power applications [18]. According to [19], permanent magnet machines limited to applications where the required surface speed of the rotor does not exceed 250 m/s.

a. High-Speed Induction Machines

Due to their robust construction, the solid rotor induction machines are preferred over permanent magnet machines for applications where higher power and speeds are required. [20] records that the smooth solid rotor design is the most robust but still proves inefficient as the design exhibits low conductivity paths for the induced rotor currents. Other designs of induction machines include the slitted solid rotor, coated solid rotor and caged solid rotor.

Figure 1-5 below shows the different rotor designs of induction machines;

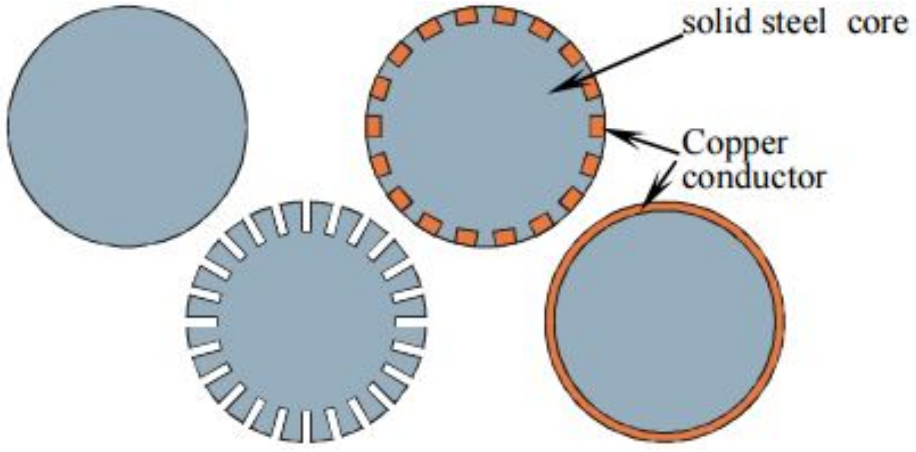

Figure 1-5: Induction machine rotor structures [21]

The coated solid rotor design is an improvement over the standard solid rotor design. This improvement features a coated copper layer over the rotor providing enhanced

mechanical robustness and higher efficiency [18]. The axially slitted solid rotor induction machine as the name suggests, has its rotor surface slitted axially. This enables the fundamental flux component to be guided into the rotor and also provides a path of high resistance for the eddy currents travelling on the rotor surface [18]. Lastly, the caged solid rotor displays a blend of features from the solid rotor topology and squirrel cage rotor topology. With this rotor topology, [22] reports higher efficiency levels and utilization factor compared to the copper coated solid rotor topology.

A further comparative study by [21] concludes that from the four topologies of induction machines for high speed applications, the order of preference in terms of mechanical performance is solid rotor induction machine, slitted solid rotor induction machine, solid rotor with coated conducting sheet induction machine and finally, solid cage rotor induction machine. But in terms of electromagnetic performance, the result is reverse with the first choice being the solid cage rotor induction machine.

b. High-Speed Permanent Magnet Machines

High-speed permanent magnet machines have become popular over the years for use in high speed applications due to their high efficiency levels and various configurations have been designed, tested and built. The two topologies with extensive usage in high speed applications are the Interior Permanent Magnet (IPM) machine and the Surface Permanent Magnet (SPM) machine.

From [18], it is clear that the surface mounted permanent magnet machines are dominant in industry with evidence from the various technical papers reviewed. The dominance of SPM machines can be attributed to the fact that the SPM machines show a greater robustness over other configurations such as the IPM machines, as the use of the sleeve proves to be better at retaining magnets at high speeds than embedding them in the rotor as with IPM machines [23].

Research conducted by [19] suggests that the use of IPM machines in high speed applications is limited primarily by mechanical constraints. It is due to the strength of conventional electrical steels that these machines are limited to surface speeds less than 80m/s. However, [24] proved that by using high-strength electrical steels, it is possible to achieve peripheral speeds in excess of 230m/s in IPM machines.

Figure 1-6 shows the rated powers and speeds of high speed machines; comparing permanent magnet machines to induction machines.

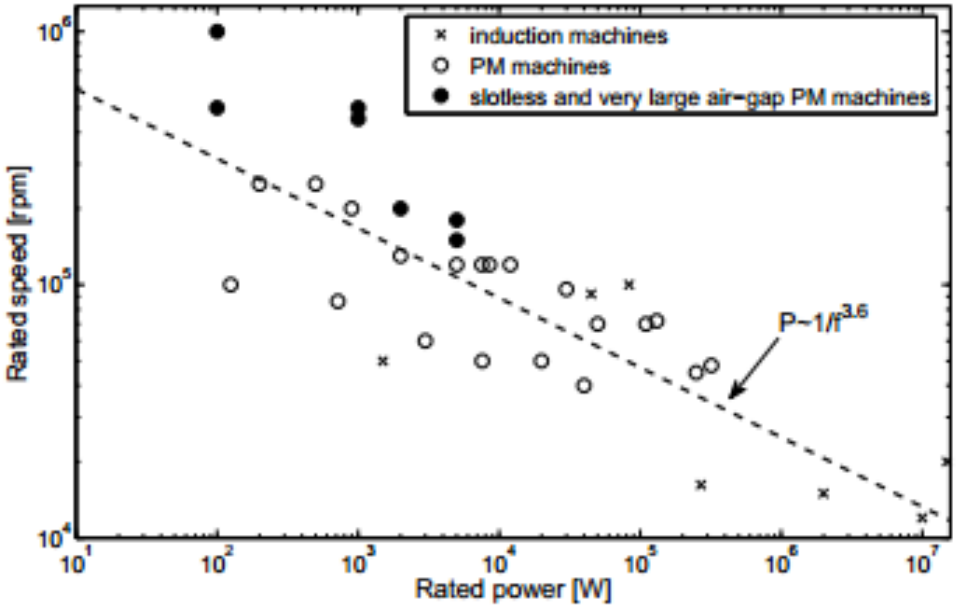

Figure 1-6: Rated powers and speeds of existing high-speed machines [25]

1.2.2. Other Topologies for High Speed Applications

The less common topologies used for high speed applications include; the Switched Reluctance machine, Synchronous Reluctance machine and the Synchronous Homopolar machine.

a. Switched Reluctance Machines

Although induction and PM machines are the preferred choices for most high speed applications, switched reluctance machines boast numerous advantages such as fault tolerance, robustness and low cost [26]. According to [27], SR machines are able to operate under the loss of one phase and display better fault tolerance in designs with more than three phases. It is due to this reason that SR machines are favoured in the aerospace industry. On the other hand, major drawbacks such as vibration, noise, drive topology and torque ripple hinder the use of SR machines for less specific applications [26].

b. Synchronous Reluctance Machines

The rotor and stator of synchronous reluctances machines are constructed in a similar way to the traditional IPM machines. The difference is that SyR machines are completely free of magnets. This makes them inexpensive to manufacture and capable of operating at much higher temperatures and speeds than PM machines [28]. The advantages of SyR machines are similar to those of SR machines as discussed earlier except that SyR machines possess lower torque ripple and can operate from simple P.W.M converters [28].

However, the use of SyR machines in high-speed applications is usually discouraged due to their low structural integrity caused by the presence of multiple flux barriers [29]. [29] further suggests that for speeds over 70 krpm, the performance of SyR machines significantly reduces due to structural limitations. In [30], a 100 kW 20,000 rpm motor with novel rotor was built and tested using a new mechanically robust construction technique. A few other examples of HS SyR machines presented in literature include; a 10 kW 10,000 rpm machine [31], 20 kW 20,000 rpm machine [32] and a 5 kW 50,000 rpm machine in [33].

c. Synchronous Homopolar Machines

Synchronous homopolar machines have been adopted for use mainly in high-speed flywheel energy storage systems. They are similar to the wound-field synchronous machine with the only difference being that the field winding is fixed to the stator rather than the rotor. This allows for simplified rotor construction, elimination of slip rings and better cooling of the field winding [34]. Research is still being conducted on the design and development of synchronous homopolar machines for HS applications. A 30 kW 100,000 rpm machine was designed, constructed and tested in [34]. [35] proposed an 8 kW 60,000 rpm machine for use in a flywheel energy storage system. [34] also suggests the development of a homopolar machine with a slotless stator thereby eliminating slotting induced rotor losses and also allowing the realization of higher airgap flux densities.

1.2.3. Applications

Increasing attention has been given to the use of high speed permanent magnet machines in a wide range of application such as micro gas turbines, aircraft and drone generators, dental drilling tools, pumps, compressors and airborne radars in the military industry.

a. Microturbines

A microturbine consists of a single-shaft turbine coupled with a high-speed electric generator. Other components include; turbine compressor, combustor, recuperator and a converter to provide a specific output power. According to [18], microturbines have typical outputs between 30 and 400 kW. They are ordinarily used in sites where space is a constraint as well as in low infrastructure countries [9]. Microturbines are also finding applications in drones and electric aircrafts [7].

Figure 1-7 shows a cutaway view of a microturbine showing the typical arrangement of components.

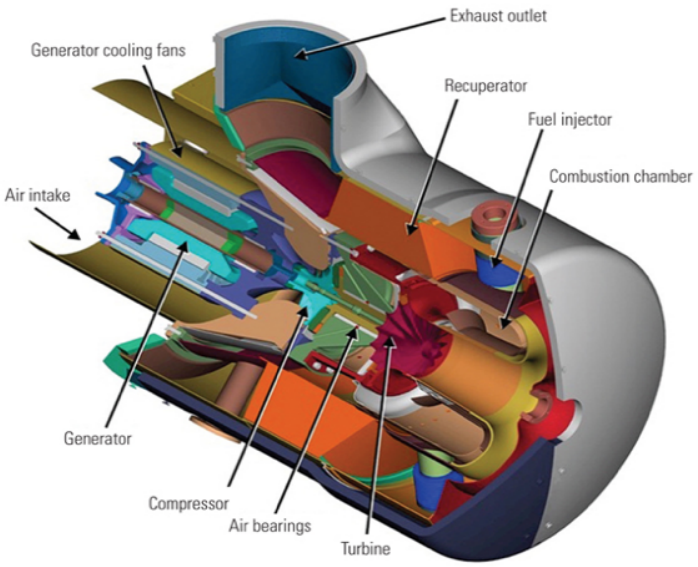

Figure 1-7: Cutaway view of microturbine [36]

With efficiencies of about 20-30%, microturbines alone do not provide attractive investment returns in commercial applications. A solution to this is found in coupling microturbines with combined heat and power systems where heat and exhaust gases can be recovered and effectively used [36], [37].

b. Compressors

Compressors play a vital role in many industrial applications that demand high quality and oil free compressed air. Some examples include; the pharmaceutical industry, food and beverage industry as well as the automotive industry. These specialist applications require uncontaminated air to avoid consumer health hazards and to provide high-quality finishes on products [18]. The main features of compressors include; centrifugal compression, high-speed PM brushless motor, an impeller, oil free bearings, a PWM inverter-fed motor and power electronics [37].

The maximum power and speed of high-speed motors is limited by thermal and mechanical constraints. According to [38], [39], the estimated maximum power of high-speed PM motors for compressor applications is 1.5 MW at 20,000 rpm. The use of direct drive PM motors for compressor applications is preferred as they offer high power densities and efficiencies as well as reduced size [40].

c. Aircraft Generators

Aircraft generators are required to supply the entire aircraft with power during flight. They are driven by the aircraft engines and require high fault tolerance as well as the capability to operate in harsh environments [41]. These generators typically operate from about 7200 to 27000 rpm and output power from 30 to 250 kW [37].

Thermal and environmental considerations also play a vital role in the selection of machine type for this application. [9] suggests that the synchronous reluctance machine proves to be the ideal candidate amongst others such as the PM machine for use in aircraft generators as its thermal capability is only related to the winding insulation. Cooling is achieved using either spray oil cooling or forced air cooling. For very high temperatures, spray oil cooling is one of the most effective methods [37].

d. Automotive

A call for stringent emission requirements and regulations to end the use of internal combustion engines mainly in Europe and China have necessitated the development of hybrid machines in vehicles [42], [43]. In order to meet these requirements, manufacturers have opted to either use complete electrified propulsion systems or hybrid drivetrains which encompass the use of auxiliary electrical systems to boost the efficiency of the combustion engine [9].

Table 1-1 summarizes a few of the applications for high speed machines in the automotive industry as compiled from [9], [18]:

Table 1-1: Summary of Applications for HS machines in the automotive industry

Application description	**Machine type**	**Speed range**	**Power ratings**
• Placed in-between turbine and turbocharger • Used as motor to speed up compressor to required speed avoiding turbo lag • At high engine loads with excess exhaust energy, used as generator	Permanent Magnet	≥18 krpm	20-60 kW
• Installed downstream of the turbo charger • Extracts waste heat from exhaust gases • Energy recovered is supplied to the vehicles electrical loads	Permanent Magnet	50-100 krpm	4-100 kW
• Kinetic Energy Recovery System (Hybrid) • Energy from flywheel rotor is stored in its kinetic form • Storage mechanisms form part of the electrical machine	Permanent Magnet	50-100 krpm	60 kW

e. Flywheel Energy Storage

In a flywheel energy storage system, energy is stored mechanically in a rotating flywheel driven by a motor. The flywheel rotates at speeds greater than 20,000 rpm and offer a number of advantages over battery technologies such as wider operating temperature ranges, increased lifetime and compact size [18].

The more advance flywheel energy storage systems are made of composites providing high strength and light weight. These properties allow for maximum rotational speed and ultra-low friction bearing assemblies that are less costly [37].

f. High-Speed Spindle Applications

The machine tool industry has also contributed to the development of high-speed electrical machines. The speed limits in spindle applications vary from 9,000 to 180,000 rpm with power ranging from 24 kW down to 1 kW [18]. These machines have been developed for dental applications, grinding and ultraprecision machining applications with speeds up to 300,000 rpm.

High-speed spindles offer smooth and constant torque, low vibration levels, speed control and high power density as compared to the traditional low speed spindles [18], [37].

1.2.4. Materials

The increasing availability of new materials has also contributed to further realization of high-speed machines. These new materials have been specifically designed to meet the demands of high-speed electrical machines in mechanical strength as well as electromagnetic performance. The development of these materials has been key in pushing the operational boundaries of high-speed electrical machines.

a. Electrical Steels

The selection of electrical steels is of great importance during the development of high-speed machines. Different silicon alloys have been considered by researchers based on their yield strength, saturation flux densities as well and the amount of core losses. The core losses are primarily influenced by the lamination thickness and final annealing method for a given frequency and flux density [18]. Therefore, thinner laminations would result in much lower core losses.

Figure 1-8 below shows a comparison of different high-performance electrical steels based on their core loss and yield strength.

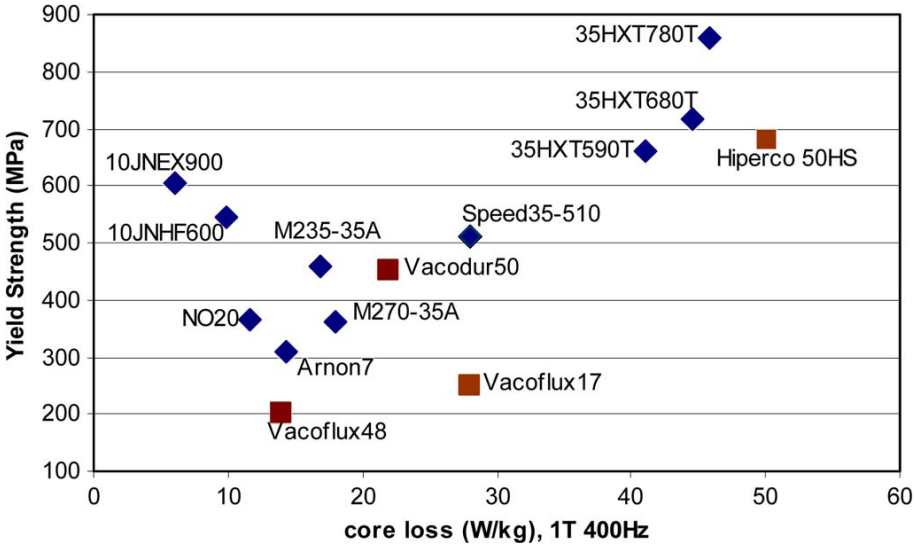

Figure 1-8: Comparison of core loss and yield strength for different high-performance electrical steels [18]

Efforts in developing new materials have increased with the demand for higher speeds in electrical machines. The simplest solution to this has been to increase the silicon

content as in the case of the JNEX10-Core having 6.5% Si content as compared to the conventional silicon steel sheets having a silicon content of 3.5% or less [18]. However, a higher silicon content tends to harden the steel sheet making it brittle and undesirable for punching and for operation at high-speeds.

It is still worth noting that thinner Silicon-Iron (SiFe) grades such as Arnon7 and NO20 with a thickness of 0.17 mm and 0.2 mm respectively are being used for higher frequencies. According to [44], electrical steels as thin as 0.1 mm are commercially available and tailored for high-frequency specialist applications. The use of Amorphous Magnetic Materials (AMMs) has not seen commercial utilization in electric machines as compared to low frequency power transformer applications due to lack of suitable handling methods and economic cutting techniques. This is despite the fact that AMMs display much lower iron losses compared to the traditional silicon steel [45]. However, [46] recently developed a novel tapered rotating electrical machine topology utilizing cut AMM with a maximum operating speed of 7000 rom.

b. Permanent Magnets

High speed operation demands that permanent magnets possess high temperature and mechanical stress capability. Neodymium-Iron-Boron (NdFeB) and Samarium-Cobalt (SmCo) magnets with high-energy-density are preferred for use in high-speed electrical machines. NdFeB grades alloyed with Dysprosium (Dy) allow for operation in temperatures up to 250 °C and for temperatures above this, SmCo remains the only suitable material [18]. However, [9] states that the use of Dysprosium poses some major financial drawbacks due to its rare natural occurrence and use in many other applications. [47] predicts the demand to greatly outweigh the supply which will further increase the price of such a metal in the near future. High-strength metallic materials such as titanium and Inconel have been adopted to ensure mechanical integrity of high-speed rotors. Carbon fibre is often used either as a prefabricated sleeve or pressed onto the assembly for retention of magnets [18].

One other challenge for magnets operating in high-speed environments is the internally generated losses due to flux pulsation as a result of asynchronous fields, air-gap harmonics and stator slotting. A known solution to this has been to segment the magnets axially, radially or circumferentially. [48] also suggests a critical design

trade-off between designing the machine winding and geometry to minimize rotor losses and, subsequently, magnet selection based on temperature capability.

c. Conductors

The selection of conductor material is important so as to minimize AC copper losses. For most high-speed applications, copper litz wire is normally preferred for lower proximity and skin effect losses. Even though copper litz wire is lighter in weight with increased resistivity, it still presents the challenge of poor slot fill factor and jointing with other metals [9]. Pure copper is not typically used in high-speed high temperature applications due to its low yield strength, and it softens at high temperatures [18]. However, there have been efforts into co-extruding copper and aluminium by [49] resulting in a conductor having an aluminium core and copper outer surface. A few advantages include; ease of bonding, improved skin resistance and lighter weight. Further advances in copper alloying have also seen the introduction of high-strength 'High-Copper' alloys and bronzes for use in induction machine rotor cage applications [9].

d. Power Electronic Materials

The realization of high-speed machines has also been supported by developments in research of power electronic materials. High speed machine drives have been plagued by high harmonic induced losses due to the high fundamental frequency flux distributions within the machine. According to [9], SiC, GaN and Diamond continue to attract research attention as enabling technologies in power electronic devices for high switching frequency requirements. [50] forecasts that GaN will be predominantly used in price-driven-markets due to its potentially lower manufacturing cost whilst SiC will be limited to military and aerospace applications.

1.2.5. Bearings

Bearings pose yet another challenge for the implementation of high-speed machines. As the rotational speeds increase, challenges such as friction loss, mechanical strength and reliability become more pronounced. The choices available for high speed machines include ball bearings, static and dynamic fluid bearings, foil bearings or magnetic bearings. Of the aforementioned types of bearings, only the ball bearings have a simpler design process. The rest require more intricate design methods and analysis. Table 1-2 displays a summary of the pros and cons of different bearing types for high-speed machines.

	Bearing Type	Pros	Cons
	Magnetic	No wear Lifetime Controllability	Complexity
	Ball	Small size Availability	Losses Noise Wear, Lifetime
Fluid Bearings	**Static**	Exact positioning Lifetime	External pressure system
	Dynamic	Small size	Instabilities Wear at start/stop
	Foil	Small size	Wear at start/stop Availability

Table 1-2: Pros and cons of different bearing types [51]

One of the major advantages of the other types of bearings over the ball bearing is that they are only subjected to air friction and therefore have no wear. In addition, ball bearings are not suitable for high temperature operations as the increase in friction losses causes a change in the properties of the lubricant and results in destruction of the bearings [51]. Therefore, even though ball bearings may seem to be less complex and easy to implement, designers tend to prefer the other bearing types which are more complex to implement but have lower friction losses.

Figure 1-9 below shows the bearings used for HS machines from published data.

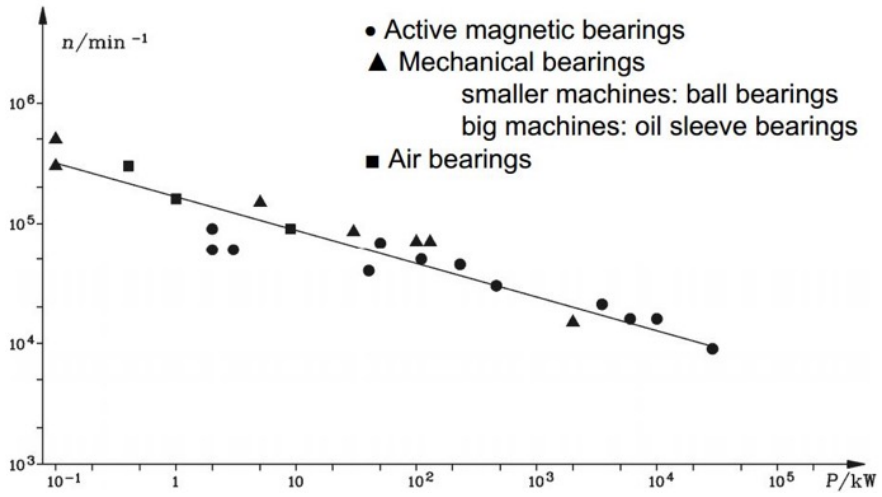

Figure 1-9: Bearings used for high-speed machines [52]

a. Ball Bearings

The ball bearing is the simplest option for high-speed applications. As stated in the previous section, ball bearings have their limitations. The main advantages of ball bearings include simple construction, small size and high robustness [5].

According to [5], the lifetime of ball bearings can be estimated using the equation as presented in (1-1). From interpretation, it can be concluded that the lifetime of ball bearings is highly dependent on load. Doubling the load reduces its life by up to 10 times, while doubling the speed, reduces it by half.

$$L_{10} = \left(\frac{C}{P}\right)^{\sim 3} \left(\frac{N_{rev}}{rpm}\right) k_e \tag{1-1}$$

Where C is the rated load of bearing, P is the applied load (includes radial and axial loadings), N_{rev} is the base revolution number, k_e is an environmental factor.

b. Air Bearings

Air bearings function by holding the rotor shaft using air pressure and without direct contact. This air pressure can either be generated externally or by the rotor [5]. In most cases, it is usual for air bearings to be designed much smaller than magnetic bearings for the same load capacity and stiffness. This allows for realization of more compact machines for high speed applications [53].

One of the main disadvantages of air bearings is their poor dynamic stability [53]. However, they have been recorded to operate up to speeds of about 700 krpm and temperatures of up to 650 °C [54].

c. Magnetic Bearings

Magnetic bearings employ the principle of levitation by use of a magnetic force. They are characterized by their complex auxiliary control system and this inevitably increases their cost as compared to the other types of bearings [5]. On the other hand, their precise position control and vibration damping make them particularly appropriate and desirable in high-speed rotating machines [55].

[56] presented the design and analysis of a permanent magnet bearingless high-speed motor and also demonstrated that the bearingless technology is capable of being used for high-speed applications. The bearingless design is a proposed improvement on the active magnetic bearings but it has not yet been completely realized in high-speed applications as research is still on-going [57], [58].

Due to the fact that magnetic bearings only make use of permanent magnet interactions or reluctance forces, they cannot be stable, according to the Earnshaw theorem [59]. In order to achieve better stability in magnetic bearings, there have been several developments in hybrid magnetic bearings such as in [53], [60] which combine both air and magnetic bearing properties.

1.2.6. Thermal Challenges

Because of their high rotational speed, HS machines allow for smaller machine volumes as compared to the conventional types. This therefore implies a higher loss density in high-speed machines. With respect to permanent magnet machines, this poses a great cooling challenge in the rotor more than the stator as cooling can only be performed through the air gap.

High-speed machines require the use of a retaining sleeve in order to protect the magnets (in SPM machines) from huge centrifugal forces acting on the rotor. There are a number of key properties that the retaining sleeve should possess such as sufficient mechanical strength, good thermal conductivity and low electromagnetic losses [61]. It is also important that the retaining sleeve be as thin as possible but still providing the needed mechanical strength to retain the magnets in SPM machines [62]. A thin retaining sleeve allows for better heat transfer from the rotor to the air gap. Figure 1-10 shows a typical surface mounted permanent magnet machine for high speed operation.

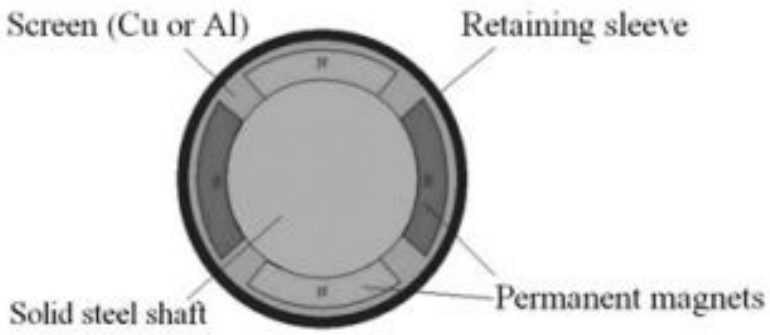

Figure 1-10: Typical layout of SPM rotor [62]

From various published papers, it is evident that the carbon-fibre composite sleeve appears to be the most popular material for high-speed PM machines. It has a high strength to weight ratio, very low electrical conductivity and very low eddy current heat generation. It is usually used in combination with either copper or aluminium for a better shielding effect to reduce eddy currents in the magnets [62]. A few examples in literature where the carbon-fibre sleeve has been employed include [63]–[65].

Titanium is another material that has been employed for use in retaining sleeves. Titanium alloys have very high tensile strength and better thermal conductivity. One main disadvantage is the higher electrical conductivity that usually results in high eddy-current losses in the sleeve [62].

1.2.7. Cooling of High Speed Machines

The high operating frequency of high-speed electrical machines demands that the cooling system be of primary importance due to increased losses per volume. These losses can be controlled either by enhancing the cooling system or reducing the electromagnetic loading [4]. The design of the cooling system depends on the type of application and a trade-off should be made between machine structural stiffness and cooling design [66]. [4] also suggests that the bearing selection should be considered in setting the limit of the machine temperature.

The cooling methods that are typically used include forced air cooling, oil cooling and water cooling. In some cases, a combination of air cooling and liquid (oil/water) cooling is used. Table 1-3 shows a comparison of different cooling methods used for high-speed application.

Table 1-3: Comparison of cooling methods

Cooling	**Characteristics**
Oil	• Allows director cooling of stator and rotor • Gravity-fed system has limited flow • Flow velocity and dynamic force effects • Magnet temperature distribution hot spots (for PM)
Water/Ethylene Glycol	• Challenge to remove heat from rotor • Heat from rotor can impact bearing durability • Magnet temperature distribution hot spots (for PM) • May require overdesign of the magnet or machine to ensure operation within thermal limits (for PM)
Air	• Can enable rotor and stator cooling • Low cost • Lower heat transfer capacity per volume • Particulate filtering

1.3 Research Questions and Objectives

This thesis aims to document the development of a high speed permanent magnet machine for use in a CHP system. The high speed machine is to be directly coupled to a turbine to produce an output power of 10kW at 30,000 rpm through a power converter.

Below is a list of the research questions aimed at achieving the objective of this dissertation:

- What are the current developments in high-speed electrical machines?
- What are the competing topologies for use in high-speed applications and which PM machine topology would be best suited for this application with respect to size, efficiency, simplicity of design and control technique?
- What is the method of design for a high-speed surface mounted permanent magnet machine?
- What special considerations should be taken into account in the design and development/prototyping of high-speed machines?
- What losses are associated with the operation of high-speed machines?

The secondary objectives include:

- To analytically model a HS surface mounted PM machine
- To analytically model the core losses associated with the designed machine.
- Determining the core loss coefficients analytically.
- Minimizing losses during the design stage and thus increasing efficiency.

1.4 Dissertation Overview and Contributions

A number of high-speed machine topologies are discussed in this dissertation. However, the design, analysis and prototyping is limited to a surface mounted permanent magnet machine. The research methods are mainly analytical and FEA. The design and performance of the machine is modelled analytically and validated through simulation with ANSYS Finite Element software package. A prototype of the high-speed SPM machine was constructed.

This dissertation also aims at contributing to existing literature on the accurate estimation of high frequency core losses in high-speed machines. The core losses constitute a larger percentage of the overall losses in the machine. Careful estimation of these losses is imperative in order for the designer to select the appropriate material as well as develop appropriate cooling strategies for high frequency operation. Current literature in this subject area mostly provides a general approach to the estimation of core losses i.e. the classic estimation of core losses which tends to be inaccurate at higher frequencies and flux densities. A comparison of the existing methods of estimation is also included in the analysis.

In addition to this, the dissertation also presents an approach to the detailed sizing of high-speed PM machines as well as the dimensioning of the magnet retention sleeve which is usually estimated based on experience from existing designs in literature. Lastly, details on the construction of the high-speed machine prototype are also presented, with an emphasis on the major components of the machine.

The detailed estimation and analysis of rotor and winding losses was not covered. These losses are seen as negligible compared to the stator core losses which form a larger proportion of the total losses in the machine.

1.5 Limitations

This dissertation is limited to the electromagnetic design, analysis and prototyping of a high-speed PM machine. There are various areas that require complete consideration for the design and development of a high-speed machine as compared to the traditional low-speed machines. These include mechanical aspects to support operation at high-speeds, development of a high-speed test rig, electromagnetic issues i.e. core losses arising from high-frequency operation, no load and full load testing etc. This could not all be covered within the scope of this dissertation and will need to be considered for future work. Recommendations for future work have been outlined in Chapter 9.

The thermal analysis was not conducted as the electrical loading of the machine was designed to be within a reasonable range. In addition to this, two methods of cooling were provided i.e. air cooling and liquid cooling.

Full testing of the machine could not be conducted as there are numerous mechanical issues that needed to be considered for construction of a high-speed test rig and safe operation up to rated speed of 30,000 rpm. Some of these issues include high-speed balancing, precision mounting as well as the need for a high-speed gear box to run the machine up to rated speed.

1.6 Structure

A brief description of each chapter is outlined in this section:

Chapter 1: A general review of literature on high-speed machines including applications, topologies and challenges.

Chapter 2: Discussion on the selection of the PM machine topology to be employed based on the requirements of the application.

Chapter 3: Material selection and detailed sizing of the PM machine. This also includes sizing of the magnet retention sleeve.

Chapter 4: This chapter presents an analytical model of the machine based on the per-phase equivalent circuit of surface mounted PM machine.

Chapter 5: The model developed in chapter 4 is simulated using FEA software and results presented in this chapter. The analytical model is validated with results obtained from FEA.

Chapter 6: Modelling of the high-frequency core losses is presented in this chapter as well as the estimation of the core loss coefficients.

Chapter 7: Presents brief details of the prototyping process

Chapter 8: Conclusion and recommendations for future work

Chapter 2

2 Topology Selection

This chapter outlines the selection of a PM machine topology based on the comparison of the radial flux and axial flux PM machine topologies.

Selection of the appropriate design topology is of critical importance in the design of high speed machines. Both electromagnetic and mechanical considerations have significant impact on the rotor design. The rotor structure should be strong and rigid enough to withstand the large centrifugal forces present during high speed operation and at the same time be able to produce the required electromagnetic torque and output power. As described in the previous chapter, the PM machine was preferred over other machine designs due to its simplistic structure and high power density.

2.1 Radial Flux versus Axial Flux PM Machines

A permanent magnet machine is composed of a rotor with either surface mounted magnets or magnets embedded in the rotor and a stator which holds the windings. In the case of a generator, the rotor with the permanent magnets is rotated by the prime mover and a current is produced in the stator windings from the time varying magnetic field.

There are a number of possible design structures for permanent magnet machines. The two most common structures are radial flux and axial flux machines.

a. Axial Flux Machines

With axial flux machines, as with their name, flux flows in the axial direction and the stator windings are placed along the radial direction. They are mostly employed where space is a constraint and have not found widespread use due to increased manufacturing time and cost [67]. Figure 2-1 shows the configuration of an axial flux machine.

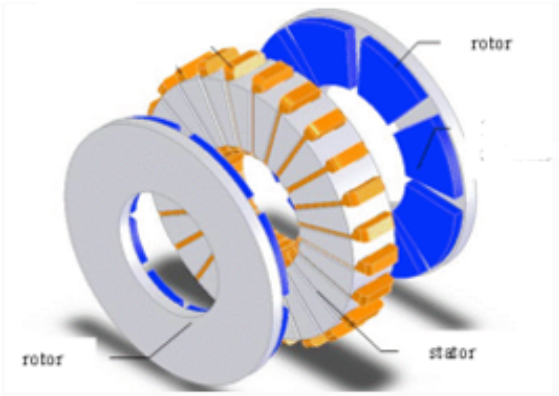

Figure 2-1: Axial Flux PM Machine Configuration [68]

Although Axial Flux Permanent Magnet (AFPM) machines are inherently suitable for high-performance applications, they are still perceived as machines with a poor constant power speed range due to their low values of synchronous inductance [69]. However, recent developments in the AFPM machines have seen an increase in their constant power speed range through newer topologies and alternative ways to achieve flux weakening [69].

Figure 2-2 displays a general classification of AFPM topologies using a tree diagram [69]. The single sided structure is the simplest, from which both the Karman and Torus type machines are derived.

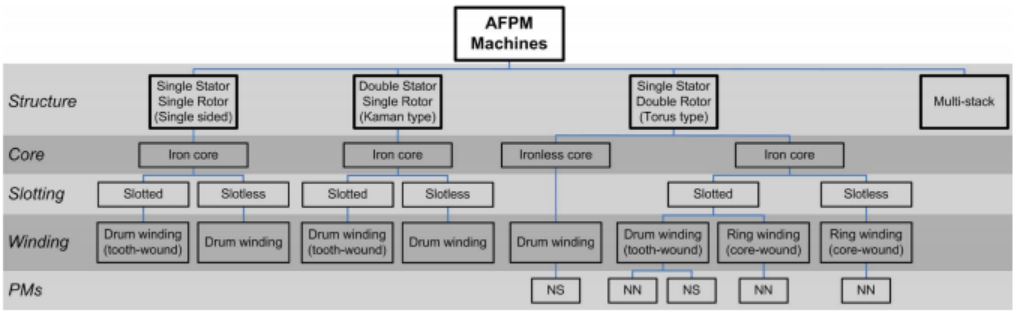

Figure 2-2: AFPM machine topologies

Extensive research has been conducted comparing AFPM machines to other machine topologies such as the radial and transverse flux machines. [70]–[74] show that the AFPM and RFPM machines display similar performance characteristics for different basis of comparison. A huge draw back for the use of AFPM machines in high speed applications is the complexity in retaining the magnets. The key conclusion is that the

topology selection will be based on size requirements, cooling method, efficiency as well as total volume and cost.

b. Radial Flux Machines

Flux travels radially from the rotor to the stator in these machines and there is the possibility of either an inner rotor or outer rotor. Considering the inner rotor machine, there are a number of rotor designs other than the standard surface mounted magnets.

Figure 2-3 below shows the two competing configurations for the inner rotor radial flux machine.

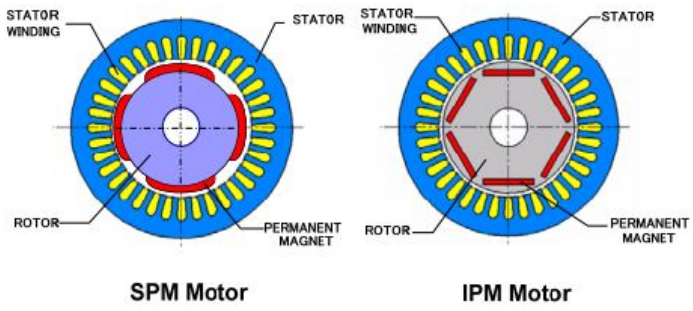

Figure 2-3: Radial Flux Machine Configurations

The surface mounted PM machine has its permanent magnets mounted on the surface of the rotor. Different industrial applications have adopted the use of surface-mounted pm machines for their high torque density and power density [75]. Although the retention of permanent magnets on the rotor may seem to be a slight disadvantage, surface permanent magnets have still shown dominance over other configurations such as the inset PM machines.

The dominance of SPM machines can be also be attributed to the fact that the SPM machines show a greater robustness over other configurations such as the IPM machines. The use of a magnet retention sleeve has proved to better at retaining magnets at high speeds than embedding them in the rotor as with IPM machines [18], [24], [76].

Below is a summary of the advantages and disadvantages of SPM machines:

Table 2-1: Advantages and disadvantages of SPM machines

Pros	**Cons**
Zero Saliency	Magnet retention
Simplest Topology	High cogging torque
Less complex power electronics	Lack of field weakening capability
High power factor	Cost of permanent magnets and risk of demagnetization at high temperatures

The most attractive of these advantages is that the surface mounted machine has the simplest design. In addition to this it possesses zero saliency i.e. the inductance values in the d-axis and q-axis are the same regardless of rotor position; this provides for less complex power electronics for the converter [77].

2.2 Selection of Design Topology

Radial Flux Permanent Magnet (RFPM) machines are more suitable for high-speed machine applications as compared to AFPM machines for their simplicity in both control and construction. The SPM topology was selected for design over the IPM topology after careful consideration of the pros and cons of both machines as well as the type of application. High-speed machines require a simple and robust rotor geometry and construction. These are all features displayed by the SPM topology and make it a suitable alternative for high-speed applications.

A summary comparing the conventional RFPM and AFPM topologies is given in Table 2-2.

Table 2-2: Comparison of RFPM and AFPM topologies

Machine Topology	**Advantages**	**Disadvantages**
Surface PM machine	Simple, robust construction Zero saliency Simplistic control and power electronics	Lack of field weakening Magnet retention
Interior PM machine	Field weakening capability Easy magnet retention – no need of retaining sleeve	Relatively complex control Higher leakage flux Lower speeds
Axial Flux PM machine	High torque-to-mass ratio High power factor	Large pole number for HS High material cost

Chapter 3

3 Material Selection and Machine Sizing

The following section will discuss the material selection and sizing of the HS SPM machine. The machine has a power rating of 10 kW, rotating at 30000 rpm with a terminal phase voltage of 220 V_{rms}. An output efficiency of 90% or more before optimization is required in order to maximize efficiency of the CHP system. The dimensions of the machine are required to fit into the T100 CHP unit as described in Appendix B-5.

3.1 Material Selection

The traditional permanent magnet machine is made out of five material classes as described by [9]. The increasing availability of new materials has been as a result of demanding mechanical and electrical requirements in high-speed electrical machines. Table 3-1 displays the details of these material classes.

Table 3-1: Classification of materials for HS applications

Material Class	**Location**	**Properties of interest**
Soft magnetic	Rotor Stator	• Saturation Flux Density • Yield and tensile strengths • Ductility and Brittleness • Low iron loss over a wide frequency range
Hard magnetic	Rotor Stator	• Coercivity • Remanent flux • Yield and tensile strengths • Operating temperature • Low electrical conductivity

Conductors	Rotor Stator	• Conductivity • Mechanical strength
Retention Systems	Rotor Stator	• Yield strength • Magnetic properties • Electrical and thermal conductivity

Selection of suitable materials is one of the key considerations during the design of electrical machines. Electrical steels fall under the category of soft magnetic materials. Recent developments in electrical steels with lower losses and higher efficiencies have enabled their use in high-speed applications. Additional criteria for selection are cost, permeability and saturation flux. It is important that the material selected enables flux concentration in the airgap and absorbs the minimum amount of magneto motive force (MMF) [3].

High quality, non-oriented electrical lamination steels are usually employed for high-speed applications. The most common materials are low carbon steels, silicon steels, nickel alloy steels and cobalt alloy steels. The selection is a trade-off between core loss and cost. Silicon steels usually have about 3% silicon which increases the resistivity and hence a reduction in eddy current losses. Table 3-2 shows a comparison of the different lamination materials [3].

Table 3-2: Properties of laminated steel

Material Type	**Core Loss**	**Saturation Flux Density**	**Permeability**	**Ease of processing**	**Relative cost (Si is 1.0)**
Low Carbon Steel	Fair	Good	Good	Best	0.5
Si Steel	Good	Good	Fair	Good	1.0
Thin Si Steel	Better	Good	Fair	Fair	10.0
49% Ni Alloy	Good	Fair	High	Care Req'd	12.0
80% Ni Alloy	Better	Low	Best	Care Req'd	15.0

Co Alloy	Good	Best	Good	Care Req'd	45.0

The M19 29G Silicon Steel was selected (highlighted in Table 3-2) for the PM machine design as it is readily available, relatively economical with low core losses and has a high saturation flux density. Although Nickel and Cobalt alloys have lower iron losses, they are costly and only used in high performance applications such as military aircrafts [3].

In the case of hard magnetic materials i.e. permanent magnets, selection is based mainly on power density and temperature capability. The material properties of permanent magnets determine the size and performance of high-speed PM machines. NdFeB and SmCo are the material of choice for most high-speed scenarios with Nd based magnets having the highest power density and Sm based magnets having superior temperature capability [9].

Between the two rare-earth magnets, NdFeB is preferred as it is cost-effective and more readily available. NdFeB still displays a few disadvantages such as lower resistance to temperature effects and moderate corrosion but these can be controlled by employing sufficient cooling and surface treatments respectively [3]. For these reasons, NdFeB magnets were selected for use in the PM machine design with properties as listed in Table 3-3.

Table 3-3: Selected NdFeB magnet properties

Property	**Units**	**Value**
Energy Product (BH_{max})	kJ/m^3	247
Maximum Temperature	°C	180
Recoil Permeability (μ_r)	-	1.04
Remanence Flux Density (B_r)	T	1.13
Coercivity (H_c)	kA/m	852
Magnet Grade	-	N33
Mass Density	Kg/m^3	7550

As described in section 1.2.4, copper litz wire is usually selected for high-speed applications for the reduction of AC copper losses. At high frequencies, the AC resistance is directly affected by proximity effects and skin depth which is inversely proportional to the square-root of frequency. Therefore, increasing frequency will result in higher AC copper losses. Litz wire is made up of small sized wires bound together and/or transposed thereby minimizing the skin effect on the conductor. This in turn reduces the ac resistance and consequently the ac copper loss. Copper litz conductors were chosen for use in the design of the high-speed machine.

Last but not the least is the selection of a retention system as the topology being designed is a surface mounted PM topology which employs magnets on the surface of the rotor. The most commonly reported materials are Inconel 718, CFRP or Carbon fibre composite and Ti6Al4V (titanium alloy). Ideally, a good retention material should display good thermal conductivity, a high yield strength and be non-magnetic in order to prevent the production of eddy currents. A carbon fibre composite known as PEEK was selected for the design because it is readily available, cost-effective and has relatively high tensile strengths which is adequate for the required machine specifications.

3.2 Winding Design

The winding design is usually determined by the machine's slot/pole combination. There are a number of factors that influence the choice of number of poles and slots in a machine. Determination of the optimal winding design will result in reduced cogging torque, higher flux linkage and induced back EMF and consequently better performance. In addition, the winding topology should be selected to give the lowest harmonic distortion with a high winding factor.

The number of slots is usually a multiple of the number of phases in the machine and will also determine the winding structure [3]. In this particular case, the number of phases selected is 3 phases. On the other hand, the number of poles will affect the machine structure and performance [6]. The number of poles is also related to the operating frequency of the machine. A lower number of poles is desirable as this lowers the operating frequency and consequently the core losses in the machine. A 4 pole machine was selected for this design.

The choice of either concentrated or distributed winding is influenced by the slot and pole combination. According to [67], the winding layout developed in 3 phase 4 pole winding configurations usually leads to a double layer winding and appears in just about all brushless permanent magnet motors. The choice of 4 poles also supports the double layer winding configuration by lowering the length of the end windings [6]. The table below displays the slot pole configurations considered for this design.

Table 3-4: Slot/Pole Combination for 4 Pole Design

	Number of Slots (4 Poles)										
	12	15	18	21	24	27	30	33	36	39	42
q	1	1.25	1.5	1.75	2	2.25	2.5	2.75	3	3.25	3.5
k_{w1}	1	0.957	0.960	0.956	0.966	0.955	0.951	0.955	0.960	0.938	0.956

The choice of integral slots/pole/phase is common as this combination allows for a balance between the phases [78]. From Table 3-4, the 4 pole 24 slot combination was selected for the design. According to [79], the selected number of slots should be low with a winding factor as high as possible for maximised electromagnetic performance

and lower manufacturing costs. The 24 slot topology was selected over the 36 slot even though it displayed slightly higher 5^{th} and 7^{th} order harmonics. These harmonics govern the amount of ripple torque produced by the design. As stated in the previous chapter, the ripple torque requirements are not stringent for this particular application and therefore a lower manufacturing cost was preferred over a slightly lower ripple torque.

3.3 Machine Sizing

For the preliminary design, the machine was sized on the basis of electromagnetic power produced in the airgap. [80] highlights that it is dependent on the quality of the permanent magnets in use as the volume of PMs is proportional to the output power of the synchronous machine.

Equation (3-1) shows how the electromagnetic power produced in the air gap is related to the main dimensions of the machine [80].

$$S_{elm} = \frac{\pi^2}{2} k_{w1} D_{1in}^2 l n_s B_{mg} A_m \tag{3-1}$$

D_{1in} is the rotor diameter (m)

l is the stack length of the machine (m)

n_s is the synchronous speed (rev/sec)

B_{mg} is the magnetic loading (T)

A_m is the electric loading (A/m)

To simplify equation (3-1), the l/D_{1in} ratio i.e. length to diameter ratio of the machine is introduced, which is another critical parameter for the sizing of the machine. According to [81], [82], this ratio typically ranges from 1-3 for high speed PM machines. The electric loading typically ranges from 10,000 A/m for small motors to 55,000 A/m for medium-power motors [80], [83].

The electrical power is related to the airgap apparent power as in the following equation [84];

$$P_{gen} = 3V_a I_a \cos\phi = 3\frac{E_f}{\varepsilon} I_a \cos\phi = \frac{1}{\varepsilon} S_g \cos\phi \tag{3-2}$$

$\varepsilon = E_f / V_a$ is the ratio of EMF induced by the rotor excitation flux to the input voltage

Equations (3-1) and (3-2) can be combined to determine the D^2L product which is proportional to the volume of the machine and also determines the output torque of the machine;

$$D_{1in}^2 l = \frac{\varepsilon P_{gen}}{0.5\pi^2 k_{w1} n_s B_{mg} A_m \cos\phi} \tag{3-3}$$

The choice of *l/D* ratio can be chosen once the D^2l product has been obtained. This ratio depends on the application being designed for. The values vary widely and are provided in various sources of literature [80], [82], [83]. A first estimation ratio of $l/D = 2$ was taken for the design of the machine.

A rule of thumb according to [80], [85], [86] is to assume the ratio of the rotor diameter to stator diameter being equal to about 0.55 for 4 pole machines, which can then be optimized using FEA based on the magnetic loading. The choice of length and diameter are directly tied to the mechanical integrity of the rotor. Improper selection of these parameters will lead to resonant vibrations and consequently bending [5]. The rotor radius is inversely proportional to the centrifugal force acting on the rotor as in equation (3-12).

Using equation (3-3) from above, the rotor diameter, $D_{1in} = 70\ mm$ and with the assumed length-to-diameter ratio of '2', $l = 140\ mm$. Table 3-5 below shows a list of the design parameters used for estimation of the l/D ratio of the machine.

Table 3-5: Design parameters for estimation of l/D ratio

Design Parameter	**Value**
ε	0.9
P_{gen}	10 kW
n_s	30, 000 rpm
B_{mg}	0.8
A_m	10, 000 A/m
cos Ø	0.95
k_{w1}	0.966

3.4 Magnet Dimensions

In order to calculate the magnet height, equation (3-4) was used. This equation relates the air gap flux density to the magnet height and the magnet remnant flux density. Equation (3-4) is simplified from the equation presented in [67], assuming unity values for flux concentration factor, reluctance factor and leakage factor.

$$B_g = \frac{h_m}{h_m + g} B_r \tag{3-4}$$

h_m = height of magnet in (mm)

g = Height of air gap in (mm)

B_r = Remnant flux density in (T)

B_g = Air gap flux density (T)

A first estimate of the magnet height is 5 – 10 times the height of the air gap [67], [80]. This applies to the use of high-coercivity magnets. Assuming a gap of 1mm for the air gap (g), the magnet height (h_m) was chosen as 5mm for the initial design.

The final magnet height was obtained after an iterative process in Ansys Maxwell 2D and Matlab to obtain an optimized value.

3.5 Stator Dimensions

The stator dimensions are mainly determined by the material selection as this governs the flux density to avoid saturation of the material. For this design, the material chosen was Silicon Steel M19 29 Gauge with a saturation flux density of about 1.6 T.

$$\phi_p = B_g \lambda_p l \tag{3-5}$$

ϕ_p is the flux per pole (Wb)

Where

$$\lambda_p = \frac{\pi D_{1in}}{2p} \tag{3-6}$$

λ_p is the magnet pole pitch in (m) assuming full pole pitch

p is the number of pole pairs ($p = 2$)

D_{1in} = Rotor Diameter (m)

Figure 3-1 below shows details of the main dimensions of the motor;

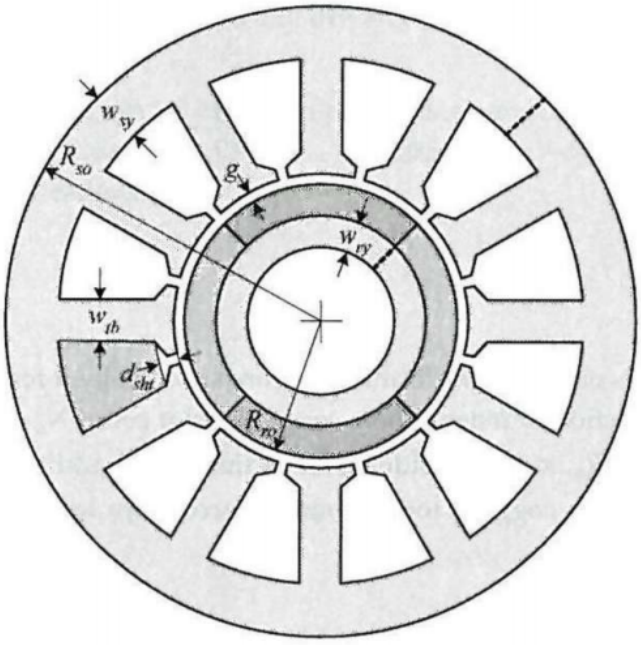

Figure 3-1: Machine dimensions [67]

From the values obtained in the previous sections, the flux per pole is calculated using equations (3-5) and (3-6). Equation (3-7) relates the flux per pole, stack length and stator yoke flux density to the width of the stator yoke. It assumes the yoke carries half the pole flux.

$$W_{sy} = \frac{\phi_p/2}{B_{sy} l} \tag{3-7}$$

W_{sy} is the width of the stator yoke in (m)

B_{sy} is the stator yoke flux density in (T)

To calculate the tooth body width, equation (3-8) obtained from [67] relates the tooth body width to the slot pitch, air gap flux density and the tooth saturation flux density.

$$W_{tb} = \frac{\lambda_s B_g}{B_t} \tag{3-8}$$

B_t is the tooth flux density to avoid saturation (T)

λ_s is the slot pitch (m)

$$\lambda_s = \frac{2\pi R_{ro}}{N_s K_{st}} \tag{3-9}$$

N_s is the number of slots

R_{ro} is the rotor outer radius (m)

K_{st} is the stacking factor with a typical value of ~0.9

For calculation of the slot height;

$$h_s = \left(R_{so} - W_{sy}\right) - R_{si} \tag{3-10}$$

R_{si} is the inner stator radius (m)

Expanding from the equations above, the slot area can be calculated;

$$A_s = \frac{\pi}{N_s}\left[(R_{so} - W_{sy})^2 - (R_{ro} + g + d_{sht})^2\right] - W_{tb}\left(R_{so} - W_{sy} - R_{ro} - g - d_{sht}\right) \quad (3\text{-}11)$$

N_s is the number of slots

d_{sht} is the height of the stator tooth fillet (m)

R_{so} is the stator outer radius (m)

3.6 Rotor Retaining Sleeve Dimensions

In order to determine the dimensions of the retaining sleeve, there are a few factors that have to be taken into consideration. Of these, the most important being the centrifugal force on the magnets due to the high-speed rotation of the rotor. As described in section 3.1, a carbon-fibre composite i.e. PEEK was selected as it displays reasonable strength (~ 200 MPa/29 ksi) i.e. high yield stress and lower conductivity hence lower eddy current losses.

The force acting on the magnets is converted to an outward pressure known as the hoop stress, which acts on the inner surface of the retaining sleeve. Matlab code adapted from [3] was modified to determine the stress limit for different thicknesses of the retaining sleeve.

The centrifugal force acting on the magnets is defined using the equation below:

$$F_{cen} = \frac{M_m + v_{mag}^2}{R_{ro} + h_m} \quad (3\text{-}12)$$

M_m is the mass of the magnets

v_{mag} is the velocity of the magnets in m/s

The stress as calculated using Matlab is shown in Table 3-6 below for sleeve thicknesses from 0.5 mm to 3.5 mm. The selected sleeve stress as calculated from Matlab should be equal to or lower than the material's yield stress. This will allow for adequate retention of the magnets.

Table 3-6: Stress on retaining sleeve for different thicknesses

Sleeve Thickness (mm)	Hoop Stress (MPa)	Hoop Stress with SF (MPa)
0.5	334.4	368.2
1.0	167.5	184.1
1.5	111.7	122.7
2.0	83.4	91.7
2.5	66.9	73.8
3.0	55.8	61.4
3.5	47.6	52.4

It is evident from the table above that a thickness of 1 mm is sufficient for the retaining sleeve. A safety factor (SF) of 1.1 was also applied to account for inaccuracies and during manufacturing. This has no adverse effect on the magnetic/mechanical design of the machine.

One critical point to note here is that this method is valid for a rotor with a perfect centre of mass. This is achieved through precision machining and dynamic balancing. A slight deviation in the centre of mass is capable of increasing the centrifugal force (hoop stress) two fold and even more. Measurement of the rotor body after complete construction and dynamic balancing revealed the centre off mass to be very close to centre and only being about 2 microns off. This means that the designed rotor sleeve will be able to retain the magnets up to maximum operating speed.

3.7 Design Parameters

The machine parameters were obtained using the equations discussed in this chapter. Matlab was used to generate the input parameters of the machine using the design equations from the previous sections. Table 3-7 displays these parameters:

Table 3-7: Initial design parameters

Parameter	**Symbol**	**Value**	
Number of phases	$\emptyset$	3	
Number of pole pairs	p	2	
Number of slots	N_s	24	
Power rating	P	10	kW
Speed	n_s	30000	rpm
Torque	T	3.18	Nm
Terminal voltage (RMS)	Ea	218.83	V
Current (RMS)	I	16.61	A
Frequency	f	1000	Hz
Stator Outer Diameter	D_{so}	120	mm
Rotor Diameter	D_{1in}	70	mm
Machine Length	l	140	mm
Airgap Length	g	2	mm
Retaining sleeve thickness		1	mm
Tooth width	w_{tb}	4.2	mm
Stator yoke	h_{sy}	9.6	mm
Slot height	h_s	9.33	mm
Slot width (Average)	w_s	6.88	mm
Slot area	A_s	7.25e-05	mm^2
Magnet height		2.92	mm
Magnet angle		60.03	º Mech
Turns per phase	T_{ph}	16	
Turns per coil	T_c	2	

Chapter 4

4 Analytical Model of High Speed PM Machine

This chapter presents an analytical model of the high-speed PM machine that will be used to determine the parameters and performance of the machine. The design is based on the requirements of the turbine including maximum output power, turbine speed and bus voltage. Due to the choice of the topology i.e. radial-flux surface mounted pm machine, saturation of the magnetic circuit will be neglected as it is not considerable. The machine was designed for an output power of 10 kW rotating at 30,000 rpm and a terminal rms voltage of 380 V_{Line}.

4.1 Analytical Model of High Speed PM Machine

The analytical model of the PM generator is presented here. The machine is assumed to be balanced and therefore its parameters can be represented on a per phase basis and subsequently applied to other phases. Figure 4-1 below shows the per phase model of the machine.

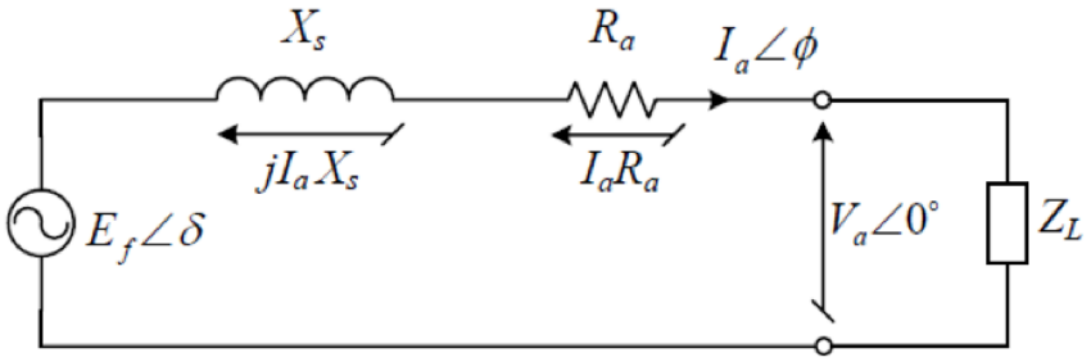

Figure 4-1: Per-phase equivalent circuit model

4.1.1. Flux Density

The presence of magnetic flux linkage in a machine induces voltage across a winding within a rotating magnetic field according to Faraday's Law. Flux travels from the magnet poles across the airgap to the stator winding.

The flux travels through the path of least reluctance which is underneath the tooth shoes as opposed to the stator slot openings. A slight proportion of flux leaks along the way and does not get linked to the stator. This is accounted for by a leakage factor, $k_l \sim 0.95$ for surface mounted magnets. A reluctance factor, $k_r \sim 1.05$, is used to account for the effect of the steel reluctance on the airgap flux. In addition to this, through the use of Carter's coefficient (k_c), an effective value of the airgap length is formulated as the coefficient accounts for the difference in permeance caused by the presence of slots i.e. for areas underneath the slot regions, the flux has to travel slightly further as compared to regions underneath the tooth shoes.

The airgap flux density is calculated using equation (4-1) through to equation (4-5). Carter's coefficient is introduced in equation (4-1) in order to obtain the effective airgap length as a result of slotting [83].

$$k_c = \left[1 - \frac{1}{\frac{\lambda_s}{w_s}\left(5\times\frac{l_g}{w_s}+1\right)}\right]^{-1} \tag{4-1}$$

Where w_s is the average width of the slot is, w_{tb} is the tooth width and the slot pitch (λ_s) is described as $\lambda_s = w_{tb} + w_s$.

The effective airgap is calculated as;

$$g_e = k_c g \tag{4-2}$$

Where g_e is the effective airgap length

The permeance coefficient when described using the magnet demagnetization curve, is the absolute value of the slope (normalized to μ_0) of the load-line drawn from the origin through the operating point. On the demagnetization curve, the permeance coefficient is used to measure the point at which the magnet operates in open circuit.

$$PC = \frac{h_m}{g_e C_\phi} \tag{4-3}$$

Where PC = Permeance Coefficient

C_ϕ = Flux concentration factor $\left(A_m / A_g\right)$

The flux concentration factor relates the magnet area (A_m) to the airgap area (A_g).

The plateau value of airgap flux density is described using equation (4-4);

$$B_g = \frac{k_l C_\phi}{1 + k_r \frac{\mu_{rec}}{PC}} B_r \tag{4-4}$$

Where μ_{rec} = recoil permeability

B_r = remanent flux density

The flux density in the airgap can be represented as a Fourier series with contributions from odd number harmonic due to half-wave symmetry;

$$B(\theta) = \sum_{n=1}^{\infty} B_n \sin(np\theta) \tag{4-5}$$

Where $B_n = \frac{4}{n\pi} B_g k_{gn} \sin\left(\frac{np\theta_m}{2}\right) \sin\left(\frac{n\pi}{2}\right)$

and

$$k_g = \frac{h_m}{g + h_m}$$

k_g is the magnetic gap factor describing the geometry of the airgap

4.1.2. Excitation Voltage

Below is an expression for the fundamental value of the rms voltage induced in the phase winding of the machine:

$$E_f = \frac{2\pi}{\sqrt{2}} f T_{ph} k_{w1} \phi_p \tag{4-6}$$

Where k_{w1} = fundamental harmonic winding factor

ϕ_p = flux per pole

f = electrical frequency

T_{ph} = Number of turns per phase

The fundamental harmonic winding factor is a product of a pitch factor (k_{p1}) and distribution factor (k_{d1}). In practice, windings are normally short-pitched and this is accounted for by the winding factor which is the ratio of flux linked by an actual winding to the flux linked by a full-pitch winding.

$$k_{w1} = k_{p1} \cdot k_{d1} = \frac{\sin\left(\frac{q\lambda_s}{2}\right)}{q \sin\left(\frac{\lambda_s}{2}\right)} \cdot \sin\left(\frac{\tau_c}{2}\right) \tag{4-7}$$

Where q = number of slots/pole/phase i.e. $q = N_s/2p/3$

λ_s = slot pitch

τ_c = coil pitch

The peak flux per pole linked by an ideal full pitched coil is given by;

$$\phi_p = \frac{B_{1max} D l}{p} \tag{4-8}$$

Where B_{1max} = peak value of fundamental harmonic of flux density

D = Stator inner diameter

l = Axial length

Additionally, B_{1max} can be expressed in terms of the plateau value of flux density B_g described earlier in equation (4-4);

$$B_{1max} = k_f B_g \tag{4-9}$$

Where k_f = form factor

The form factor of the excitation field in the case of a single magnet per pole is expressed as:

$$k_f = \frac{4}{\pi} \sin\left(\frac{\alpha\pi}{2}\right) \tag{4-10}$$

Where α is the pole arc to pole pitch ratio

4.1.3. Synchronous Reactance

The synchronous reactance can be written in terms of leakage (X_l) and magnetizing (X_m) reactance:

$$X_s = X_l + X_m \tag{4-11}$$

Where $X_s = \omega L_s$ and L_s is the synchronous inductance

The synchronous inductance determines the rate at which winding currents can change and is used in current control techniques. In surface PM machines, the d and q-axis reactances are equal.

The magnetizing reactance as a result of airgap inductance, can be calculated using equation (4-12) [83]:

$$X_m = \frac{6\mu_0 lDf k_{w1}^2 T_{ph}^2}{p^2(k_c g + h_m/\mu_r)} \tag{4-12}$$

Where $(k_c g + h_m/\mu_r)$ is the effective airgap length seen by the magnetizing flux as modified by Carter's coefficient.

The leakage reactance takes into account the permeance coefficients associated with the dominant leakage flux paths i.e. the stator slot (slot + tooth top) and end winding overhang, as:

$$X_l = 4\pi\mu_0 f \frac{T_{ph}^2 l}{pq}\left(\lambda_{slot} + \lambda_{tooth-top} + \lambda_{end\ winding}\right) \tag{4-13}$$

The slot leakage permeance coefficient for semi-closed oval slots as shown in Figure A-1 can be expressed as:

$$\lambda_{slot} = 0.1424 + \frac{2h_{11}}{3(b_{11} + b_{12})} + \frac{2h_{12}}{b_{12} + b_{13}} + \frac{2h_{13}}{b_{13} + b_{14}} + \frac{h_{14}}{b_{14}} \tag{4-14}$$

The permeance coefficient associated with the tooth-top can be expressed as:

$$\lambda_{tooth-top} = \frac{5\, g/b_{14}}{5 + 4\, g/b_{14}} \tag{4-15}$$

Equation (4-16) is an expression for the permeance coefficient associated with the end winding:

$$\lambda_{end\ winding} = 0.47q\frac{l_{end}}{l} - 0.3q\frac{\lambda_p}{l} \tag{4-16}$$

Where $\lambda_P = \pi D_{1in}/2p$ is the pole pitch, h_{1t} is the height of the stator tooth and l_{end} is the length of a single end winding and can be expressed as:

$$l_{end} = (0.083p + 1.217)\frac{pD + h_{1t}}{2p} + 0.02 \tag{4-17}$$

4.1.4. Armature Resistance

For high-speed machines, litz wire is normally employed in order to minimize the high frequency AC losses that result from skin and proximity effects. The skin effect causes the current to be distributed near the outer surface of the conductor. This causes a decrease in the effective area of the winding thereby increasing the resistance of the winding. This is more significant at higher frequencies as the skin depth is inversely proportional to the square root of the operating frequency as expressed by equation (4-18).

$$\delta = \sqrt{\frac{2\rho}{\omega\mu}} \tag{4-18}$$

ρ is the resistivity of the conductor

ω is the angular frequency

μ is the magnetic permeability of the conductor

The skin depth for this particular design was calculated to be higher than the diameter of the winding strands. Therefore, the AC winding loss was ignored.

In contrast, the proximity effect refers to the effect of alternating current in one conductor on the current distribution in another, proximate conductor. Transposition of the litz winding was used to decrease the contribution from the proximity effect.

The DC armature resistance per phase can be expressed as:

$$R_{dc} = \frac{l_{ph-winding}}{a\sigma_{cu}A_{cond}} \tag{4-19}$$

l_{ph} is the total length of the phase winding

a is the number of parallel paths

σ_{cu} is the conductivity of copper

A_{cond} is the cross sectional area of a single conductor

The total length of a phase winding can be expressed as:

$$l_{ph-winding} = 2(l + l_{end})\, T_{ph} \tag{4-20}$$

For winding employing round litz wire, as with the current design, the relationship between AC resistance and DC resistance can be approximated empirically using:

$$R_{ac} \approx R_{dc}\left(1 + \frac{2r}{\delta}\right) \tag{4-21}$$

r is the radius of the round wire

Chapter 5

5 Finite Element Analysis

ANSYS Maxwell Electromagnetics Software was used to perform the finite element analysis of the SPM machine. The results presented in this section will discuss the torque, current, voltage and power of the machines. In addition, the losses of the machines are discussed in detail and the simulated results are compared to analytical calculations. Figure 5-1 displays the circuit used to analyse the FEA model in Ansys Maxwell 2D and 3D.

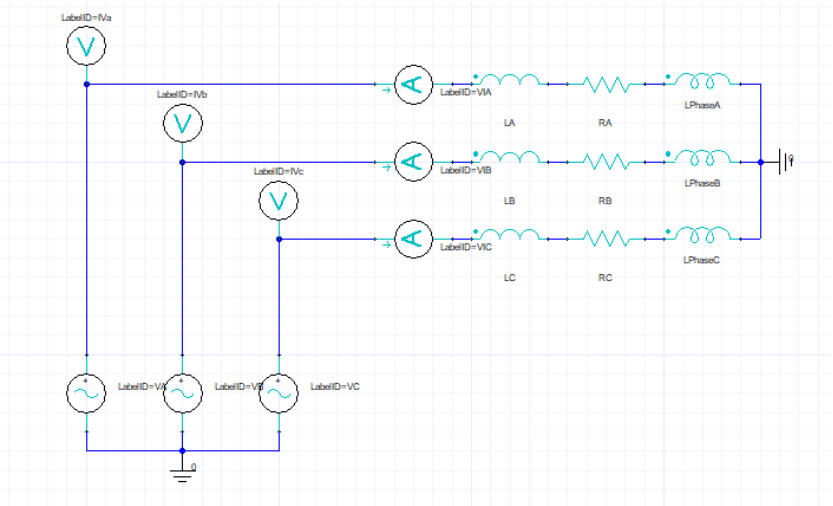

Figure 5-1: FEA Electrical Circuit

A quarter of the entire model was simulated to save on computation capacity and time. Finite Element Analysis was performed in 2D and thereafter 3D for a more accurate simulation and representation of the machine model. The figure below displays a 2D model with a flux plot of the SPM machine under no load conditions.

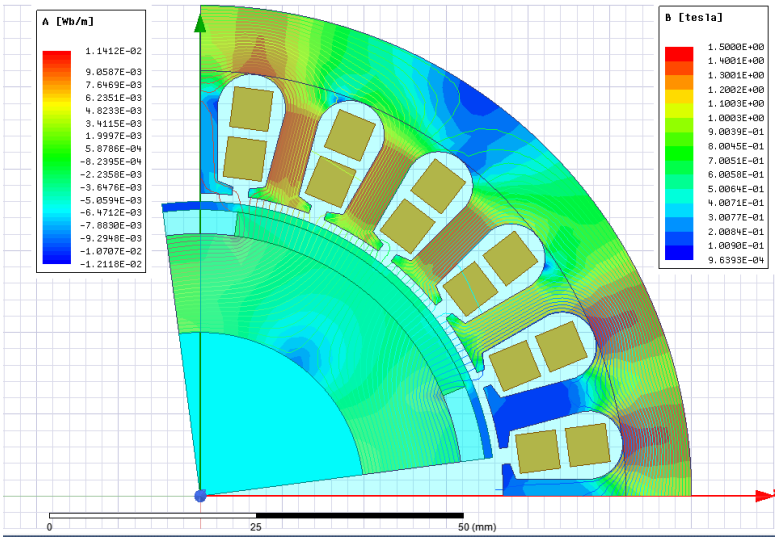

Figure 5-2: 2D Model of SPM Machine

5.1 Distribution of Flux Density within Generator

The flux density at the centre of the airgap was obtained and analysed. The plateau value of flux density is about 0.65 T. One of the design goals is to achieve a high airgap flux density in order to achieve the specified torque output of the machine. Both the circumferential and the radial components of flux density were obtained in Ansys Maxwell 2D. From the Figure 5-3, it can be seen that the stator slotting has effect on the waveform of the airgap flux density. The stator slotting increases the effective reluctance of the airgap and this is seen through the slotting on the flux density waveform shown.

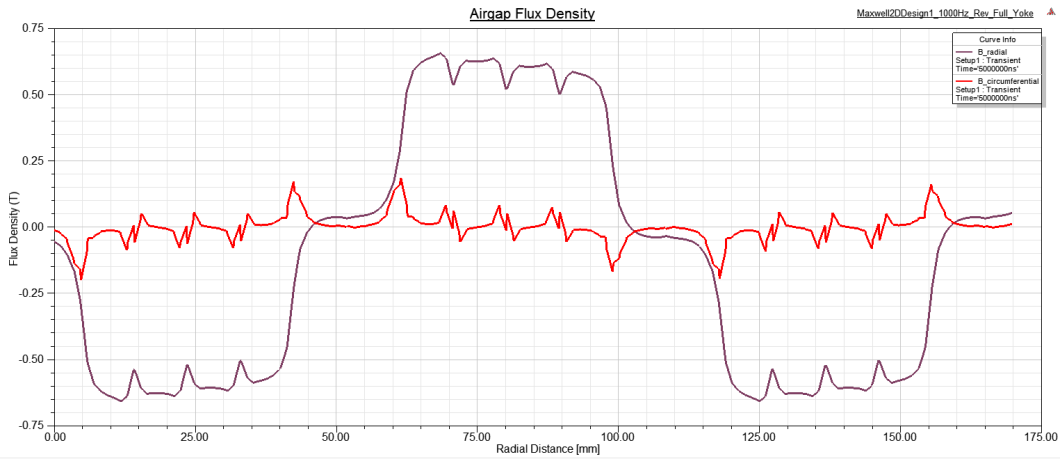

Figure 5-3: No load airgap flux density

As expected, the flux density in the airgap is largely radial with a slight contribution from the circumferential component. The circumferential component, which is seen to be close to zero, is as a result of fringing effects as the flux travels between magnet poles. In the other areas of the machine, the flux density waveform is slightly different. Further into the stator, the flux density has different compositions of the components based on the shape of the stator as well as the magnets. Figure 5-4 and Figure 5-5 show the flux densities in the stator tooth and yoke respectively.

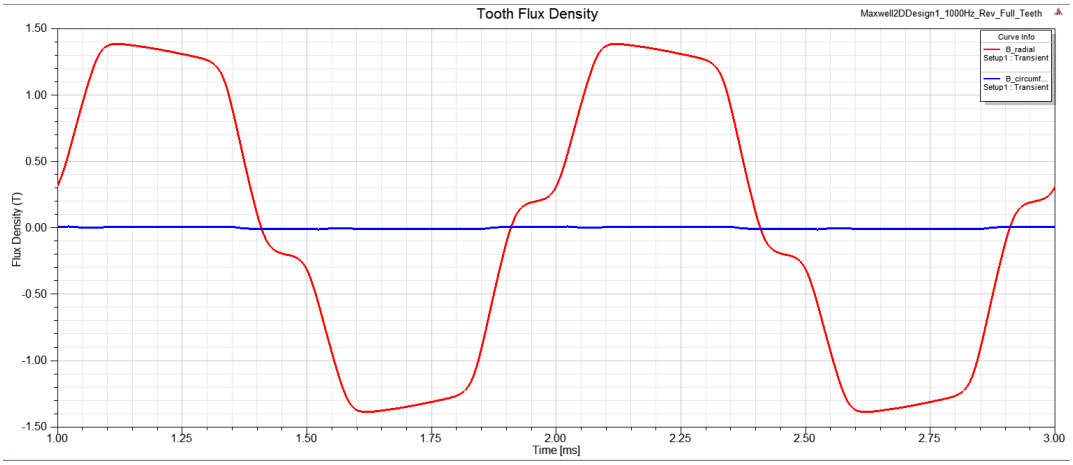

Figure 5-4: No Load Stator tooth flux density waveforms

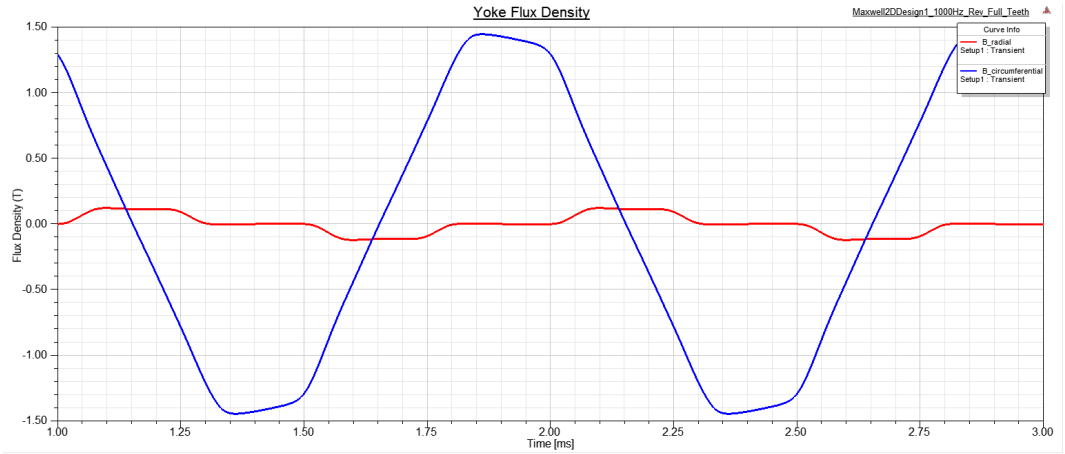

Figure 5-5: No Load Stator yoke flux density waveforms

The flux density in the stator tooth and yoke reaches a maximum of about 1.53 T. This shows that the core material is not saturated at any point. The maximum flux density is below the saturation flux density of the material (Silicon Steel M19 29G) being used. The objective was to achieve maximum magnetic loading whilst avoiding saturation of the stator and rotor material.

Further examination of the flux density plot as shown in Figure 5-2 shows that the maximum flux density appears in the stator yoke and certain sections of the centre of the teeth dependent on the rotor position.

The flux density in the rotor yoke appears to be considerably significant with a maximum of 1.26T closer to the shaft surface (inner rotor yoke) with the circumferential component of flux density being dominant.

The flux density in the rotor body is considerably low and only increases at the points below the edges of the magnets. This is due to the high concentration of leakage flux at the magnet edges.

5.2 Phasor Study – Operation in DQ Plane

The purpose of this study is to display the operation of the machine in the DQ plane using current and voltage excitation in Ansys Maxwell as well as to determine the power factor of the machine.

5.2.1. Current Excitation

In the case of current excitation, the machine is supplied with a purely sinusoidal signal described by the equation below:

$$i(t) = \sqrt{2} I_{rms} \sin\left(2\pi f t + \gamma + \theta_{ph}\right) \quad (5\text{-}1)$$

Where;

$\sqrt{2} I_{rms}$ is the peak phase current

f is the excitation frequency

γ is the current angle i.e. angle between EMF and current phasor

θ_{ph} is the phase difference

This is better illustrated using a phasor diagram. The phase current I_{rms} is the resultant phasor from the d-axis current and the q-axis current. The back-EMF phasor is taken as the reference phasor and lies on the positive q-axis.

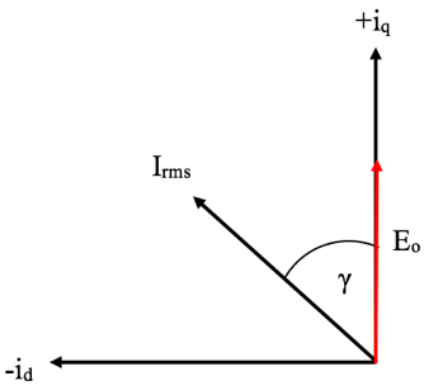

Figure 5-6: Phasor diagram (motor mode)

The current angle γ was varied from 0° to 180° and the torque recorded over this range.

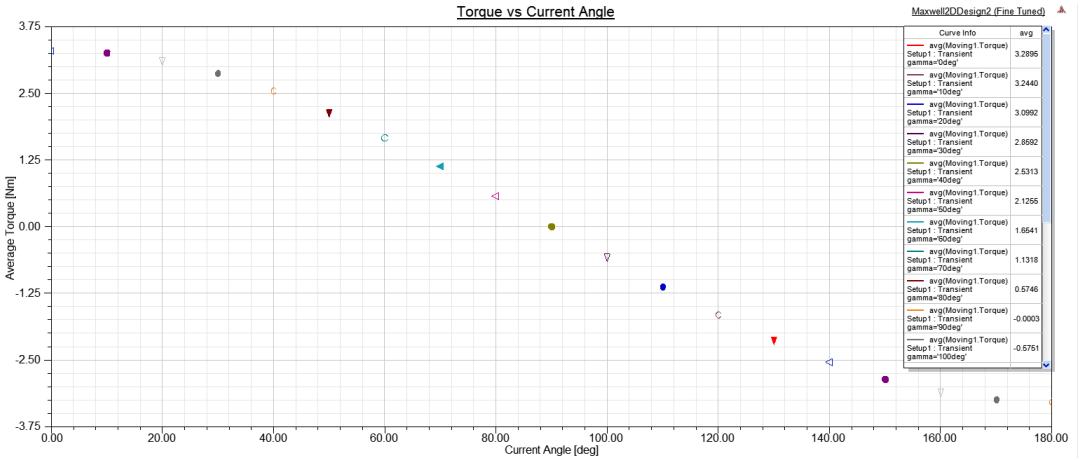

Figure 5-7: Torque vs. current angle

From above, it can be seen that rated motor torque occurs when the current angle is 0° i.e. the current phasor is on the positive q-axis. When the current angle is 90°, the machine produces zero torque. In this case, the current phasor lies on the negative d-axis producing demagnetizing current. Between 90° and 180°, the machine produces negative torque as a result of negative d-axis and q-axis currents and thus operating in generator mode. At 180°, the machine produces negative rated torque with the current phasor lying along the negative q-axis.

Figure 5-8 shows the current and back-EMF waveforms and confirms the positions of the phasors in relation to the machines operation. For a current angle $\gamma = 40°$, the current phasor should lead the back-EMF phasor by 40°.

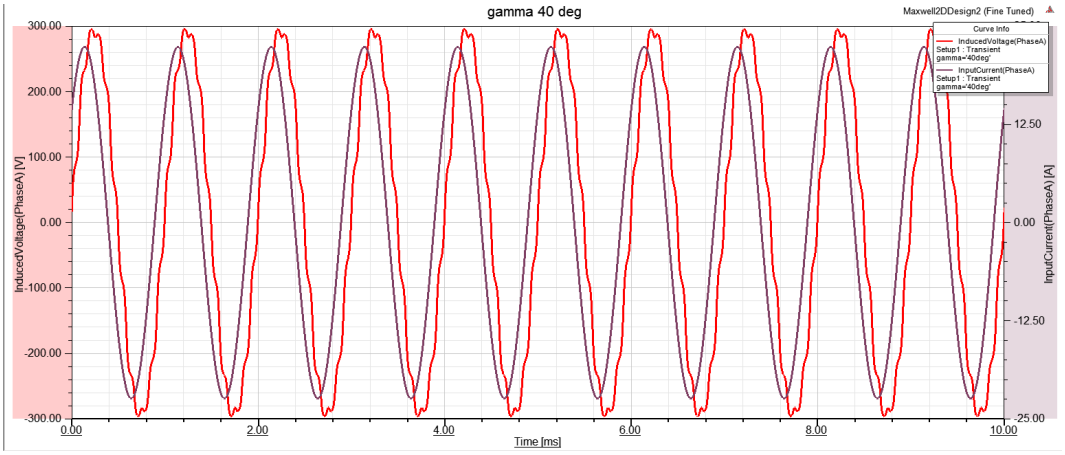

Figure 5-8: Winding currents & induced EMF waveforms

With reference to the analysis performed in the previous section, it is important to understand how the d-axis and q-axis currents influence the operation of the machine. A model of the machine in the d-q reference frame allows for accurate control of the machine at different operating points. The torque equation of a permanent magnet machine is derived from the power balance equation and simplifies to the equation below:

$$T_e = \frac{3}{2} p\left[\lambda_{pm} + \left(L_d - L_q\right) i_d\right] i_q \tag{5-2}$$

Where;

L_d and L_q are the d-axis and q-axis inductances respectively

I_d and I_q are the d-axis and q-axis currents respectively

λ_{pm} is the permanent magnet flux linkage

The first term in (5-2) above represents the torque produced by the flux of the permanent magnets i.e. synchronous torque and the second term represents the reluctance torque which is as a result of the difference in inductances in the d-q

reference frame. The second term however, only applies to the case of a salient PM machine i.e. IPM. In the case of the SPM which is a non-salient machine, the d-axis and q-axis inductances are equal i.e. $L_d = L_q$

$$T_e = \frac{3}{2} p \lambda_{pm} i_q \tag{5-3}$$

Thus, according to (5-3) the torque in a surface mounted machine is proportional to the q-axis current. This confirms the simulation results from the previous section showing the rated torque occurring when the current phasor lies along the q-axis.

5.3 Electromagnetic Performance

5.3.1. Torque

Figure 5-9 shows the full load output torque against time after a 3D FEA simulation in Ansys Maxwell. The average torque output of the machine meets the specifications with an average torque of 3.1 Nm. The ripple in the waveform is as a result of the cogging torque and the on-load ripple torque. The total on-load torque ripple is about 9 % of the total torque which is acceptable for a bio-gas turbine application. According to [87] applications such as vehicle power steering and precision machining tools would have more stringent requirements on torque ripple.

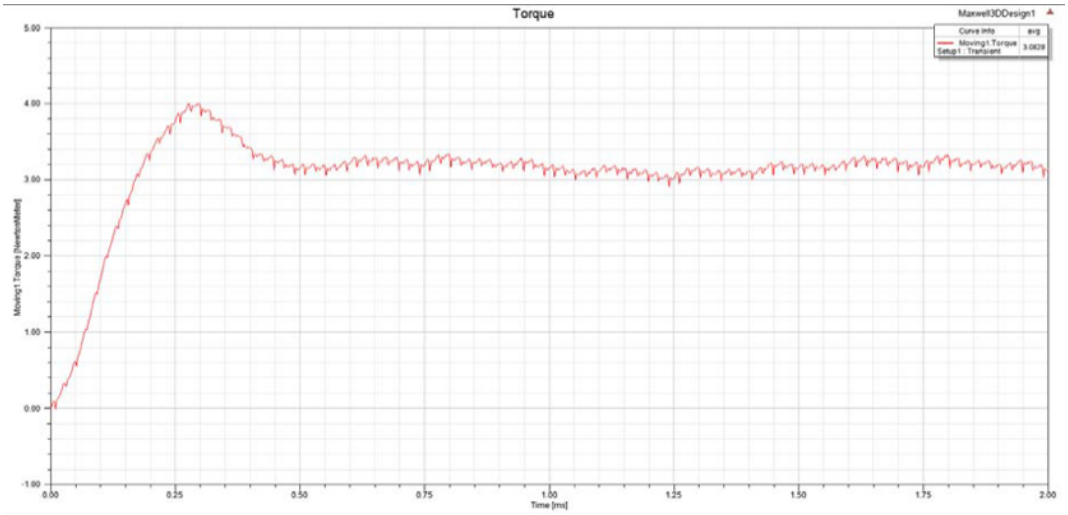

Figure 5-9: 3D FEA - Torque vs. time

5.3.2. Voltage and Current

Figure 5-10 shows the induced voltages in the winding of the machine. The goal was to achieve a sinusoidal waveform so as to avoid excessive losses in the motor and drive. The low harmonic content is apparent by the sinusoidal shape of the induced voltage waveform shown. This is due to the low harmonic content which is as a result of the 4 pole 24 slot winding design. The induced phase voltage has an RMS value of 219 V which is close to the supply voltage of 220 V RMS which also translates to lower I^2R winding losses.

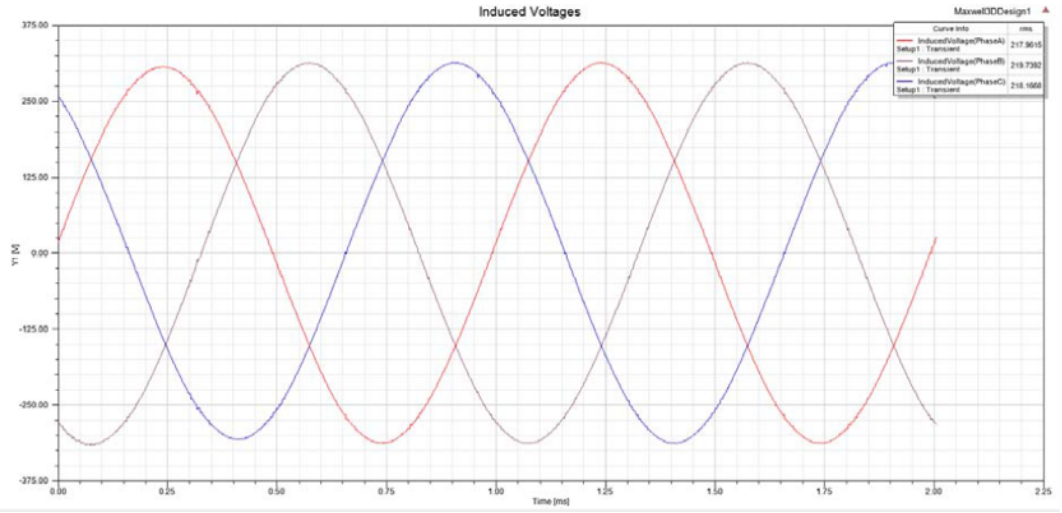

Figure 5-10: Induced phase voltage vs. time

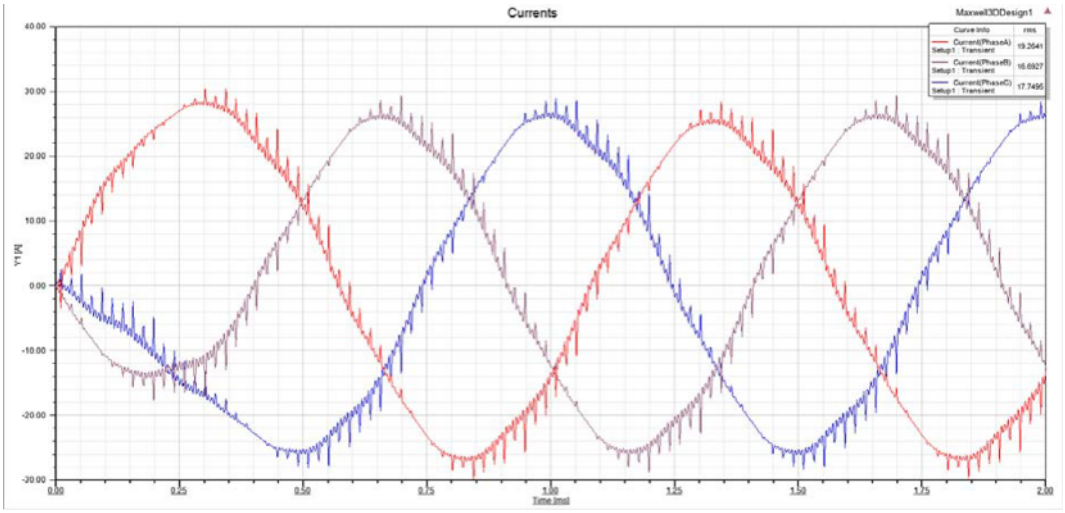

Figure 5-11: Phase currents vs. time

The winding currents are shown in Figure 5-11 and are close to sinusoidal as expected from the induced voltages. The value of the RMS Phase Current is 16.5 A. The harmonics present on the current waveforms are mainly as a result of the external driving circuit used in Ansys software. This is due to limitations with the 3D solver on star connected windings.

5.3.3. Machine Losses

The electrical losses are made up of eddy current, hysteresis and stranded copper (winding) loss. The core loss i.e. eddy current and hysteresis loss, occurs in both the stator and the rotor material. The stranded copper winding loss is obtained from the winding material in the stator. These losses are presented in Figure 5-12

Total Core Loss = 688 W

Stranded Winding Loss = 8.77 W

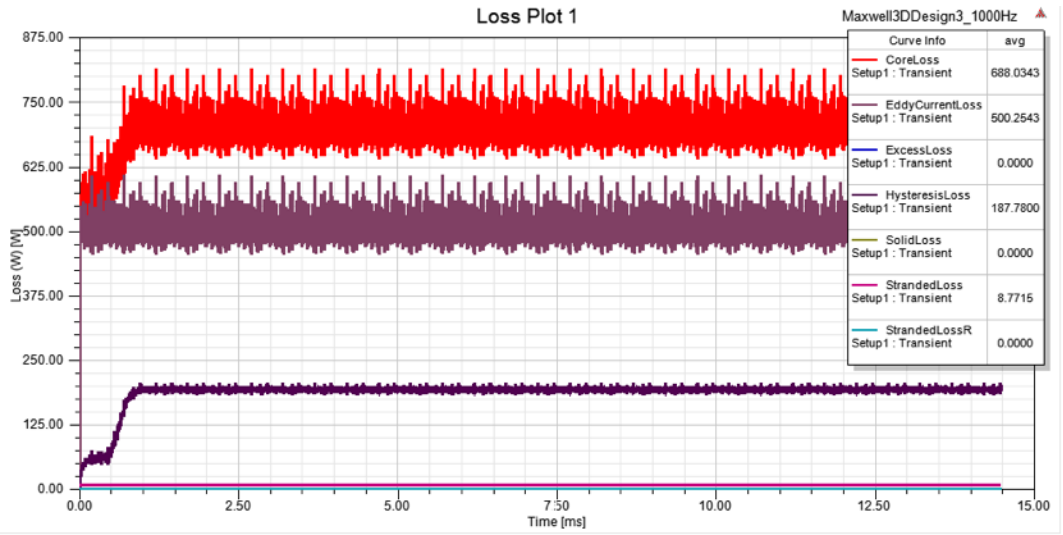

Figure 5-12: 3D Loss plot

5.3.4. Output Power

The machine produces an average output power of 9.9 kW at rated conditions as shown in Figure 5-13 i.e. averaged over steady state. With a total loss of 697 W (core loss and winding loss), the estimated machine efficiency is just about 90%, assuming mechanical losses amount to about 2% of rated power [83].

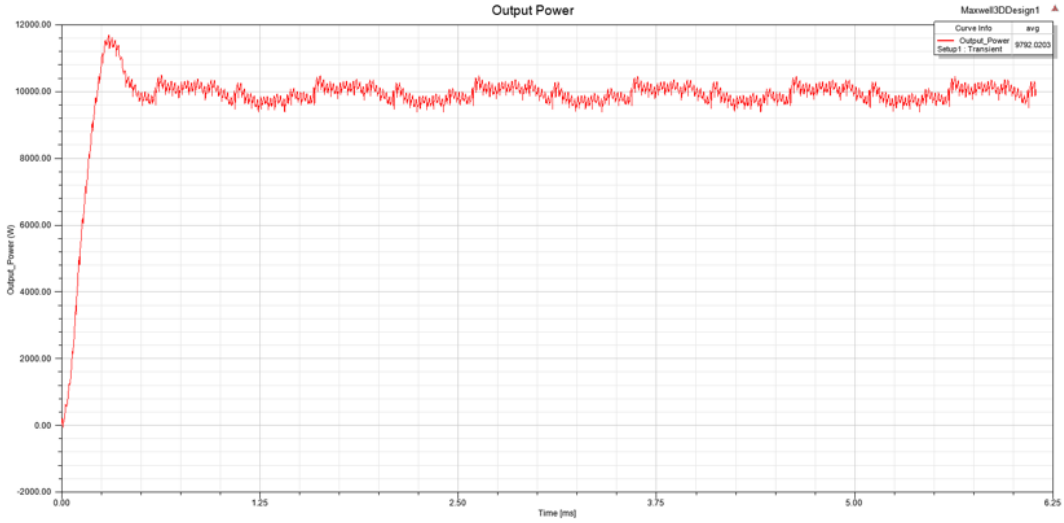

Figure 5-13: Output power vs. time

The output power from 3D simulations shows that the output power is slightly lower than the designed value of 10 kW. Ideally, the output power of the designed machine should be slightly higher than 10 kW to be able to compensate for losses within the machine and still maintain a high efficiency. However, the output power of the designed machine is 1% lower than the required output power. The core losses account for a larger percentage of the overall losses in the machine and significantly contribute to lowering the efficiency of the machine. Selection of an advanced high frequency electrical steel, though more expensive, is the best solution to lowering the core loss and hence increasing the efficiency of the machine. Further optimization of the machine would yield little benefit as the core loss is proportional to the frequency and flux density. This design was limited to the selection of a cost efficient electrical steel i.e. M19 29G. However, the 1% difference between the estimated and designed output power is still acceptable even with an estimation of mechanical and stray losses at 2% of total output power as recommended by [25], [83].

5.3.5. Comparison of analytical and simulated results

Table 5-1 compares the analytical results with the 2D and 3D FEA results. There is a high correlation between the results which confirms an accurate design of the machine.

Table 5-1: Comparison of analytical and FEA results

	Analytical	**2D FEA**	**3D FEA**
Average end-turn, l_e [m]	0.089	0.073	0.073
Phase Resistance, R_a [Ω]	0.0207	0.0209	0.0322
Airgap flux density, B_g [T]	0.56	0.57	0.57
Flux linkage Peak [Wb-turns]	0.0056	0.0069	0.0069
EMF, E_f [V]	218.31	218.83	218.93
Current, I_{rms} [A]	16.61	16.50	16.50
Torque, T [Nm]	3.18	3.1	3.1
Power, P_o [kW]	10	10.8	9.9
Core losses, P_c [W]	637.60	673.06	688.8
Copper losses Resistive, P_{cu} [W]	5.63	5.69	8.77
Efficiency [%]	**91.6**	**91.3**	**90**

It is imperative that the error between the analytical and FEA results be kept at a minimum for adequate validation of the design as full laboratory tests were not conducted on the machine prototype. A considerable discrepancy exists between the analytical and FEA values of resistive copper losses. This is as a result of the estimation of the winding length which is directly proportional to the phase resistance. The analytical and 2D estimation of the winding length assumes a circular path for the end turns for all the coils in the circuit. This tends to be inaccurate as the end turn length increases as more coils are wound, thereby increasing the total phase resistance and consequently the resistive copper loss. The core losses i.e. eddy current and hysteresis are analysed and estimated in chapter 6.

The efficiency estimated by the 2D and 3D FEA agrees with the analytical estimations. The slight discrepancies are as a result of the core loss estimations. The

3D FEA takes into consideration the effect of flux density along the axial length of the machine on the core loss. The analytical and 2D FEA results are based on a 2 dimensional analysis of the core loss in order to reduce the complexity of the analysis.

Chapter 6

6 Iron Loss Modeling

6.1 Overview of Iron Losses

The design of high-speed electrical machines imposes constraints on the rotor dimensions and generally subjects the machines to operation at high power density in order to meet performance specifications. This creates very high levels of thermal, electrical and mechanical stress which necessitate accurate prediction of losses in the machine. The accurate prediction of iron losses is essential for developing the cooling techniques as well as selection of the appropriate lamination material and machine geometry [88].

Iron losses constitute a larger portion of the total loss as compared to winding, friction and windage losses. Iron loss occurs when a magnetic material is subjected to a magnetic flux. Iron loss can be explained using the motion of magnetic domain walls under the influence of an externally applied magnetic field. When there is a change in the applied external field, movement of the magnetic domain walls occurs in order to achieve realignment. The energy dissipated as a result of the domain wall motion reveals itself as heat within the magnetic material and this is what is termed as the iron loss. It is generally influenced by the magnitude and the rate of change of the magnetic field and is also proportional to some function of the frequency of variation of the magnetic field [89].

This chapter presents the estimation of iron losses using various loss models from literature [89]–[92]. The loss models to be reviewed and analysed include; the original Steinmetz equation, Bertotti's modified Steinmetz equation as well as additional three term formulas. We will also look at how these models behave under a range of operating frequencies and flux densities; more specifically reviewing the behaviour of the loss coefficients as well as their formulations. Finally, an improved iron loss model with high accuracy is presented and a comparison made between analytical and

simulated values for different operating frequencies with sinusoidal and non-sinusoidal excitations.

6.2 Iron Loss Model Review and Analysis

6.2.1. Original Steinmetz's Two-Term Model

Steinmetz originally modelled the iron loss as a combination of two components: hysteresis loss P_h and eddy current loss P_e. However, Steinmetz original equation is only valid for low values of sinusoidal flux densities and low operating frequencies [89], [90].

$$P_c = P_h + P_e = k_h f B^n + k_e f^2 B^2 \tag{6-1}$$

Where P_c, P_h and P_e is the total loss per unit mass, hysteresis loss and eddy current loss respectively, n is the Steinmetz constant, B is the flux density, f is the frequency, k_h and k_e are the hysteresis and eddy current coefficient which are dependent on the properties of the lamination material.

Equation (6-1) assumes a static hysteresis loop and maximum flux density of about 1.0 T which is not practical in electrical machines especially at high frequency which is the case being considered. Another drawback to the model in (6-1) is that it does not take into account the anomalous/excess loss. The model assumes that the anomalous loss is lumped into the hysteresis loss term which brings in additional inaccuracies. The loss coefficients are obtained through regression analysis or experimental results obtained from the material manufacturer. Core loss per cycle is plotted against flux density at various frequencies and a mathematical expression is obtained through curve fitting. The material used in this study is M19 29 Gauge Non-Grain Oriented Silicon Steel.

Below is a graph showing the variation of total iron loss with flux density for different operating frequencies obtained from the manufacturers' data sheet.

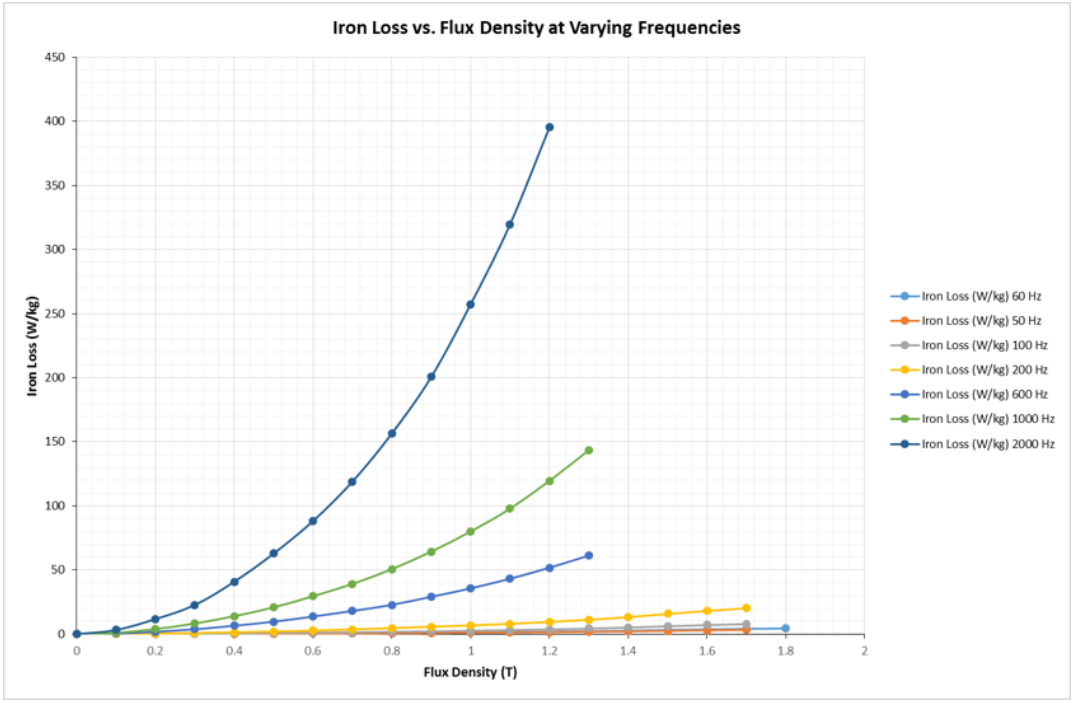

Figure 6-1: Iron loss vs. Flux density

It is evident that iron loss increases with frequency from Figure 6-1. The loss as a result of eddy currents is proportional to the second power of frequency and flux density and therefore accounts for a larger percentage of the total iron loss at higher frequencies. From the figure above it is also evident that a linear model of the iron loss would only be applicable at lower frequencies. At higher frequencies, the iron loss adopts a more exponential curve with an increase in flux density.

To obtain the loss coefficients, (6-1) is divided by frequency f and reduces to

$$P_c/f = P_h/f + P_e/f \qquad (6\text{-}2)$$

$$= k_h B^n + k_e f B^2$$

which is a linear equation of the form $D = Ef + G$ in frequency at each flux density B.

The values of k_e and k_h were calculated using two selected values of flux density at f of 1000 Hz. The loss coefficients were recalculated at each frequency in order to achieve more accurate loss estimates.

$k_h = 0.0224$	$k_e = 6.02\times10^{-5}$	$n = 1.51$

Figure 6-2 shows plots of the iron loss vs flux density at two frequencies (i.e. low and high frequency).

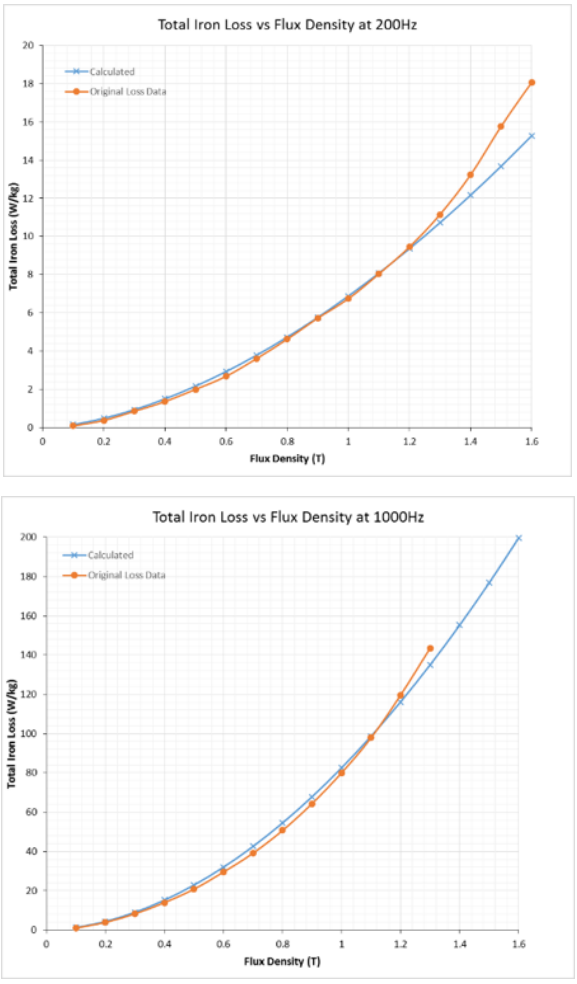

Figure 6-2: Iron loss vs. flux density at two frequencies

It can be seen that there is a deviation between the calculated and original loss data. It is also evident that there is a slightly better agreement between the original loss data and the calculated loss data at low flux densities than higher flux densities. The graph is seen to deviate further at flux densities beyond 1T, especially at points closer to

saturation. This statement is true even for variations in frequency. If we take for example, *B* of 1.2T, the % Error is about 0.96% at 200Hz and 2.95% at 1000 Hz.

6.2.2. Modified Steinmetz's Two-Term Model

Various models have been proposed in literature for the modification and correction of the original Steinmetz's model. However, these models still do not accurately predict the iron loss as the excess loss is not explicitly accounted for. The model still assumes a sinusoidal flux density wave form and is given by [90]:

$$P_c = k_h B^{a+bB} f + k_e B^2 f^2 \tag{6-3}$$

Where *a* and *b* are constant terms. The exponent coefficient in the hysteresis component, changes linearly with flux density. The Steinmetz's constant now varies with flux density in order to cater for different lamination materials.

To obtain the coefficients, (6-3) is divided by *f* which gives

$$\frac{P_c}{f} = k_h B^{a+bB} + k_e B^2 f = G + Ef \tag{6-4}$$

Equation (6-4) is a linear relationship between specific iron loss and frequency at different flux densities. The intercept *D* on the vertical axis of P_c/f vs *f* must be equal to the hysteresis loss i.e. $D = k_h B^{a+bB}$. At least three flux densities are selected and their curves extrapolated, yielding three different values of *D*, which represents the hysteresis loss component as described above. Using logarithmic expressions from the three selected flux densities, k_h, *a* and *b* can be calculated. The slope of each of the three curves is equal to the eddy current loss coefficient k_e and can be taken as an average value.

k_h = 0.024	*a* = 1.69	*b* = -0.15	k_e = 4.95e-05

Figure 6-3 displays a comparison of the loss data against calculated loss using equation (6-3). The Steinmetz's model (6-1) prediction is better than the modified two term model in (6-3) at high flux densities. This could be attributed to the calculation of the loss coefficients and exponents, and that they are kept constant over the entire

flux density range of operation. Also, this model does not take into account the contribution from excess loss component.

On the other hand, the model in (6-3) displays a better prediction across the low flux density range. One of the limiting factors in this comparison is that the manufacturers loss data does not contain loss data at high flux densities i.e. > 1.3T, especially for high frequencies.

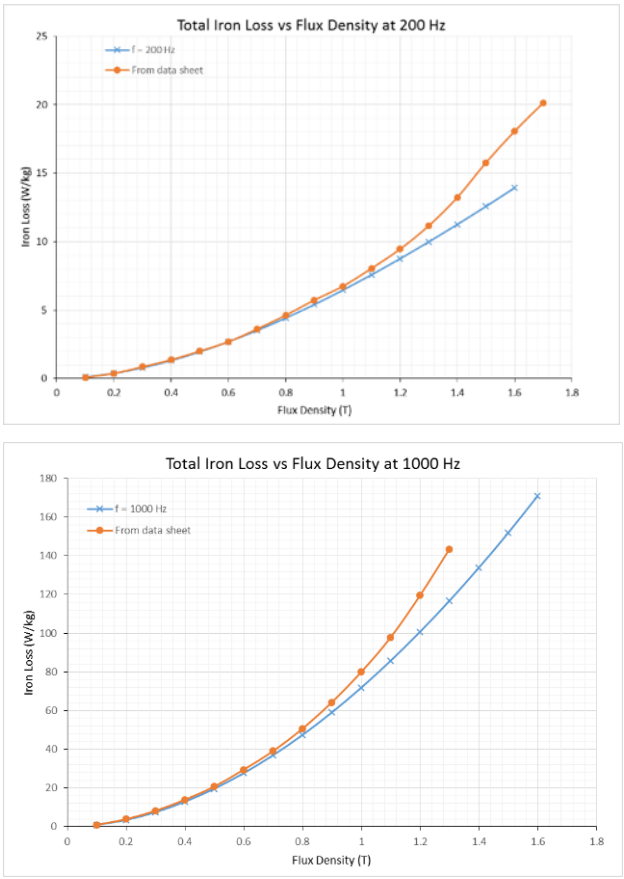

Figure 6-3: Steinmetz model comparison at 200 Hz and 1000 Hz

Equations (6-1) and (6-3) still under estimate the iron loss at the frequencies in consideration. The error between measured and calculated loss increases further at high frequency and high flux density i.e. at 1.2T, % error of 8.1% at 200 Hz compared to 18.7% at 1000 Hz.

6.2.3. Bertotti's Three-Term Model

The existence of the excess loss component justified the derivation of Bertotti's three-term mode. Bertotti carefully studied different materials using the statistical loss and domain wall theory. The theory assumes that the magnetic objects found in the magnetic domain structure tend to expand and/or collapse when a magnetic field is applied thereby resulting in loss. The modified core loss formula according to Bertotti is given by

$$P_c = k_h B^2 f + k_e B^2 f^2 + k_a B^{1.5} f^{1.5} \quad (6\text{-}5)$$

Where k_a is the anomalous (excess) loss coefficient which is dependent on material conductivity, thickness, cross-sectional area and is a function of the peak flux density. According to [89], the formula is in good agreement with several core loss tests. However, a few deviations have been observed thereby displaying the dependence of k_a on flux density.

To obtain the coefficients, a similar approach as in section 6.2.2 is taken. The three term model equation is divided by *f* to obtain a polynomial equation in terms of $\sqrt{f}$ as can be seen below

$$\frac{P_c}{f} = k_h B^2 + k_e B^2 f + k_a B^{1.5}\sqrt{f} = D + E\left(\sqrt{f}\right)^2 + G\sqrt{f} \quad (6\text{-}6)$$

By comparing the LHS and RHS of (6-6), the coefficients of Bertotti's three-term model can be obtained for given flux densities. Bertotti approximated the exponent of flux density in the hysteresis loss component to be equal to '*2'* i.e. *n=2*. It is clear from Figure 6-4 that the three-term formula predicts the core loss better than Steinmetz's two-term model described earlier in (6-1).

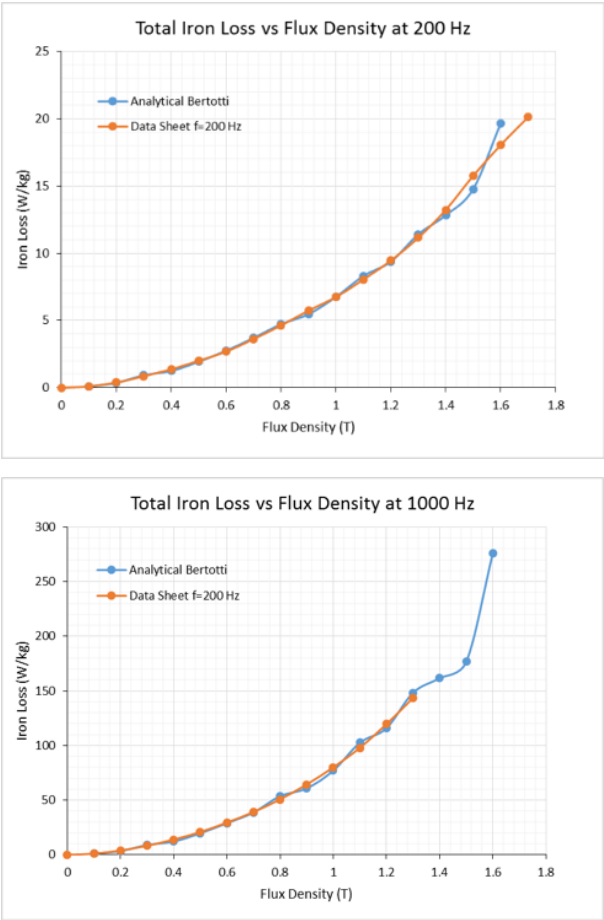

Figure 6-4: Bertotti's three-term model comparison at 200 Hz and 1000 Hz

From above, the estimation using Bertotti's model also deviates at high flux densities. It is, however, better than Steinmetz two-term model. At a flux density of 1.2T, there is an error of 0.95 % at 200 Hz and 3.15 % at 1000 Hz between the analytical and measured results. This slight deviation can be attributed to a poor approximation of the flux density exponent in the hysteresis loss. Also, it could be as a result of the curve fitting technique used and insufficient data points at higher flux densities. Further examination of the two curves from both models also shows that the three-term model agrees well with the measured core loss across a wider range of flux densities at low and high frequencies. It is evident that the presence of the excess loss component also accounts for the difference between measured and calculated values in the previous two term models.

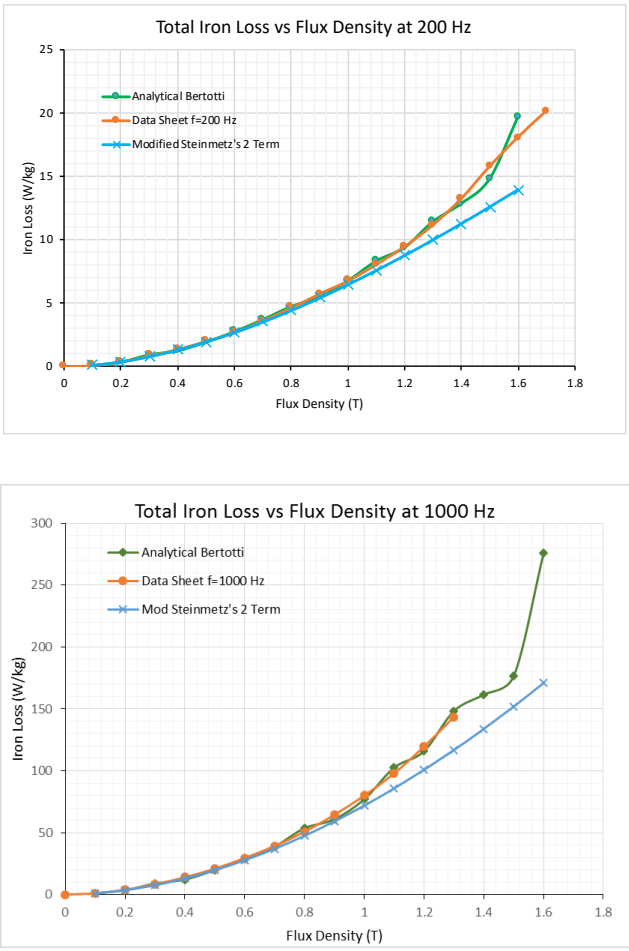

Figure 6-5: Bertotti vs. Steinmetz's model at 200 Hz and 1000 Hz

Comparison of the two models against the measured data is shown in Figure 6-5. It is more evident that the Bertotti model matches the measured data better than the Steinmetz 2 term model. It is also worth noting that the accuracy of the model also largely depends on the estimation of the loss coefficients i.e. k_h, k_e *and* k_a. These are functions of both frequency and flux density as shown in previous sections.

6.3 Estimation of Core Loss in a Machine

In this chapter, a core loss model based on work done by [90] is introduced and applied to different cases for the evaluation of core losses. The core loss models are developed for the different areas of the machine. A tooth core loss model is developed that is as a result of the radial component of flux density which is dominant in the tooth. A correction factor is introduced to account for the loss induced by the circumferential component of flux density.

Another model is developed for the core loss in the stator yoke resulting from contributions from both the circumferential and radial components of flux density. The waveform of the circumferential component of flux density in the stator yoke can be approximated by a trapezoidal waveform. This waveform has the same shape as that of the radial component of the tooth flux density waveform. In this case as well, a correction factor is introduced to account for the geometry influencing the two components of the flux density in the stator yoke. These models simplify the calculation of core losses in PM machines and can be utilized to save computational time whilst still providing high accuracy as compared to FE methods.

Estimation of the rotor loss is not included in this model as the flux density is in synch with the rotor hence the variation in flux density can be assumed to be negligible.

The linear synchronous motor was used as an example to better understand the core loss model and was then adapted to the case of rotary machines. The flux distribution in the linear PM motor is as shown below:

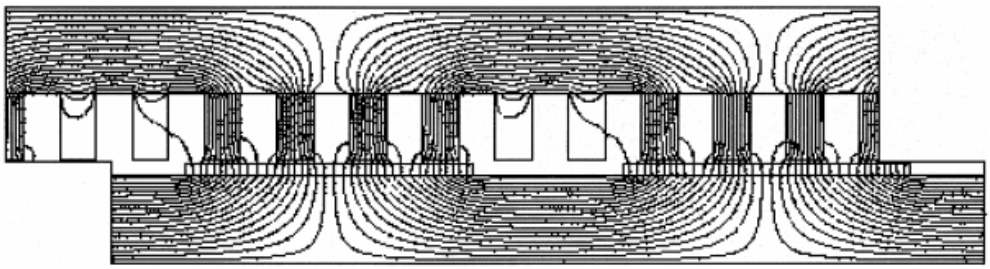

Figure 6-6: Linear PM motor flux distribution [90]

From Figure 6-6, it can be seen that the flux density travels from the magnets into the stator teeth and finally distributed into the yoke. The magnetic flux in the stator teeth

is fairly uniform and in the radial direction above the magnets and is essentially zero in between the magnets.

In the yoke region above the teeth i.e. where it is above the magnet, the flux transitions from the radial direction to the circumferential direction. As it travels further into the yoke, towards the space between magnets, the flux density can be seen as predominantly circumferential and uniformly distributed over the yoke thickness.

6.3.1. Tooth Eddy Current Loss Model

The understanding developed from the linear PM motor in the previous section was applied to a radial flux PM machine as in our case. The flux lines flow in a similar manner to the linear PM motor as can be seen in Figure 6-7 below. The difference in this case is the presence of the shoe area of the teeth where the flux is a combination of the radial and circumferential components as compared to only the radial component as in the case of the linear PM motor.

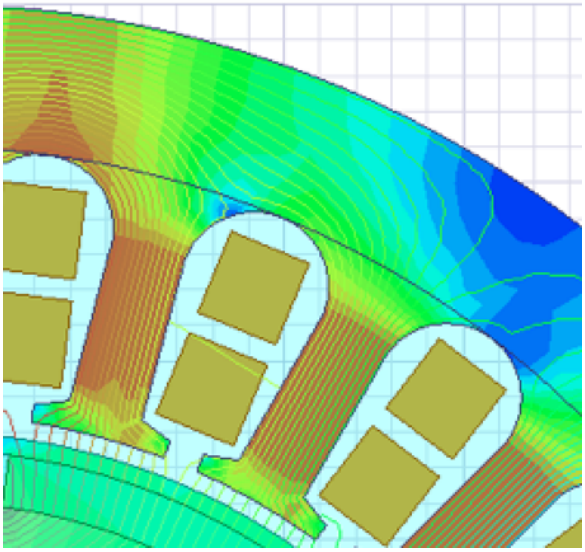

Figure 6-7: Movement of flux lines in SPM

The flux density waveform in the tooth as well as other parts of the stator being considered, has to be carefully studied in order to fully understand the core loss model. The following is the behaviour of the flux density waveform in the tooth;

- The flux density in a tooth follows a trapezoidal shape. It rises linearly at the leading edge of the magnet to a maximum and stays constant as the magnet

traverses the tooth until the lagging edge where the flux density falls from maximum to zero. This waveform is mirrored about the x-axis for alternate poles.

- Following the above statement, the core loss is highest at the teeth near the edges of the magnets i.e. $\frac{dB}{dt}$ is maximum.
- The time taken for the flux density to change from maximum to zero or vice versa is equal to the time taken for the magnet edge to traverse the slot width.

The flux density waveform of the radial component of flux density obtained using FEA is shown below. The flux density was extracted at the centre of a tooth and follows an approximately linear pattern which can be shown by the linear approximation lines.

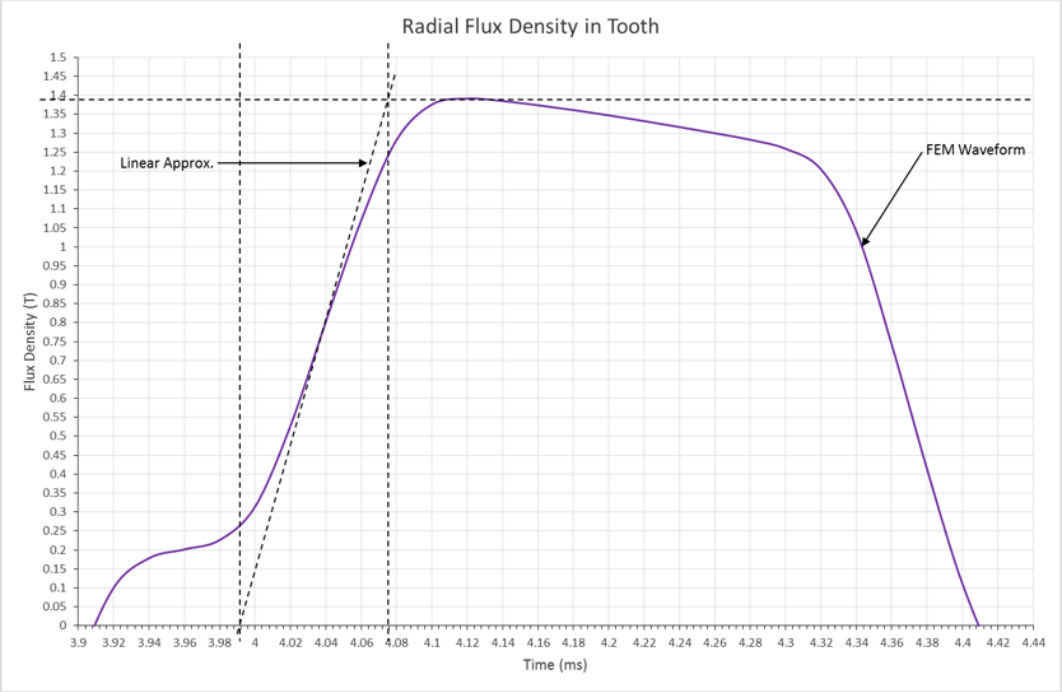

Figure 6-8: Radial flux density waveform in tooth

To obtain the rise time of the linear approximation of the flux density waveform, the eddy current loss obtained by FEM was equated to the eddy current loss calculated by the linear approximation. This ensures that we obtain an accurate representation of the linear approximation of the flux density waveform. It was found that the rise time is equivalent to the slot width in this case.

Other linear approximations of the flux density waveform were tested i.e. extending the linear part of the flux density waveform and assuming a rise time equivalent to a tooth width. Both cases resulted in a larger error between the analytical and FEM results.

Table 6-1: Approximation of waveform rise time

	Rise Time Approx.		
	Slot Width	**Tooth Width**	**Waveform Extension**
FEM	32.58 W	32.58 W	32.58 W
Analytical	30.67 W	67.93 W	22.64 W
% Difference	-6.04 %	70.34 %	-36 %

From Table 6-1, the approximation assuming a rise time equivalent to one slot width reflects the best linear approximation of the flux density in the tooth. The slight difference between the analytical and FEM calculation is because FEM takes into account the contribution of the circumferential flux density component which is present in the tooth tip.

The change in flux density from zero to peak and vice-versa happens two times every cycle or time period i.e. four changes per period. Equation (6-7) is used to evaluate the eddy current loss induced by the radial component of flux density [90].

$$P_{etr,APP} = \frac{2k_e}{T} V_t \int_0^T \left(\frac{dB_x}{dt}\right)^2 dt = \frac{2k_e}{T}\left(\frac{B_{th}}{\Delta t}\right)^2 (4\Delta t) V_t = \frac{8k_e}{T}\frac{B_{th}^2}{\Delta t} V_t \tag{6-7}$$

Where Δt is the rise time of flux density

B_{th} is the plateau value of flux density

V_t is the volume of the teeth and T the time period

It can be concluded from equation (6-7) that the eddy current loss induced in the tooth is inversely proportional to the rise time of the linear approximated flux density waveform.

6.3.2. Simplified Tooth Eddy Current Loss Model

As it has been discussed in the previous section, the radial component of the tooth flux density waveform can be approximated by a linear trapezoidal waveform with a rise time equivalent to one slot pitch i.e. the time taken for the flux density to rise from zero to maximum is equivalent to the time taken for the magnet edge to traverse one slot pitch.

With the understanding gathered from the previous section, we can estimate the rise time analytically using equation (6-8) for an 'm-phase' PM motor with q slots per pole per phase.

$$\Delta t = \frac{T}{2}\frac{1}{mq} \tag{6-8}$$

Substituting the equation for Δt from (6-8) into (6-7), we obtain an estimation for the tooth eddy current loss induced by the radial component of flux density expressed by:

$$P_{etr} = \frac{12}{\pi^2} q k_e (\omega_s B_{th})^2 V_t \tag{6-9}$$

This shows that the tooth eddy current loss is proportional to q (slots per pole per phase) for given operating frequencies. An increase in q will result in a substantial increase in the tooth eddy current loss induced by the radial component of flux density.

6.3.3. Effect of Machine Dimensions on Tooth Loss

This section examines the effect of selected design parameters on the tooth eddy current loss. The selected parameters are critical in the initial design stage of machines as well as in validating the approximate linear model of the flux density waveform in the tooth. Their effect on the flux density waveform as well as eddy current loss induced is considered.

a. Effect of Slot Opening Width

The slot opening width was varied while keeping other dimensions constant. The radial component of the flux density at the centre of the tooth is shown below for variations of the slot opening.

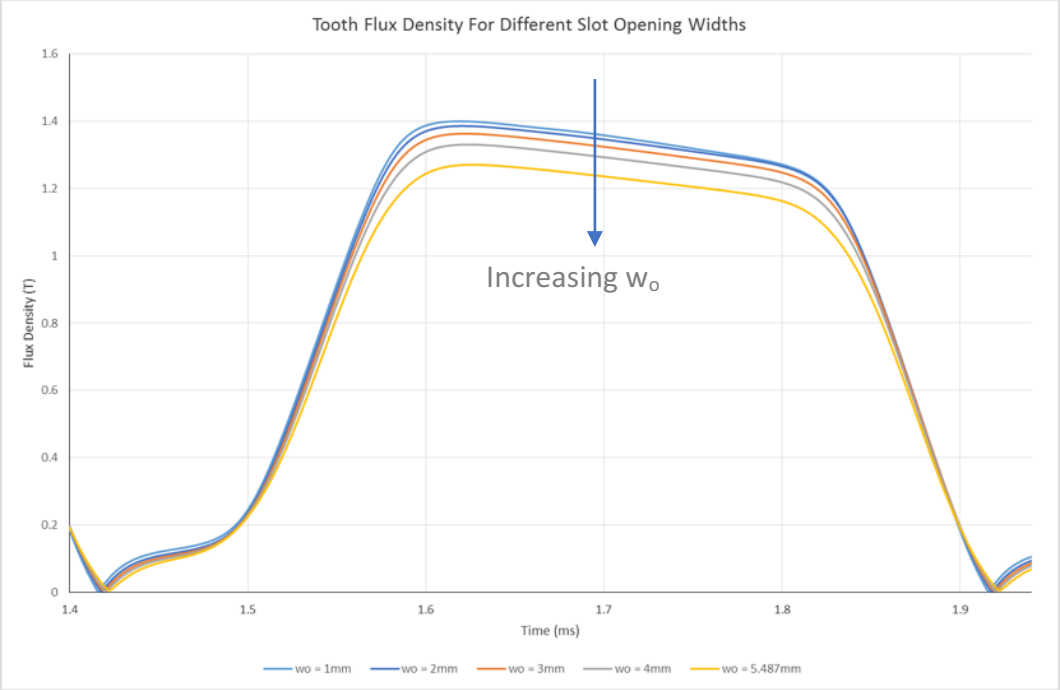

Figure 6-9: Tooth flux density for varying slot opening widths

From top to bottom, the width of the slot opening is 1mm, 2mm, 3mm, 4mm and 5.487mm (open slot). The slope of the waveform is similar whereas the plateau value differs as the slot opening width is varied.

As the slot opening width is increased, the effective airgap reluctance increases causing a decrease in flux density in the tooth. It can also be deduced from Figure 6-9 that the rise time of flux density can be assumed to be independent of the slot opening width.

Figure 6-10 displays the change in tooth eddy current loss as the slot opening width is varied.

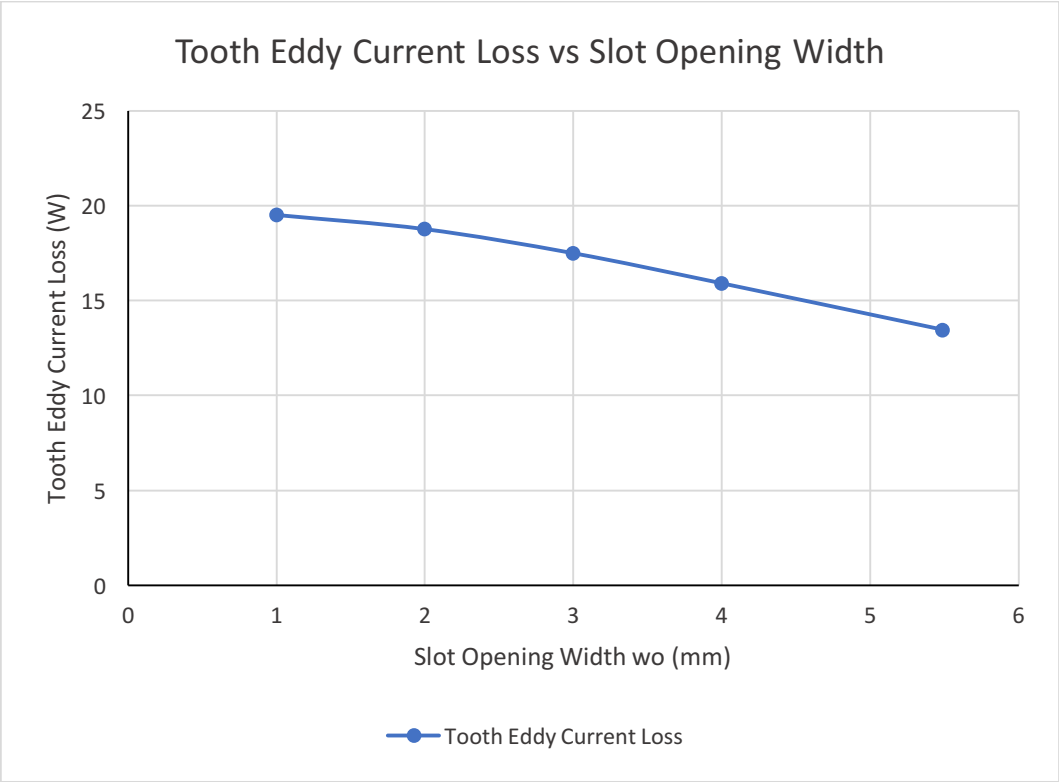

Figure 6-10: Tooth eddy current loss vs. slot opening width

b. Effect of Pole-arc

As explained earlier, the tooth eddy current loss occurs when there is a change in the flux density i.e. at the leading and trailing edges of the magnets. We can therefore assume that the eddy current loss would be independent of magnet coverage (pole-arc).

The magnet coverage was examined from full pole pitch to the equivalent of a slot pitch of the machine being considered.

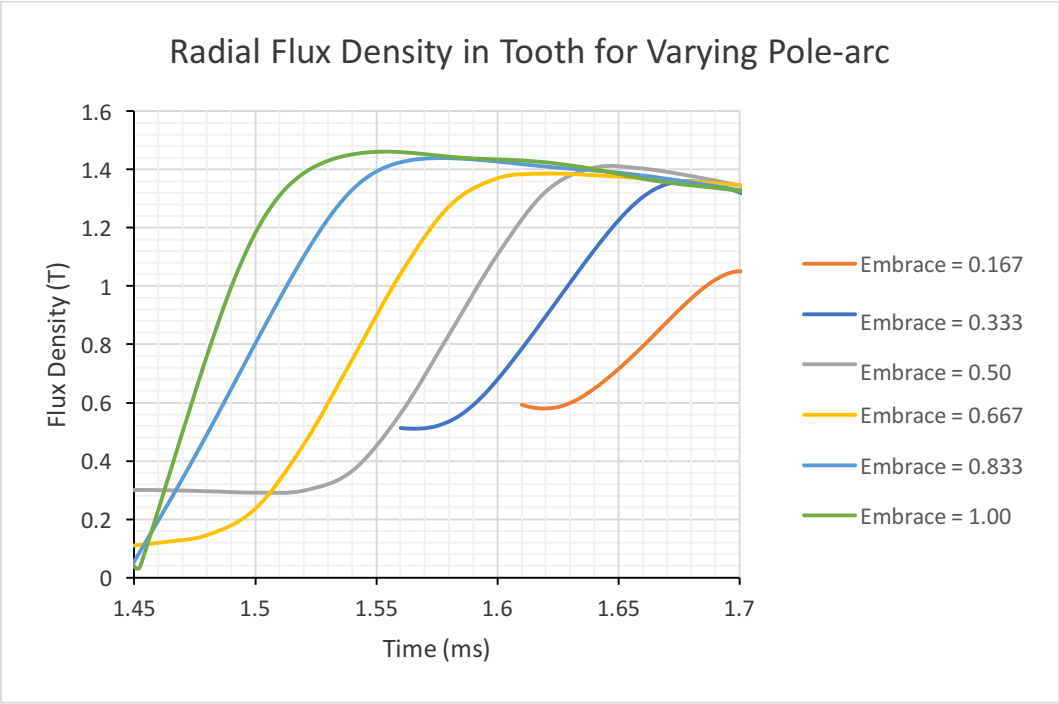

Figure 6-11: Radial flux density in tooth for varying pole-arc

For different magnet coverage, the tooth flux density is observed to have the same plateau flux density except for the smallest magnet coverage of 0.167. Another observation is that the highest pole-arc of 1 is seen to have a different slope. It can be concluded that the linear approximation of the flux density waveform would only be valid for pole embrace less than or equal to 0.833 and greater than 0.167 which is less than a slot pitch. At a pole embrace greater than 0.833, the space between two magnets is less than a slot pitch and the slope of the radial component increases significantly.

Figure 6-12 below shows the variation of *dB/dt* and the magnet pole-arc where *dB/dt*, as in Equation (6-7), is the slope of the linear part of the radial flux density waveform in the tooth.

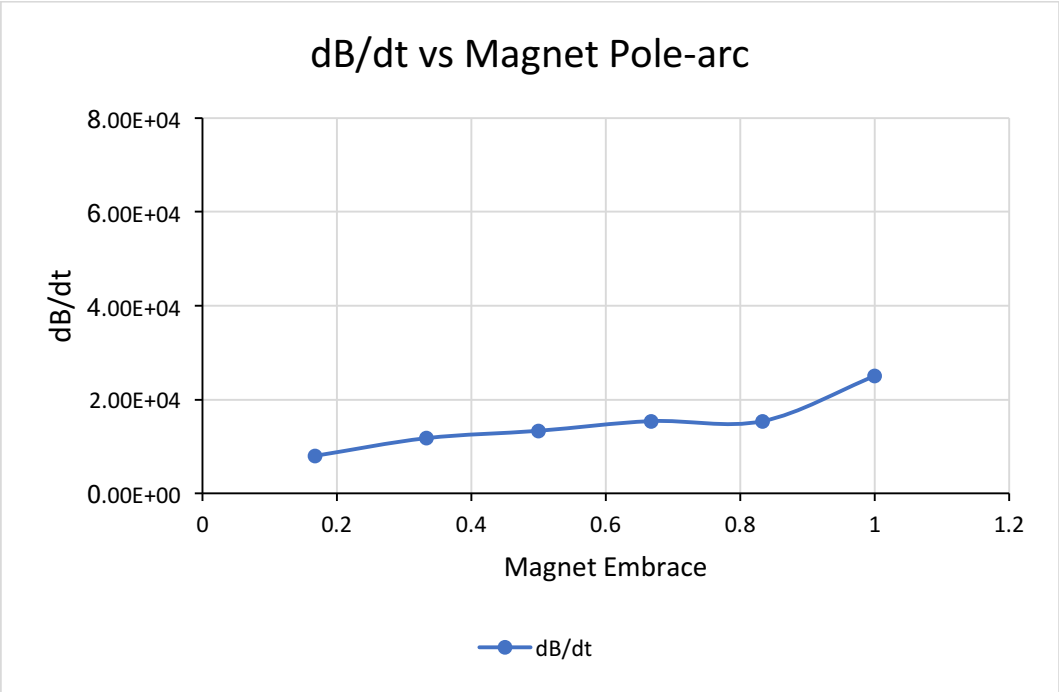

Figure 6-12: dB/dt vs. magnet pole-arc

This also confirms that the losses will remain relatively constant as the tooth eddy current loss is proportional to the slope of the radial component of the flux density waveform as in equation (6-7). A pole embrace greater than 0.833 effectively creates a space in between the magnets that is less than about a slot pitch and eliminates the slow change in flux density with time as the magnet edge approaches the tooth.

Therefore the use of short pitched magnets as opposed to full pitched magnets would not only eliminate leakage flux between the poles but also reduce the eddy current loss in the stator teeth.

c. Effect of Airgap Height and Thickness of Magnet

This section details the investigation of the magnet thickness and airgap height on evaluation of a correction factor k_q. Here, k_q is introduced by equating the loss obtained by FEA to the approximated eddy current loss, resulting in (6-10). The correction factor to the approximation model was shown to be a function of magnet height, airgap length and slot pitch.

$$k_q = \frac{\pi^2 P_{etr,FEM}}{12 q k_e (B_{th}\omega_s)^2 V_t} \tag{6-10}$$

The correction factor was obtained for a wide range of combinations of magnet thickness and airgap height. The analysis was performed on a linear PM motor and can be applied to radial PM motors although the variation of k_q in the latter case is usually in the range 0.85 to 1.15. Figure 6-13 below shows the relationship of k_q vs airgap height (δ) and magnet thickness (l_m) for a fixed slot pitch (λ).

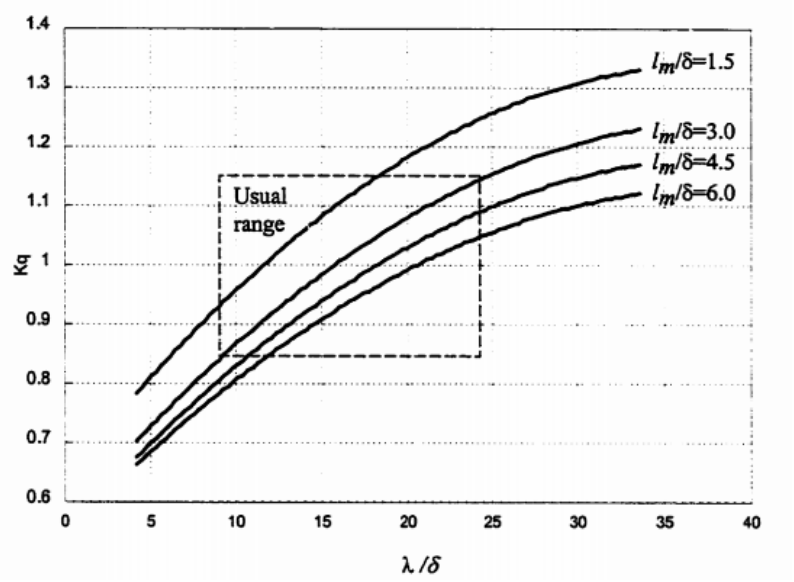

Figure 6-13: Correction factor k_q - varying magnet thickness and airgap height

6.3.4. Circumferential Component of Flux Density on Eddy Current Loss

The flux density in the stator tooth comprises the radial and the circumferential component. The radial component is dominant in the centre of the tooth whereas the circumferential component dominates the tooth shoes as the flux flows from the airgap.

The circumferential component of flux density follows a more complex pattern and therefore cannot be approximated linearly as with the radial component. Another correction factor k_c is introduced to account for the eddy current loss induced by the circumferential component from the approximate linear model. The total eddy current loss in the tooth is shown by:

$$P_{et} = P_{etr} + P_{etc} = P_{etr}\left(1 + \frac{P_{etc}}{P_{etr}}\right) = k_c P_{etr} \tag{6-11}$$

Where;

P_{etc} is the eddy current loss induced by the circumferential component

P_{etr} is the eddy current loss induced by the radial component and k_c is the correction factor.

The circumferential component is significantly influenced by the slot opening width. Increasing the slot opening width in turn reduces the width of the tooth shoe (tooth tip) and eventually reduces the circumferential component of flux density in the tooth. An increase in the slot opening leads to an increase in the airgap reluctance thereby forcing more flux radially along the tooth. Additionally, the tooth tip area is reduced resulting in a smaller proportion of the flux density transitioning from radial to circumferential at the tooth tip.

The correction factor k_c was found to be a function of the relative slot closure (width of the tooth tip) and is shown in Figure 6-14 [90]:

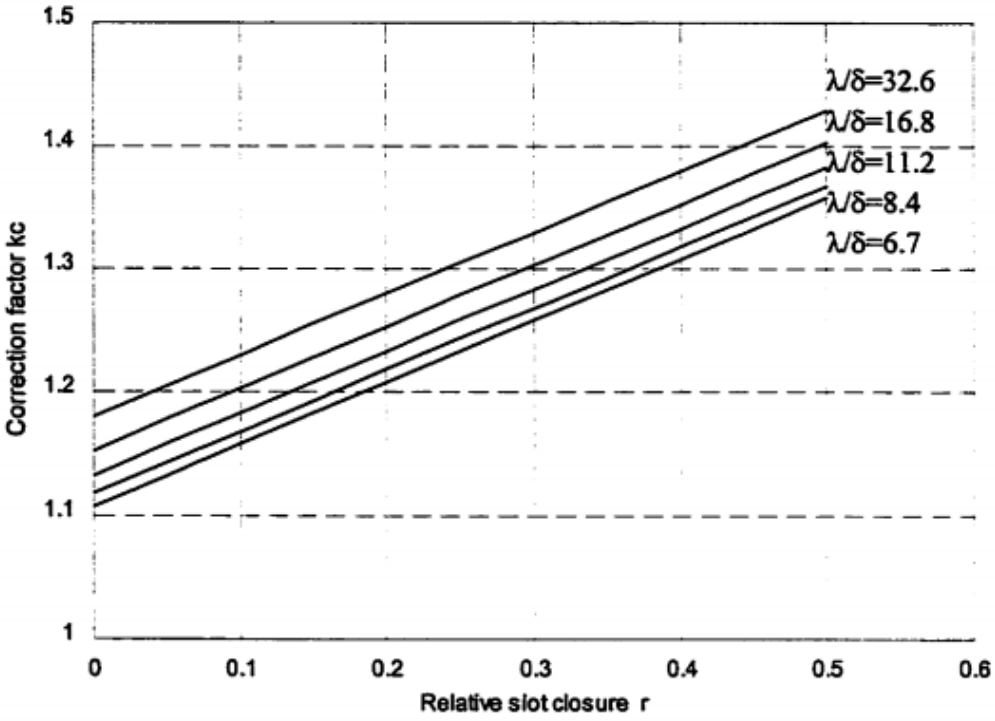

Figure 6-14: Correction factor k_c for varying slot closure [90]

A more accurate approximation of the tooth eddy current loss can now be obtained with the inclusion of the two correction factors [90]:

$$P_{et} = \frac{12}{\pi^2} q k_q k_c k_e (\omega B_{th})^2 V_t \tag{6-12}$$

Where;

k_e is the eddy current loss coefficient

k_q & k_c are the correction factors which can be estimated using Figure 6-13 and Figure 6-14 respectively.

Expressing (6-12) as a function of speed shows that the eddy current loss is proportional to the number of poles squared and slots per pole per phase [90].

$$P_{et} = \frac{qp^2}{300} k_q k_c k_e n^2 B_{th}^2 V_t \tag{6-13}$$

Where n is the speed in revolutions per minute

The tooth eddy current loss model developed in the previous section (from Figure 6-8) was used to estimate the eddy current loss in the tooth of the designed 4-pole PM machine. Using Figure 6-13 and Figure 6-14, the two correction factors k_c and k_q were obtained from the following machine dimensions; $l_m/\delta = 1.5$, $\lambda/\delta = 6$ and $\gamma = 0.36$.

Table 6-2: Approx. Tooth Eddy Current Loss at 1000Hz

Tooth Eddy Current Loss Model Comparison	
k_q	0.82
k_c	1.29
FEM Tooth Eddy Current Loss (W)	32.58
Approx. Model Tooth Eddy Current Loss (W)	32.44
Error (%)	-0.43

It can be seen from Table 6-2 that the approximated tooth eddy current loss model is in good agreement with the loss calculated using FEM.

6.3.5. Yoke Eddy Current Loss Model

As with the tooth eddy current loss model, the yoke eddy current loss model also includes contributions from both the radial and the circumferential component of flux density. As stated in the previously, the circumferential component of flux density is dominant in the stator yoke.

The assumption by [91] is that the yoke flux density can be approximated by a trapezoidal waveform and the eddy current loss calculated using the average value of flux density in the yoke. However, the flux density is slightly different when obtained above the slots and above the teeth. The yoke flux density above the slots is purely circumferential as compared to the yoke flux density above the teeth which comprises both the radial and circumferential component.

Figure 6-15 shows the circumferential component of flux density obtained above a tooth.

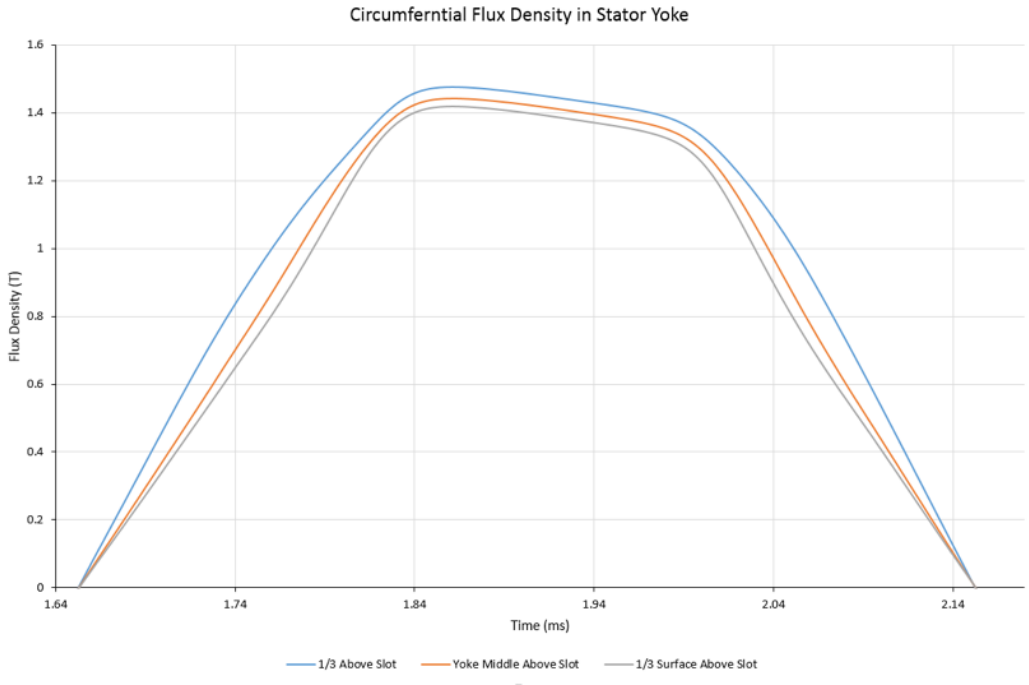

Figure 6-15: Circumferential flux density in stator yoke

The initial assumption described above agrees with the waveform extracted from FEA for the circumferential flux density obtained in the yoke. The flux density has a rise time approximately equal to the time taken for half the magnet width to traverse a given point in the stator yoke. Using the flux density obtained above the slot, the rise time of the approximate model was determined.

The time taken for the flux density in the stator yoke to change from $-B_c$ to B_c or vice versa is equal to the time required to traverse the magnet width and is given by:

$$\Delta t = \frac{w_m}{2r\,\omega_s/p} = \frac{\alpha\pi}{\omega_s} \tag{6-14}$$

Where w_m is the magnet width, ω_s is the rotational speed and α is the pole embrace

The pole embrace, α, is the ratio of the magnet width to the full pole pitch:

$$\alpha = \frac{w_m}{\tau} = \frac{w_m}{2\pi r/p} = \frac{pw_m}{2\pi r} \tag{6-15}$$

Therefore, the rate of change of flux density with time i.e. rise time can be expressed as:

$$\frac{dB}{dt} = \frac{2\hat{B}_c}{\Delta t} = \frac{2\omega_s \hat{B}_c}{\alpha\pi} \tag{6-16}$$

The total yoke eddy current loss induced by the circumferential component of flux density can be expressed as below considering that the change in flux density occurs twice per period [90].

$$P_{eyc} = 2k_e \left(\frac{dB}{dt}\right)^2 \frac{2\Delta t}{T} V_y = \frac{1}{\alpha}\frac{8}{\pi^2} k_e \omega_s^2 \hat{B}_c^2 V_y \tag{6-17}$$

According to (6-17), the eddy current loss induced by the circumferential component in the yoke is proportional to the inverse of the pole embrace and not any other machine dimensions.

6.3.6. Effect of Machine Dimensions on Yoke Eddy Current Loss

A study on the effect of machine dimensions on the eddy current loss in the stator yoke was conducted. This was done in order to validate the conclusions made in the previous section relating to (6-17).

a. Effect of Slot Opening Width

In this section, the yoke circumferential flux density waveform obtained using FEA was compared to the approximate model with particular focus on the slope of the flux density waveform. This enables us to determine whether a change in the slot opening width would invalidate the approximate model of flux density. Below is a table with variations of the slot opening width:

Table 6-3: Effect of variation of slot opening width on circumferential flux density

Slot Opening Width (mm)	1.0	2.0	3.0	4.0	5.5 (open)
Yoke Fux Density (T)	1.45	1.44	1.40	1.37	1.30
Δt Analytical (ms)	0.33	0.33	0.33	0.33	0.33
Δt by Approximation Model (ms)	0.35	0.35	0.35	0.34	0.35
Difference (%)	5.88	5.88	5.88	5.88	5.88

From the table above, the slope of the flux density waveform (*dB/dt*) obtained from FEA remains constant as the slot opening width is varied. Therefore, the slot opening has no effect on the approximate model of the circumferential flux density waveform.

b. Effect of Magnet Pole Embrace

The yoke eddy current loss was found to be inversely proportional to the magnet pole embrace in (6-17). In this section, the eddy current loss in the yoke is observed while the magnet pole embrace is varied from 0.167 to 0.833.

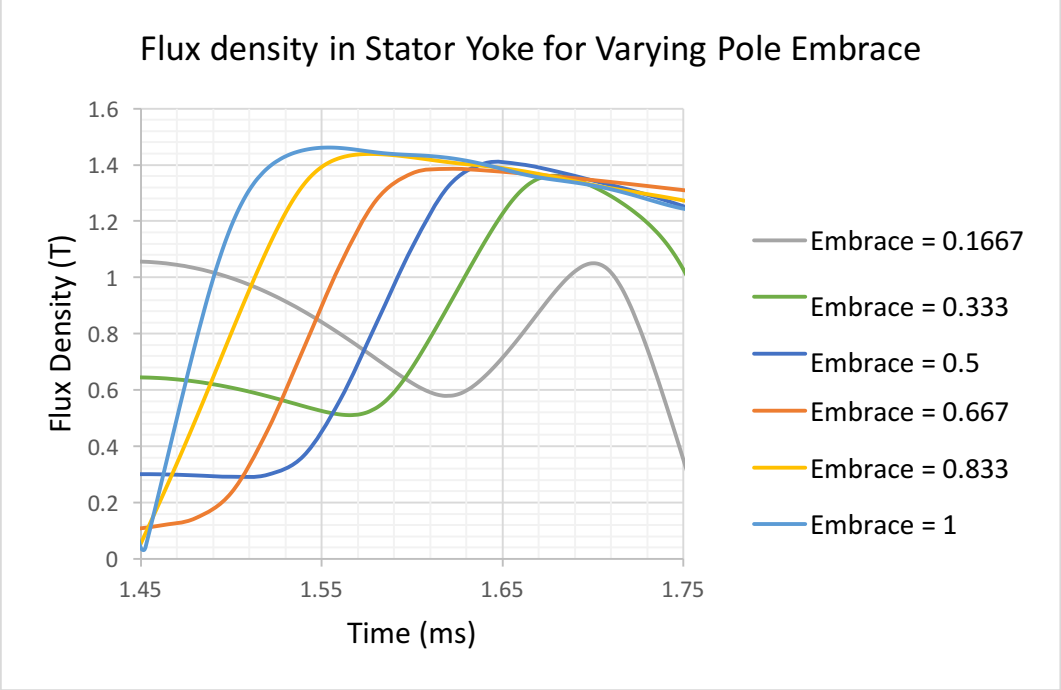

Figure 6-16: Flux density in stator yoke for varying pole embrace

Results from the graph above show that the slope of the flux density remains relatively constant over a variation of the magnet embrace. The eddy current loss in the yoke decreases with an increase in the magnet pole embrace. An increase in the magnet pole embrace results in a shorter distance between magnet poles thereby increasing the leakage flux between the poles. This further leads to a reduction in the flux density in the stator yoke. Figure 6-16 also confirms that the eddy current loss in the yoke is independent of the slope of the flux density waveform which is seen by the relatively constant *dB/dt*. Although the peak flux density in the stator yoke is seen to reduce with an increase in the pole embrace, it is not significant enough to foster a considerable decrease in the eddy current loss. Therefore, we can conclude that the pole embrace has negligible effect on the approximate model.

c. Yoke Flux Density Waveforms at Different Layers

Compared to the flux density in the stator teeth, the flux density in the stator yoke follows a different pattern although of the same shape. The tangential component of flux density in the stator yoke assumes a trapezoidal shape and is relatively constant over the thickness of the stator yoke.

However, the radial component of flux density in the stator yoke is observed to differ in terms of the plateau value over the thickness of the yoke. It is seen to be maximum near the stator teeth and reduces further into the yoke and approaches zero closer to the surface of the stator yoke.

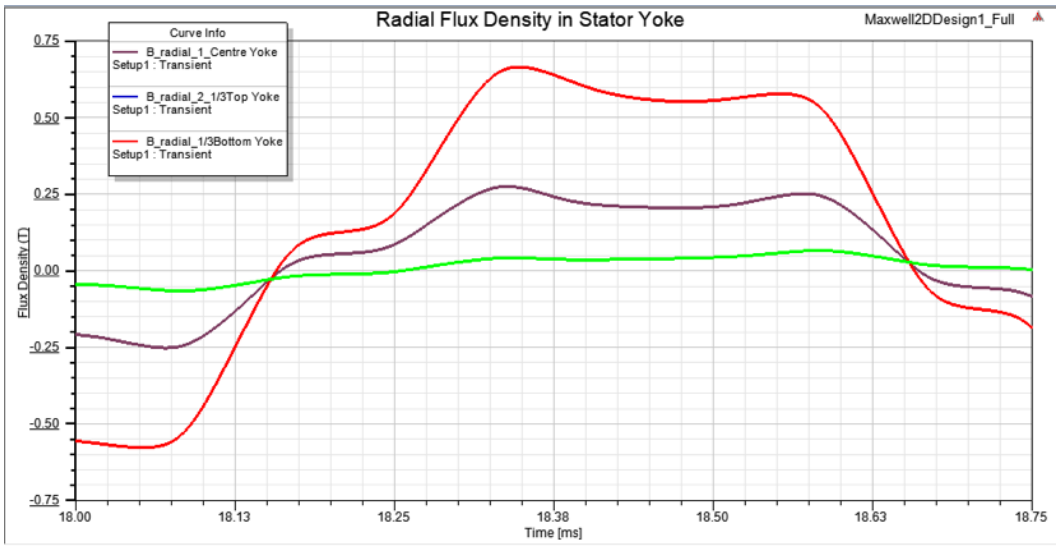

Figure 6-17: Radial flux density in Stator yoke

Integrating the loss over the entire yoke allows us to account for the difference in plateau values of the radial flux density at each layer of the yoke in order to obtain the total eddy current loss in the stator yoke.

From these observations, a simplified eddy current loss model for the stator yoke can be developed with the presence of a correction factor (k_r) to account for these variations [90].

$$P_{ey} = P_{eyc} + P_{eyr} = \frac{1}{\alpha}\frac{8}{\pi^2} k_e k_r \omega_s^2 \hat{B}_c^2 V_y \tag{6-18}$$

Where k_r is a correction factor accounting for the eddy current loss induced by the radial component of flux density in the stator yoke

$$k_r = 1 + k_y = 1 + \frac{8 k_q d_y^2}{27 \propto q \lambda_2^2} \tag{6-19}$$

Where;

k_y is the ratio of the loss induced by the two components of flux density in the stator yoke [90]

λ_2 is the slot pitch taken at the middle of the stator yoke

d_y is the depth of the stator yoke

Table 6-4: Eddy current loss - stator yoke

Yoke Eddy Current Loss Model Comparison	
k_r	1.05
FEM Yoke Eddy Current Loss (W)	311
Approx. Model Yoke Eddy Current Loss (W)	340
Error (%)	8.9

6.3.7. Hysteresis Loss Model

The hysteresis loss unlike the eddy current loss, only depends on the average of the plateau values of flux density from all the elements in the core. The hysteresis loss in the teeth and stator yoke can be calculated using (6-20) and (6-21) respectively [90]:

$$P_{ht} = k_h \omega_s B_{th}^{\beta} V_t = \frac{\pi np}{60} k_h B_{th}^{\beta} V_t \tag{6-20}$$

$$P_{hy} = k_h \omega_s B_{y}^{\beta} V_t = \frac{\pi np}{60} k_h B_{y}^{\beta} V_t \tag{6-21}$$

Where;

B_{th} is the tooth flux density

B_y is the yoke flux density

k_h is the hysteresis loss constant

β is the hysteresis loss coefficient

The table below shows a comparison between the loss calculated analytically and the loss obtained using FEM.

Table 6-5: Comparison of Hysteresis loss model with FEA

	Flux Density (T)	Volume (m^3)	Loss - FEA	Loss - Approx	% Error
Stator	1.45 peak (*varies*)	0.653e-03	182.17	169.60	6.9

The hysteresis loss calculated using the simplified model is comparable to the loss approximated using FEA with an acceptable error of 6.9 %. This error can further be reduced using a more accurate regression model for calculation of the hysteresis loss coefficient.

The table below shows the total core loss calculated analytically in comparison to FEA results.

Table 6-6: Comparison of overall core loss using analytical model

	Loss – Analytical (W)	Loss – FEA (W)	% Error
Overall Core Loss	637.60	673.06	5.3

The overall core loss estimation using the simplified analytical model gives an error of about 5.3 % when compared against the FEA estimation. This is in an acceptable range when compared to [90] and has proved to be valid for the estimation of core losses even at high frequencies.

Chapter 7

7 Prototyping of the High Speed SPM Machine

This chapter presents details of the construction of the high-speed surface mounted permanent magnet machine prototype. The main components of the machine include: the rotor, magnets, retaining sleeve, stator, winding and the housing unit. The prototype also included an oil lubrication system for the high-speed bearings and a chiller for cooling of the machine. This however, is not covered in this chapter as it is beyond the scope of this thesis.

The materials used for the prototype were carefully selected based on the application and desired electrical performance as discussed in chapter 2. A drawing section of the HS machine prototype is provided in Appendix B1.

7.1 Stator and Rotor Laminations

As mentioned earlier, M19 29G Silicon Steel was selected for the rotor and stator laminations. The laminations have a thickness of 0.36 mm each and were stacked over a length of 140 mm. The laminations are held together by means of spring clamps. Electro chemical machining (EMC) was used to cut the stator and rotor laminations. This is a high precision method and has proved to be more accurate than lazer cutting. It is based on the theory of electrolysis and works by means of anodic metal dissolution. The machining tool acts as the cathode (-) under a DC current and in the presence of an electrolyte fluid, creates an anodic reaction that cuts off the sheet of metal (+). The assembled rotor core is shown in Figure 7-1 below.

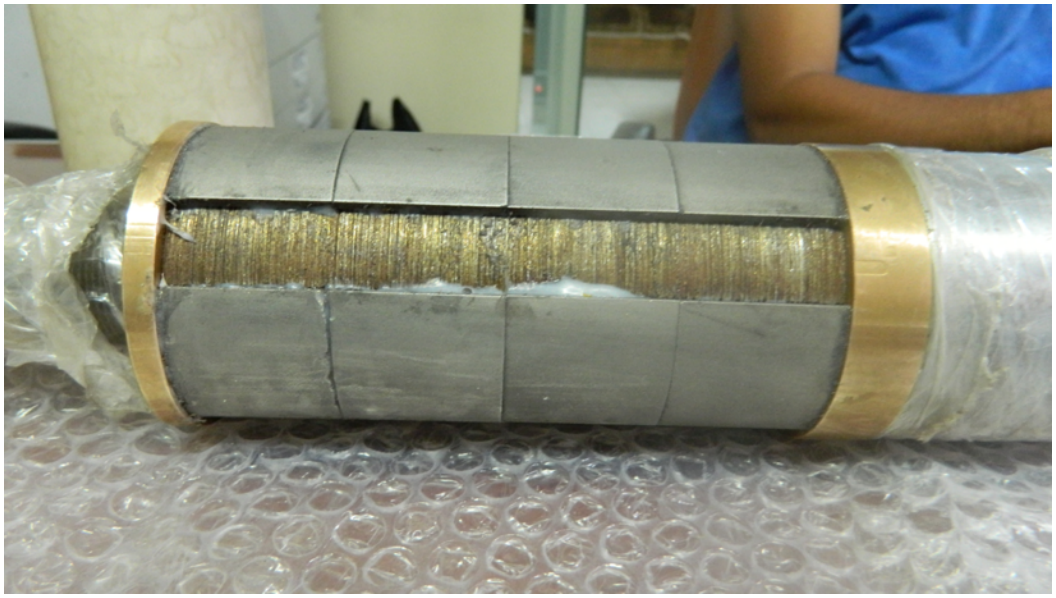

Figure 7-1: Assembled rotor core

As shown above, the magnets were fixed onto the surface of the rotor by a thin layer of epoxy glue and accurately positioned by means of prefabricated spacers. The magnets are grade N33 NdFeB PMs with parallel magnetization and are radially shaped with dimensions 60.03° radial span x 3.46mm thickness. They have a temperature withstand capability of 180 °C. The PMs were segmented to reduce the eddy current losses.

7.2 Stator Winding

An overlapping double layer winding configuration was employed for the high-speed SPM machine. Stranded litz wire was used for the winding in order to limit high frequency AC losses as a result of skin and proximity effects. The coils were twisted and hand-wound using a prefabricated fixture in order to maintain uniformity of the winding. The purpose of the fixture was to maintain a uniform shape and minimize the length of the end winding as it contributes to the final machine inductance.

Each coil consists of 15 strands of 0.776 mm diameter copper wire of insulation class H. The machine has 24 stator slots with 8 coils per phase and 2 turns per coil. The low number of turns is as a result of the machine's high operating frequency i.e. lower required flux linkage, as can be seen from equation (4-6). To monitor the winding temperatures, thermocouples were placed on the three phase windings as well as end-windings.

Figure 7-2: Stator winding

Figure 7-2: Stator winding shows the STAR connected stator winding of the 3 phase SPM machine with six terminal points i.e. 3 phase connections and a star/neutral point.

7.3 Machine Shaft

The machine shaft was manufactured from a high-grade stainless steel 415. A non-magnetic material was selected in order to avoid interference with the active magnetic circuit between the rotor and stator. As with all the other components of the machine, high precision was maintained and Quality Control (QC) reports submitted and verified at each stage of the machining process.

Figure 7-3: Machine shaft

A layer of epoxy was added in between the magnets and the retaining sleeve to provide extra retaining strength. The temperature capability of the epoxy was also taken into consideration to allow for adequate retaining strength even at high operating temperatures.

Figure 7-4: Complete rotor with shaft & retaining sleeve

Dynamic balancing was performed on the shaft and run-out measured. Balancing of the shaft was performed at various stages from initial assembly i.e. shaft alone, until complete assembly of the rotor body.

Figure 7-5 displays the dynamic balancing of the shaft.

Figure 7-5: Dynamic balancing of shaft

7.4 Housing Structure

The housing structure was constructed from FC20 Cast Iron. The most critical part of the construction process is the boring of the housing to accommodate the stator and rotor body. This requires precision machining as the interior part not only houses the stator & rotor body but the bearings, seals and other related assembly details.

Below is an image of the housing structure after successful casting.

Figure 7-6: Housing structure

A Computer Numerical Control (CNC) machine was used for precision machining of the interior parts of the housing structure. Round granule structure was maintained . This allows for easy scraping and also retains lubrication.

Hydraulic testing was also conducted on the housing structure to check for the presence of any holes or cracks in the housing structure. In most cases, presence of holes or cracks on the housing structure is as a result of a poor casting process. Figure 7-7 shows the housing structure undergoing pressure testing.

Figure 7-7: Pressure testing of housing structure

A maximum of 15 Bars was specified for the pressure test for a time period of 4-5 hours in increments of about 5 Bars of applied pressure. The specification for standard motor (low speed) housing is about 3 to 4 Bars. A high specification was necessary for this machine because of its nature of operation. A white dye was added to the water for easy identification of any leaks during the testing.

The housing body developed a crack across the cooling jackets after about 8 Bars of pressure applied. One of the major reasons could have been the presence of air pockets from the casting process. A cold welding compound (base material filling with epoxy) was used to fix the cracks along the housing and then ground down to sit flush with the housing walls. Due to safety concerns, it is recommended that a new housing body be manufactured to conduct tests at rated conditions.

Chapter 8

8 Prototype Testing

This section presents the experimental open circuit results from tests performed on the prototype machine up to 8,000 rpm. Testing could only be performed up to a maximum of 8,000 rpm due to limitations on the test rig and drive motor side as stated earlier in Section 1.5. This is outlined in detail in the limitations section of this report.

8.1 Stator Winding Coils

Each phase consists of 6 (six) coils connected in series to form the phase winding. Therefore, the resistance measured from each phase is simply an addition of the individual resistances of each coil for that particular phase. The SPM machine winding is STAR connected with four terminals i.e. 3 phases and a neutral point.

The phase resistances were measured with the aid of a galvanometer and compared to the analytical values.

	Measured (Ω)	**Calculated (Ω)**	**3D FEA (Ω)**
Phase A	0.0245	0.0207	0.0322
Phase B	0.0245	0.0207	0.0322
Phase C	0.0245	0.0207	0.0322

The measured values of resistance are equal for all three phases showing the presence of a balanced winding. However, a slight discrepancy exists between the measured and 3D FEA values. This is largely as a result of the end winding length.

8.1.1. Open Circuit Voltage

The open circuit voltages for all three phases are shown in Figure 8-1 below. The voltages were measured using a Yokagawa Power Analyser. U1, U2 and U3 represent phases A, B and C respectively and can be seen to be sinusoidal in shape and displaced by about 120°. It is evident that the voltages have a low harmonic content. An fft on the voltage waveforms was performed to further highlight the absence of significant harmonics.

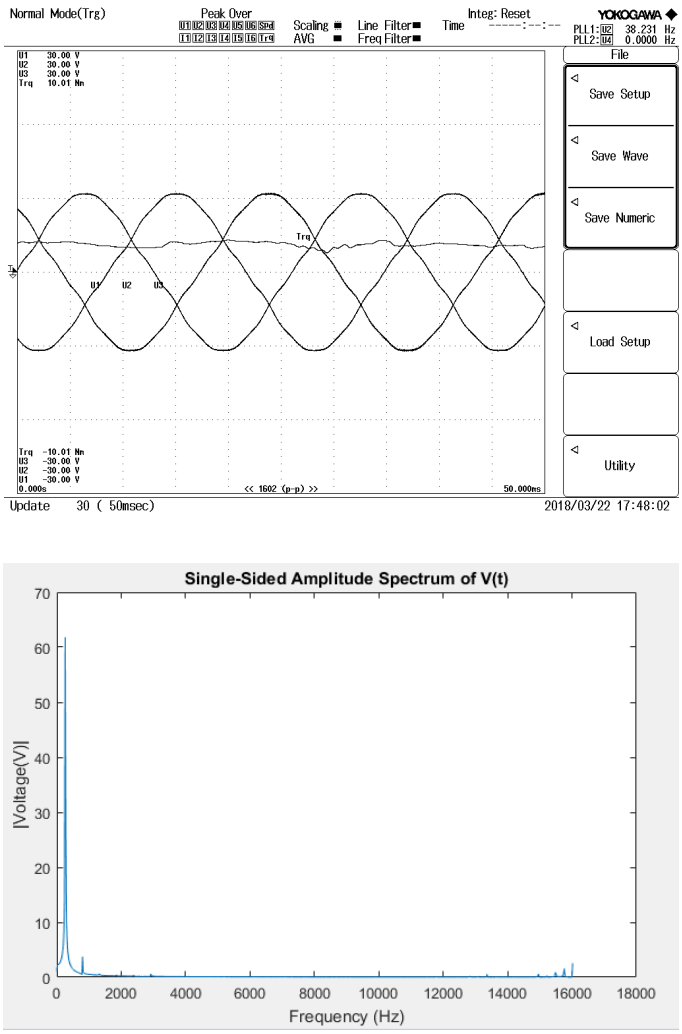

Figure 8-1: Open circuit voltage waveform and fft

To estimate the PM flux linkage of the machine, the variation of open circuit phase voltage with shaft speed was plotted as shown in Figure 8-2. The flux linkage is determined from the slope of the best-fit line to the data points.

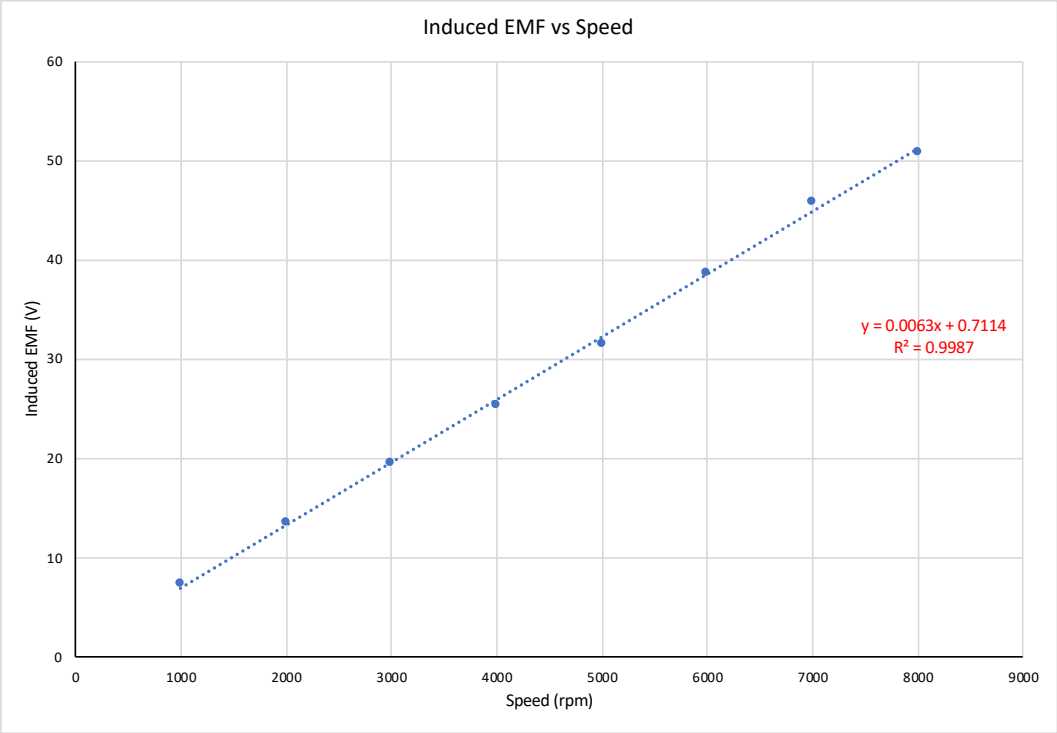

Figure 8-2: Induced EMF vs. rotational speed

From Figure 8-2, the estimated PM flux linkage from the slope of the best-fit line is 0.0063 Wb-turns. This is comparable to the values obtained analytically and using FEA with an acceptable percentage error.

Table 8-1: Comparison of PM flux linkage

	Experimental	Analytical	2D FEA
PM Flux Linkage (Wb-turns)	0.0063	0.0056	0.0069

Chapter 9

9 Conclusions and Recommendations

9.1 Conclusions

This dissertation discussed the electromagnetic design and analysis of a high-speed surface mounted PM machine including detailed sizing, analytical and FEA core loss modelling as well as construction of the machine prototype.

Based on the findings of this dissertation, the following conclusions are drawn:

9.1.1 The development of high-speed machines has seen an advancement in a number of research areas related to the design and development of these machines. Due to their high operational frequencies, these machines are exposed to various mechanical and electrical constraints. More specifically, high-speed machines have fostered the advancement of research in materials, bearing technology, cooling methods etc.

9.1.2 The competing topologies for use in high-speed applications include the induction machine and permanent magnet machine. However, more recently, preference has been given to PM machines for use in high-speed applications due to their simplistic design and operation, higher efficiency and power density, greater robustness and also the reduction in the price of permanent magnets. Other less common topologies include synchronous reluctance, switched reluctance and synchronous homopolar machines.

9.1.3 A detailed machine sizing procedure with emphasis on electromagnetic performance and mechanical integrity was outlined. Special consideration has to be given to the selection of material, winding design, the magnet retention system as well as minimization of the high-frequency losses. A 10 kW SPM machine was designed for a rated speed of 30,000 rpm. A reasonably high efficiency of 91% was achieved. The electromagnetic

performance obtained from FEA closely matched the analytical design values thereby validating the initial design of the machine. The maximum output power and torque was achieved as designed. A prototype was constructed as outlined in chapter 7 with an emphasis on the need for high-precision machining and maintaining high accuracies throughout the prototyping process. As a basis for future work which is beyond the scope of this thesis, basic no load tests were conducted on the machine prototype, that validated the initial design.

9.1.4 A number of core loss models are analysed in this thesis. A conclusion is drawn that, for the estimation of high-frequency core losses, the Steinmetz and classical formulae are inaccurate (0 – 30% error) at predicting high frequency losses. The error is dependent on the data and the method used to curve fit. Berttoti's three term model proves to be better than the Steinmetz two term model at estimating the core loss although is still inaccurate at flux densities beyond 1.3 T (> 20% error). A core loss model is also presented as an alternative to traditional core loss formulae for estimating core losses in machines. The model displays a good agreement between analytical and FEA data with an error range of about 3-11% for eddy current and hysteresis loss.

9.2 Recommendations

The following recommendations are made based on the findings of this dissertation:

9.2.1 To further validate the design of the machine, a high-speed test rig inclusive of the drive motor should be built to test the machine prototype at no load and full load conditions. The experimental results can then be compared against the analytical and FEA results.

9.2.2 In order to further improve the efficiency of the machine, an optimization algorithm should be developed for use during the design stage. The algorithm could look at altering various design parameters simultaneously to achieve a higher power density and efficiency, lower losses etc.

9.2.3 The accurate estimation of losses in the high-speed machine can be extended to the development of a thermal model for the accurate

prediction of temperatures within the machine. This will also allow for more efficient designs of the cooling system.

9.2.4 There is need to thoroughly investigate the estimation and measurement of mechanical losses in high-speed machines. Most of the work recorded in literature estimates the mechanical losses as a percentage of rated power. At high speeds, losses from drag and friction are more pronounced and need to be accurately estimated and measured.

References

[1] J. Byrne *et al.*, "Global Trends in Renewable Energy Investment 2016," Frankfurt, 2016.

[2] Turbec AB, "T100 Microturbine CHP System - Technical Description." Turbec AB, Malmo, Sweden, 2001.

[3] J. E. Rucker, "Design and Analysis of a Permanent Magnet Generator for Naval Applications," Massachusetts Institute of Technology, 2005.

[4] R. R. Moghaddam, "High Speed Operation of Electrical Machines, a Review on Technology, Benefits and Challenges," *2014 IEEE Energy Convers. Congr. Expo. ECCE 2014*, pp. 5539–5546, 2014.

[5] S. Li, Y. Li, W. Choi, and B. Sarlioglu, "High speed electric machines — Challenges and design considerations," *Electr. Mach. (ICEM), 2014 Int. Conf.*, pp. 2549–2555, 2014.

[6] W. Fengxiang, Z. Wenpeng, Z. Ming, W. Baoguo, B. Choice, and P. Number, "Design Considerations of High-speed PM Generators for Micro Turbines," pp. 158–162, 2002.

[7] C. Liu, J. Yu, and C. H. T. Lee, "A New Electric Magnetic-Geared Machine for Electric Unmanned Aerial Vehicles," vol. 53, no. 11, 2017.

[8] A. Borisavljevic, *Limits, Modeling and Design of High-Speed Permanent Magnet Machines*. Berlin, Heidelberg: Springer Berlin Heidelberg, 2013.

[9] J. B. Bartolo, H. Zhang, D. Gerada, L. De Lillo, and C. Gerada, "High speed electrical generators, application, materials and design," *Proc. - 2013 IEEE Work. Electr. Mach. Des. Control Diagnosis, WEMDCD 2013*, pp. 47–59, 2013.

[10] Z. Kolondzovski, A. Arkkio, J. Larjola, and P. Sallinen, "Power limits of high-speed permanent-magnet electrical machines for compressor applications," *IEEE Trans. Energy Convers.*, vol. 26, no. 1, pp. 73–82, 2011.

[11] Y. Hu, T. Wu, L. Chow, Y. Bai, and W. Wu, "Design of a 3kW 150k RPM

Super High-Speed Permanent Magnet Synchronous Motor," pp. 2543–2548, 2014.

[12] E. Richter and C. Ferreira, "Performance evaluation of a 250 kW switched reluctance starter generator," *IAS '95. Conf. Rec. 1995 IEEE Ind. Appl. Conf. Thirtieth IAS Annu. Meet.*, vol. 1, 1995.

[13] L. Morel, H. Fayard, R. Vives Fos, A. Galindo, and G. Abba, "Study of ultra high speed switched reluctance motor drive," *Ind. Appl. Conf.*, pp. 87–92, 2000.

[14] D. K. Hong, J. H. Choi, D. J. Kim, Y. Do Chun, B. C. Woo, and D. H. Koo, "Development of a high speed induction motor for spindle systems," *IEEE Trans. Magn.*, vol. 49, no. 7, pp. 4088–4091, 2013.

[15] D. Gerada, A. Mebarki, M. Shanel, K. J. Bradley, and N. L. Brown, "Design Considerations of High-Speed Induction Machines for High-Temperature Applications," pp. 1–6, 2008.

[16] M. a. Rahman, a. Chiba, and T. Fukao, "Super high speed electrical machines - summary," *IEEE Power Eng. Soc. Gen. Meet. 2004.*, vol. 1, no. iii, pp. 1–4, 2004.

[17] A. Maeda and H. Tomita, "Power and Speed Limitations in High Speed Electrical Machines," *IPEC*, pp. 1321–1326, 1995.

[18] D. Gerada, A. Mebarki, N. L. Brown, C. Gerada, A. Cavagnino, and A. Boglietti, "High-speed electrical machines: Technologies, trends, and developments," *IEEE Trans. Ind. Electron.*, vol. 61, no. 6, pp. 2946–2959, 2014.

[19] a. Arkkio, T. Jokinen, and E. Lantto, "Induction and permanent-magnet synchronous machines for high-speed applications," *2005 International Conference on Electrical Machines and Systems*, vol. 2. pp. 1–6, 2005.

[20] J. R. Bumby, E. Spooner, and M. Jagiela, "Solid Rotor Induction Machines for Use in Electrically-Assisted Turbochargers," *PEMD*, pp. 341–345, 2006.

[21] H. Zhou and F. Wang, "Comparative Study on High speed Induction Machine with Different Rotor Structures," no. c, pp. 1009–1012, 2007.

[22] J. Lahteenmaki, “Design and voltage supply of high-speed induction machines,” Helsinki Univ. Technol, 2002.

[23] A. Binder and T. Schneider, “High-speed inverter-fed AC drives,” *Int. Aegean Conf. Electr. Mach. Power Electron. Electromotion ACEMP’07 Electromotion’07 Jt. Conf.*, pp. 9–16, 2007.

[24] Y. Honda, S. Yokote, T. Higaki, and Y. Takeda, “Using the Halbach magnet array to develop an ultrahigh-speed\nspindle motor for machine tools,” *IAS ’97. Conf. Rec. 1997 IEEE Ind. Appl. Conf. Thirty-Second IAS Annu. Meet.*, vol. 1, no. mm, 1997.

[25] A. Borisavljević, *Limits, Modeling and Design of High-Speed Permanent Magnet Machines_Thesis*. 2011.

[26] E. W. Fairall, S. Member, B. Bilgin, and A. Emadi, “State-of-the-Art High-Speed Switched Reluctance Machines,” pp. 1–7, 2015.

[27] J. F. Gieras, “Comparison of High-Power High-Speed Machines: Cage Induction versus Switched Reluctance Motors,” *1999 IEEE Africon. 5th Africon Conf. Africa (Cat. No.99CH36342)*, vol. 2, pp. 675–678, 1999.

[28] T. J. E. Miller, *Brushless Permanent-Magnet and Reluctance Motor Drives (Monographs in Electrical and Electronic Engineering 21)*, no. 21. 1989.

[29] F. Cupertino, M. Palmieri, and G. Pellegrino, “Design of high-speed synchronous reluctance machines,” in *2015 IEEE Energy Conversion Congress and Exposition (ECCE)*, 2015, pp. 4828–4834.

[30] J. Ikaheimo, J. Kolehmainen, T. Kansakangas, V. Kivela, and R. R. Moghaddam, “Synchronous high-speed reluctance machine with novel rotor construction,” *IEEE Trans. Ind. Electron.*, vol. 61, no. 6, pp. 2969–2975, 2014.

[31] H. Hofmann and S. R. Sanders, “High-speed synchronous reluctance machine with minimized rotor losses,” *IEEE Trans. Ind. Appl.*, vol. 36, no. 2, pp. 531–539, 2000.

[32] M.-I. Lamghari-Jamal, J. Fouladgar, E.-H. Zaim, and D. Trichet, “A magneto-thermal study of a high-speed synchronous reluctance machine,” *IEEE Trans. Magn.*, vol. 42, no. 4, pp. 1271–1274, Apr. 2006.

[33] M. Palmieri, M. Perta, and F. Cupertino, “Design of a 50 000 rpm Synchronous Reluctance Machine for an Aeronautic Diesel Engine Compressor,” *IEEE Energy Convers. Congr. Expo.*, vol. 52, no. 5, pp. 5138–5143, 2014.

[34] P. Tsao, M. Senesky, and S. Sanders, “A synchronous homopolar machine for high-speed applications,” *Conf. Rec. 2002 IEEE Ind. Appl. Conf. 37th IAS Annu. Meet. (Cat. No.02CH37344)*, vol. 1, pp. 406–416, 2002.

[35] W. Li, K. T. Chau, T. W. Ching, Y. Wang, and M. Chen, “Design of a high-speed superconducting bearingless machine for flywheel energy storage systems,” *IEEE Trans. Appl. Supercond.*, vol. 25, no. 3, pp. 5–8, 2015.

[36] S. Gillette, “Microturbine Technology Matures,” *Power Magazine*, 2010. [Online]. Available: http://www.powermag.com/microturbine-technology-matures/?pagenum=1. [Accessed: 23-Dec-2016].

[37] J. F. Gieras, *Advancements in Electric Machines*, vol. 53, no. 9. 2013.

[38] J. Dong, Y. Huang, L. Jin, H. Lin, and H. Yang, “Thermal optimization of a high-speed permanent magnet motor,” *IEEE Trans. Magn.*, vol. 50, no. 2, pp. 3–6, 2014.

[39] N. Bianchi, S. Bolognani, and F. Luise, “Potentials and limits of high speed PM motors,” *38th IAS Annu. Meet. Conf. Rec. Ind. Appl. Conf. 2003.*, vol. 3, no. 6, pp. 1570–1578, 2003.

[40] R. Abebe, M. Di Nardo, D. Gerada, G. Lo Calzo, L. Papini, and C. Gerada, “High speed drives review: Machines, converters and applications,” *IECON 2016 - 42nd Annu. Conf. IEEE Ind. Electron. Soc.*, pp. 1675–1679, 2016.

[41] J. Wang, Z. Sun, J. D. Ede, G. W. Jewell, J. J. A. Cullen, and A. J. Mitcham, “Testing of a 250-Kilowatt Fault-Tolerant Permanent Magnet Power Generation System for Large Civil Aeroengines,” *J. Propuls. Power*, vol. 24, no. 2, pp. 330–335, Mar. 2008.

[42] B. Frieske, M. Kloetzke, and F. Mauser, “Trends in Vehicle Concept and Key Technology Development for Hybrid and Battery Electric Vehicles,” pp. 1–12, 2013.

[43] UNEP, “Hybrid Electric Vehicles,” 2009.

[44] K. Senda, M. Namikawa, and Y. Hayakawa, “Electrical Steels for Advanced Automobiles — Core Materials for Motors , Generators , and High-Frequency Reactors,” *JFE Tech. Rep.*, vol. 4, no. 4, pp. 67–73, 2004.

[45] R. Hasegawa, “Applications of Amorphous Magnetic Alloys,” in *Properties and Applications of Nanocrystalline Alloys from Amorphous Precursors*, 2005, pp. 189–198.

[46] N. Ertugrul, R. Hasegawa, W. L. Soong, J. Gayler, S. Kloeden, and S. Kahourzade, “A Novel Tapered Rotating Electrical Machine Topology Utilizing Cut Amorphous Magnetic Material,” vol. 51, no. 7, 2015.

[47] S. Constantinides, “Rare Earth Materials Update,” in *SMMA Management Conference*, 2011.

[48] D. Gerada, A. Mebarki, and C. Gerada, “Optimal design of a high speed concentrated wound PMSM,” *Proc. - 12th Int. Conf. Electr. Mach. Syst. ICEMS 2009*, 2009.

[49] Bruker EST, “Cupronal Information Sheet,” *Bruker*, 2013. [Online]. Available: http://www.bruker-est.com/he-cuponal.html. [Accessed: 23-Jan-2017].

[50] K. S. Boutros, R. Chu, and B. Hughes, “GaN Power Electronics for Automotive Applications,” *IEEE Energytech*, pp. 1–4, 2012.

[51] P. Imoberdorf, C. Zwyssig, S. D. Round, and J. W. Kolar, “Combined Radial-Axial Magnetic Bearing for a 1kW, 500,000 rpm Permanent Magnet Machine,” pp. 1434–1440, 2007.

[52] A. Binder, “Tutorial ‘High Speed Drives,’” in *ICEM*, 2014.

[53] A. Looser and J. W. Kolar, “A Hybrid Bearing Concept for High-Speed Applications Employing Aerodynamic Gas-Bearings and a Self-Sensing Active Magnetic Damper,” pp. 1686–1691, 2011.

[54] M. Salehi, H. Heshmat, J. F. Walton, and M. Tomaszewski, “Operation of a Mesoscopic Gas Turbine Simulator at Speeds in Excess of 700,000 rpm on Foil Bearings,” *J. Eng. Gas Turbines Power*, vol. 129, no. 1, p. 170, 2007.

[55] B. Polajzer, “Design and analysis of an active magnetic bearing experimental

system," University of Maribor, 2002.

[56] T. Schneider and A. Binder, "Design and Evaluation of a 60000 rpm Permanent Magnet Bearingless High Speed Motor," *J. Sci. Instrum.*, Mar. 2007.

[57] X. Sun, L. Chen, and Z. Yang, "Overview of bearingless permanent-magnet synchronous motors," *IEEE Trans. Ind. Electron.*, vol. 60, no. 12, pp. 5528–5538, 2013.

[58] A. Salazar, A. Chiba, and T. Fukao, "A Review of Developments in Bearingless Motors," in *7th International Symposium on Magnetic Bearings*, 2000.

[59] V. Kluyskens and B. Dehez, "Dynamic Electromechanical Model for Magnetic Bearings Subject to Eddy Currents," *IEEE Trans. Magn.*, no. 4, pp. 1444–1452, 2013.

[60] M. Y. Chen, S. C. Huang, S. K. Hung, and L. C. Fu, "Design and implementation of a new six-DOF Maglev positioner with a fluid bearing," *IEEE/ASME Trans. Mechatronics*, vol. 16, no. 3, pp. 449–458, 2011.

[61] K. J. Binns, M. S. N. Al-Din, and P. J. G. Lisboa, "Use of canned rotors in high-field permanent magnet machines," *Electr. Power Appl. IEE Proc. B*, vol. 139, no. 5, pp. 471–477, 1992.

[62] Z. Kolondzovski, a. Belahcen, and a. Arkkio, "Comparative thermal analysis of different rotor types for a high-speed permanent-magnet electrical machine," *IET Electr. Power Appl.*, vol. 3, no. 4, p. 279, 2009.

[63] F. Zhang, G. Du, T. Wang, G. Liu, and W. Cao, "Rotor Retaining Sleeve Design for a 1.12-MW High-Speed PM Machine," *IEEE Trans. Ind. Appl.*, vol. 51, no. 5, pp. 3675–3685, Sep. 2015.

[64] H. W. Cho, S. M. Jang, and S. K. Choi, "A design approach to reduce rotor losses in high-speed permanent magnet machine for turbo-compressor," *IEEE Trans. Magn.*, vol. 42, no. 10, pp. 3521–3523, 2006.

[65] F. Zhou, J. Shen, W. Fei, and R. Lin, "Study of Retaining Sleeve and Conductive Shield and Their Influence on Rotor Loss in High-Speed PM BLDC Motors," *IEEE Trans. Magn.*, vol. 42, no. 10, pp. 3398–3400, Oct. 2006.

[66] J. Herbst, J. Hahne, H. Jordan, H. Liu, A. Gattozzi, and Ben Wu, “Challenges in the design of a 100 kw induction motor for a PHEV application,” in *2009 IEEE Vehicle Power and Propulsion Conference*, 2009, pp. 408–413.

[67] D. C. Hanselman, *Brushless permanent magnet motor design*, 2nd Editio. Lebanon: Magna Physics Publications, 2006.

[68] M. Aydin, “Magnet skew in cogging torque minimization of axial gap permanent magnet motors,” in *2008 18th International Conference on Electrical Machines*, 2008, pp. 1–6.

[69] F. G. Capponi, G. De Donato, and F. Caricchi, “Recent Advances in Axial-Flux Permanent-Magnet Machine Technology,” vol. 48, no. 6, pp. 2190–2205, 2012.

[70] A. Cavagnino, M. Lazzari, F. Profumo, S. Member, and A. Tenconi, “A Comparison Between the Axial Flux and the Radial Flux Structures for PM Synchronous Motors,” vol. 38, no. 6, pp. 1517–1524, 2002.

[71] A. Parviainen, “Performance comparison between low-speed axial-flux and radial-flux permanent- magnet machines including mechanical constraints,” pp. 1695–1702, 2005.

[72] D. J. Patterson, J. L. Colton, B. Mularcik, B. J. Kennedy, S. Camilleri, and R. Rohoza, “A Comparison of Radial and Axial Flux Structures in Electrical Machines,” *IEMDC*, pp. 1029–1035, 2009.

[73] R. Qu, M. Aydin, and T. A. Lipo, “Performance Comparison of Dual-Rotor Radial-Flux and Axial-Flux Permanent-Magnet BLDC Machines,” pp. 1948–1954, 2003.

[74] A. Chen, R. Nilssen, A. Nysveen, and S. Member, “Performance Comparisons Among Radial-Flux , Transverse-Flux PM Machines for Downhole Applications,” vol. 46, no. 2, pp. 779–789, 2010.

[75] N. Bianchi and S. Bolognani, “Design techniques for reducing the cogging torque in surface-mounted PM motors,” *IEEE Trans. Ind. Appl.*, vol. 38, no. 5, pp. 1259–1265, 2002.

[76] A. Binder, T. Schneider, and M. Klohr, “Fixation of buried and surface-mounted magnets in high-speed permanent-magnet synchronous machines,”

IEEE Trans. Ind. Appl., vol. 42, no. 4, pp. 1031–1037, 2006.

[77] J. Kang, "General Purpose Permanent Magnet Motor Drive without Speed and Position Sensor," *Emsdrives.Com*, 2009.

[78] T. A. Lipo, *Introduction to AC Machine Design*, 3rd ed. New York, United States: John Wiley & Sons Inc, 2017.

[79] H. Dogan, S. Member, F. Wurtz, A. Foggia, and L. S. Member, "Analysis of Slot-Pole Combination of Fractional-Slots PMSM for Embedded Applications," no. May 2014, 2011.

[80] J. R. Hendershot and T. J. E. Miller, *Design of Brushless Permanent-Magnet Motors*. Magna Physics Publications, 1994.

[81] A. El Shahat, A. Keyhani, and H. El Shewy, "Sizing a high speed PM generator for green energy applications," *Journal of Electrical Systems*, vol. 6, no. 4. pp. 501–516, 2010.

[82] B. Sarlioglu, T. Jahns, and D. Ionel, "Design and Manufacturing of PM Electrical Machines," in *IEEE Energy Conversion Congress and Exposition (ECCE)*, 2015.

[83] J. F. Gieras, *Permanent Magnet Motor Technology*, Third Edit. Taylor and Francis Group, LLC, 2010.

[84] M. A. Khan, "Contribution to permanent magnet wind generator design including the application of soft magnetic comositions," no. August, 2006.

[85] T. J. E. Miller and D. A. Staton, *Electric Machine Design Using Speed and Motor-CAD*. Glasgow: Motor Design Limited, 2013.

[86] Infolytica Corporation, "MotorSolve BLDC," 2015. [Online]. Available: http://www.infolytica.com/secured/customer/elite/livedocs/MotorSolveBLDC/. [Accessed: 03-Jun-2015].

[87] W. Q. Chu and Z. Q. Zhu, "Reduction of on-load torque ripples in permanent magnet synchronous machines by improved skewing," *IEEE Trans. Magn.*, vol. 49, no. 7, pp. 3822–3825, 2013.

[88] J. J. H. Paulides, G. W. Jewell, and D. Howe, "An Evaluation of Alternative

Stator Lamination Materials for a High Speed, 1.5 MW, Permanent Magnet Generator," *IEEE Trans. Magn.*, vol. 40, no. 4, pp. 2041–2043, 2004.

[89] Y. Chen and P. Pillay, "An Improved Formula for Lamination Core Loss Calculations in Machines Operating with High Frequency and High Flux Density Excitation," pp. 759–766, 2002.

[90] C. Mi, G. R. Slemon, and R. Bonert, "Modeling of Iron Losses of Permanent-Magnet Synchronous Motors," *IEEE Trans. Ind. Appl.*, vol. 39, no. 3, pp. 734–742, 2003.

[91] G. R. Slemon, "CORE LOSSES IN PERMANENT MAGNET MOTORS," vol. 26, no. 5, pp. 1653–1655, 1990.

[92] G. Bertotti, "General properties of power losses in soft ferromagnetic materials," *IEEE Trans. Magn.*, vol. 24, no. 1, pp. 621–630, 1998.

Appendix A

A.1. Calculation of Slot leakage permeance

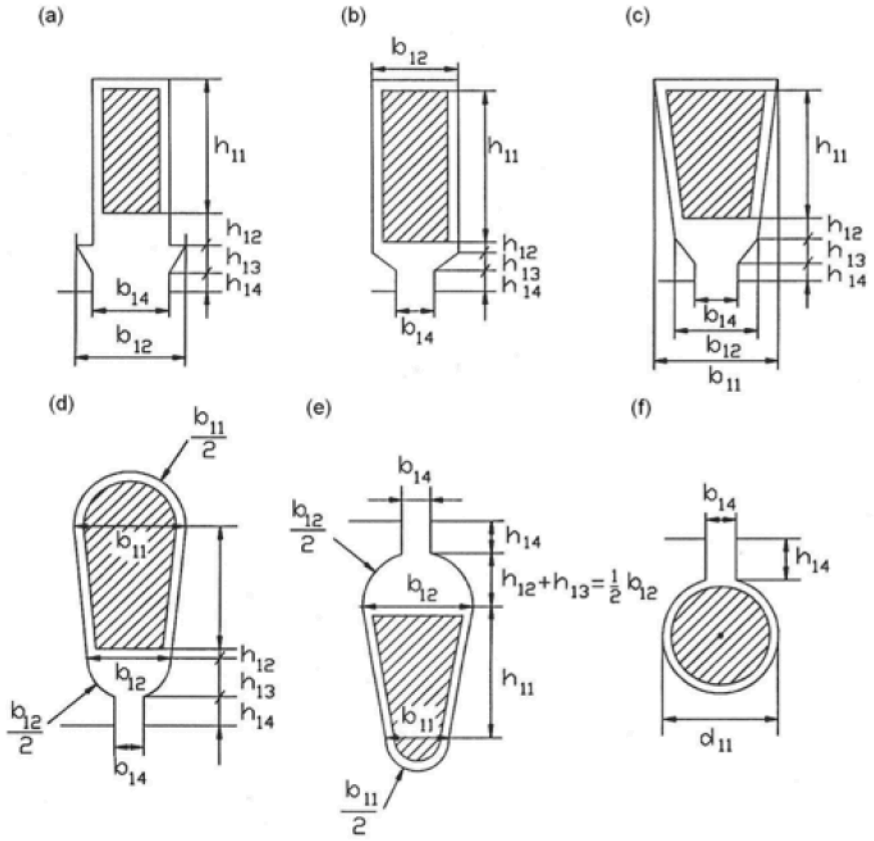

Figure A-1: *Stator slots (a) open rectangular slot (b) semi-closed rectangular slot (c) semi-closed trapezoidal slot (d) semi-closed oval slot (e) semi-closed oval slot for internal stators (f) semi-closed round slot*

Appendix B

B.1. Mechanical Drawings

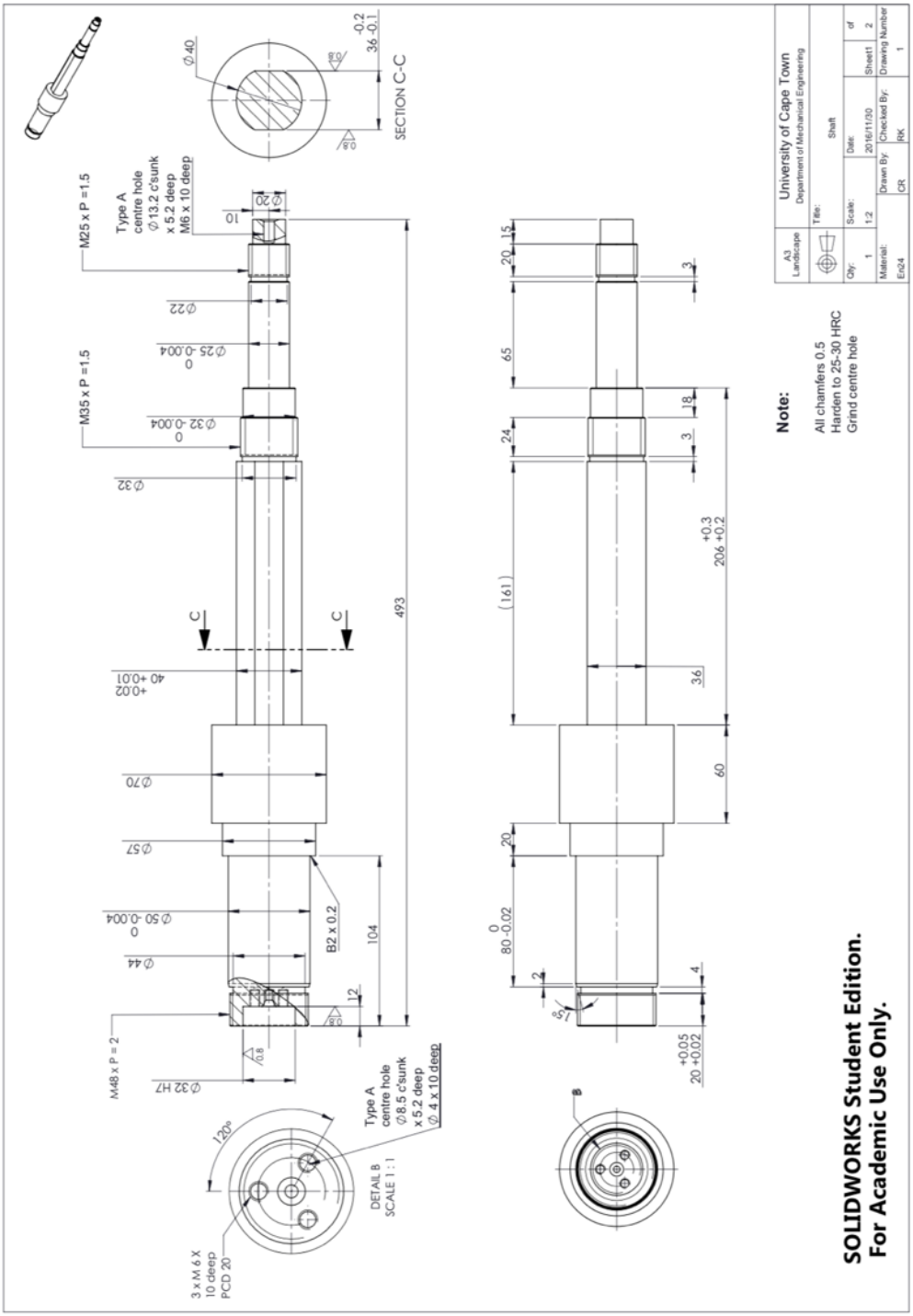

Figure B-1: *Shaft assembly*

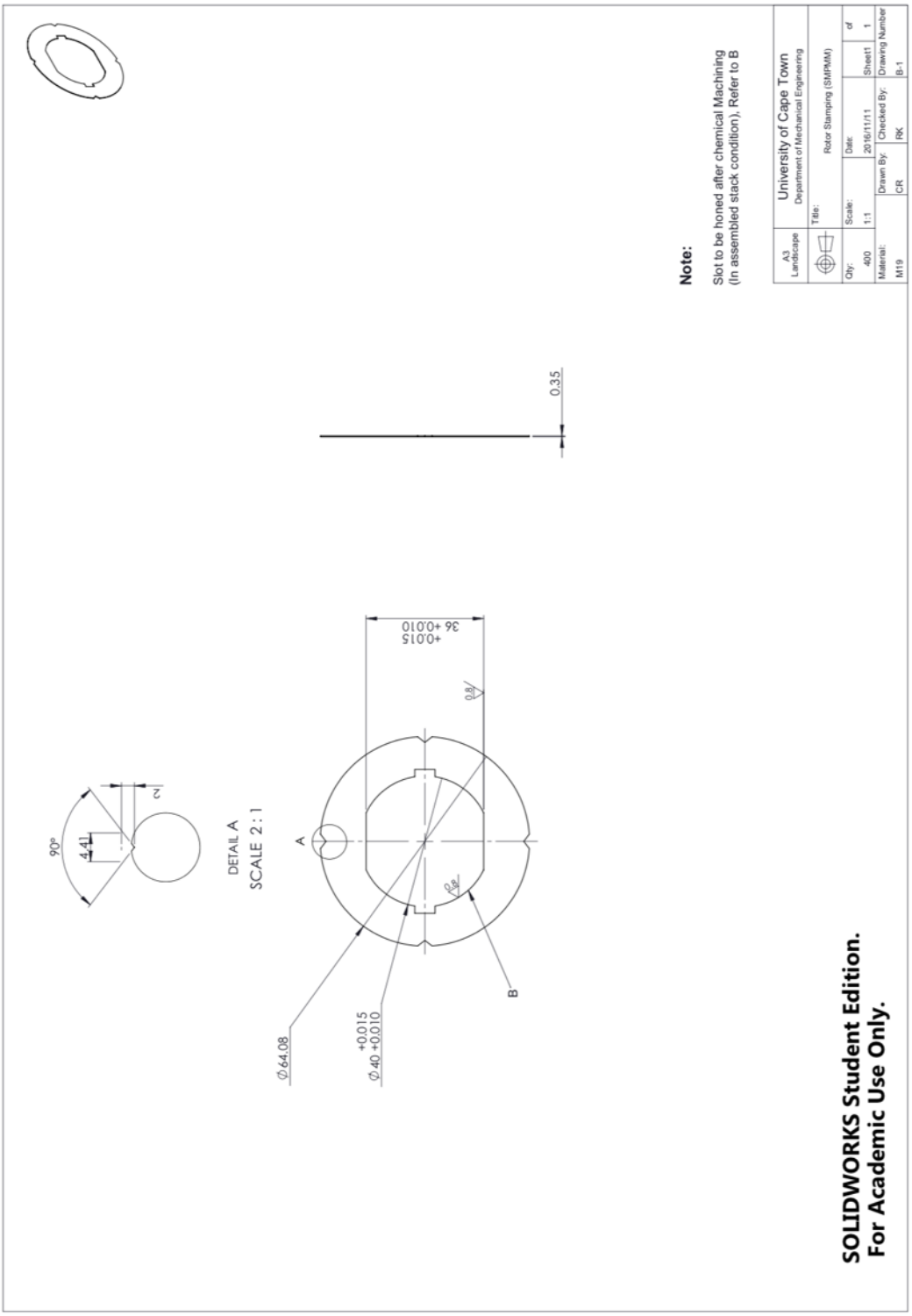

Figure B-2: *Rotor laminations*

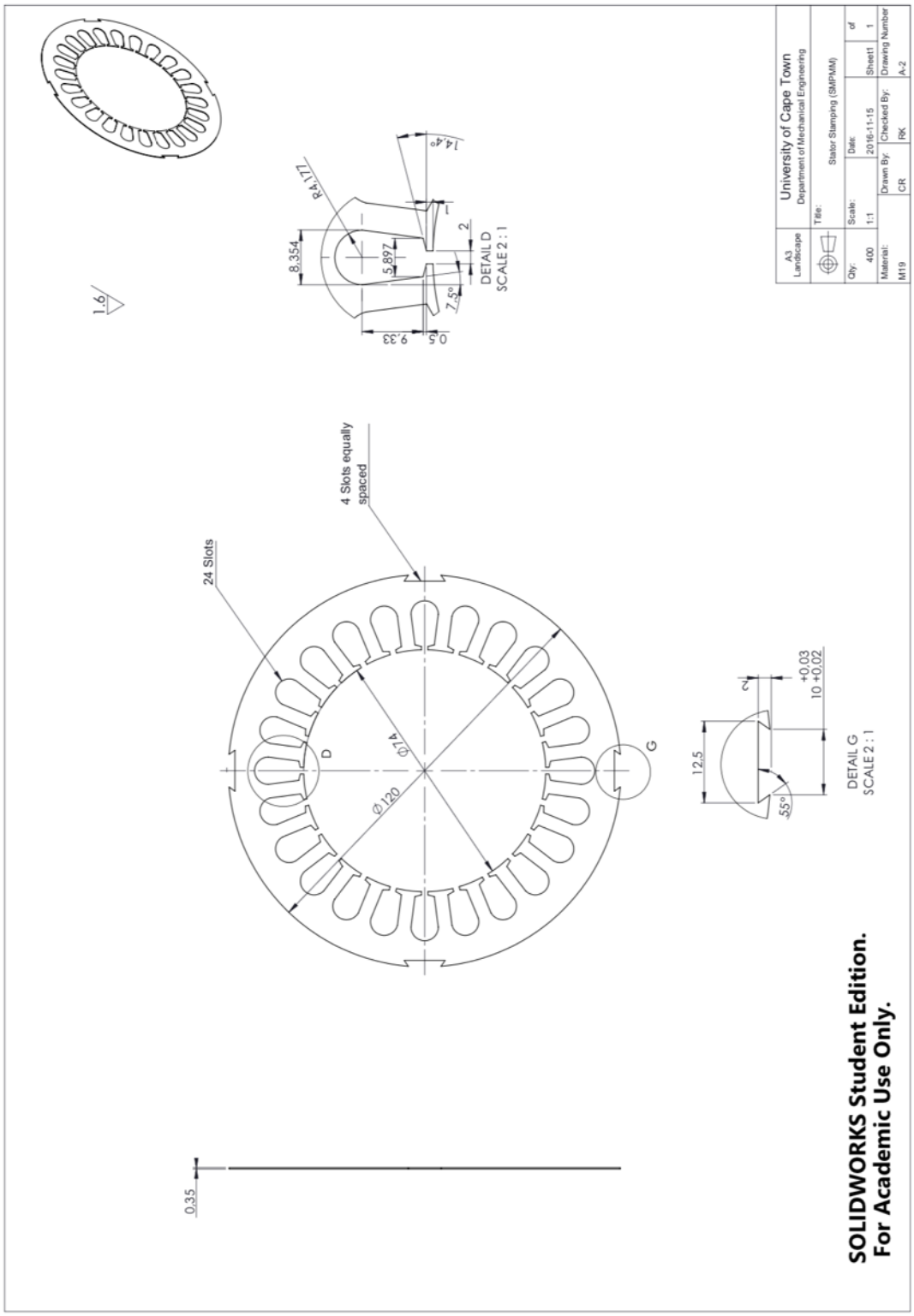

Figure B-3: *Stator laminations*

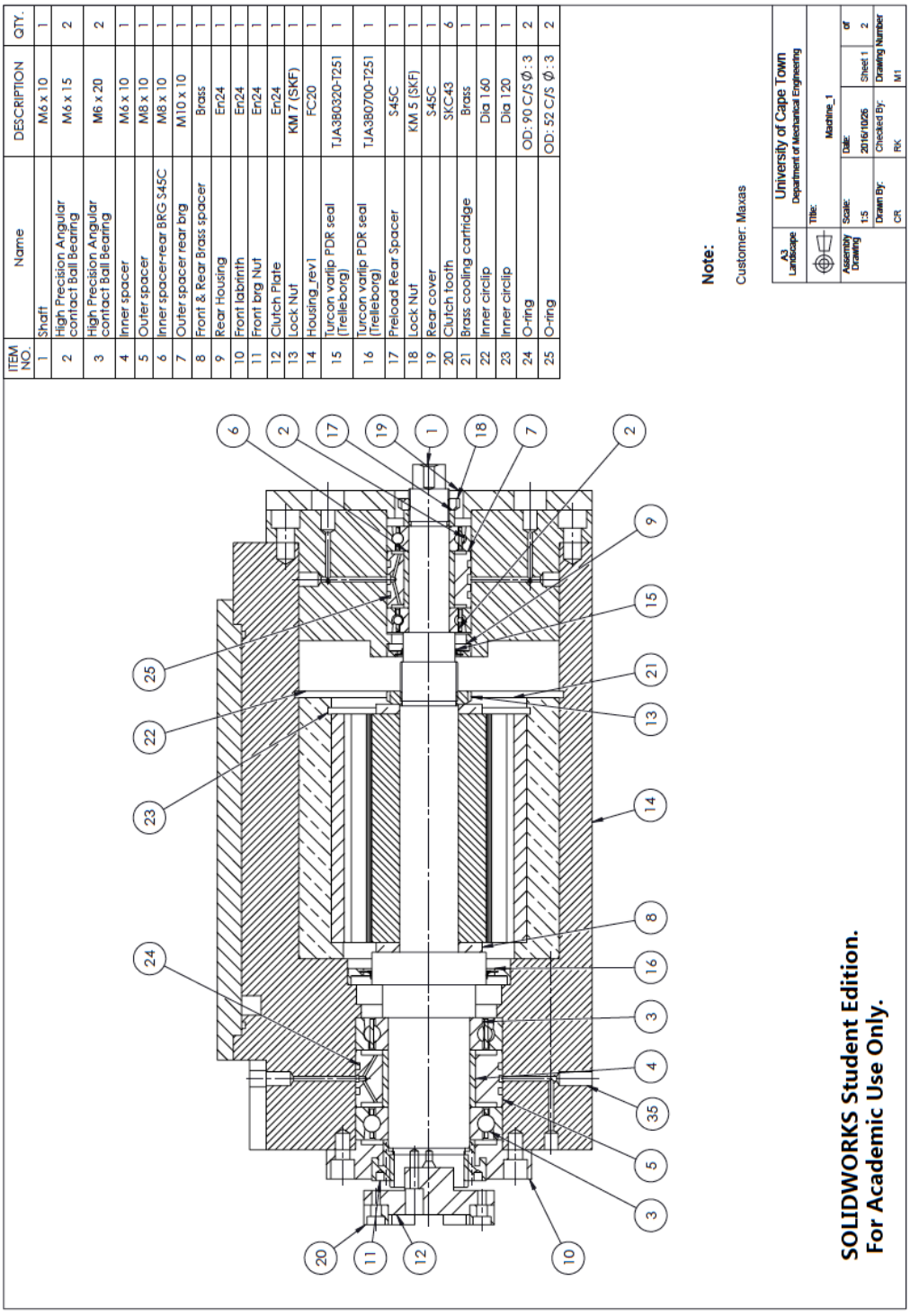

Figure B-4: *HS Machine Prototype – Drawing Section*

4. Installation

4.1 Layout & terminal points

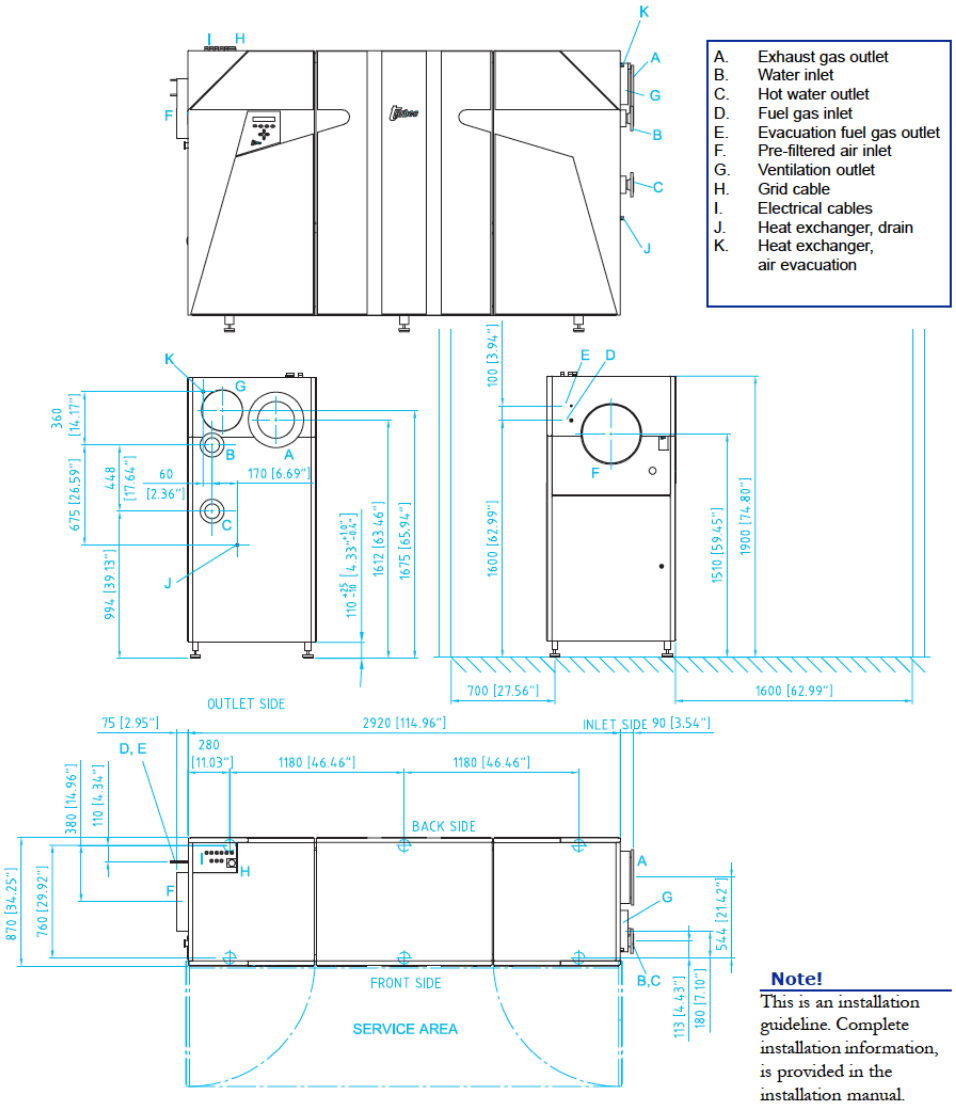

Figure B-5: CHP System Dimensions

Assessment of Ethics in Research Projects

Application for Approval of Ethics in Research (EiR) Projects
Faculty of Engineering and the Built Environment, University of Cape Town

APPLICATION FORM

Please Note:
Any person planning to undertake research in the Faculty of Engineering and the Built Environment (EBE) at the University of Cape Town is required to complete this form **before** collecting or analysing data. The objective of submitting this application *prior* to embarking on research is to ensure that the highest ethical standards in research, conducted under the auspices of the EBE Faculty, are met. Please ensure that you have read, and understood the **EBE Ethics in Research Handbook** (available from the UCT EBE, Research Ethics website) prior to completing this application form: http://www.ebe.uct.ac.za/ebe/research/ethics1

APPLICANT'S DETAILS		
Name of principal researcher, student or external applicant		MAXAS NG'ONGA
Department		ELECTRICAL ENGINEERING
Preferred email address of applicant:		ngnmax001@myuct.ac.za
If Student	Your Degree: e.g., MSc, PhD, etc.	MSc
	Credit Value of Research: e.g., 60/120/180/360 etc.	180
	Name of Supervisor (if supervised):	PROF. AZEEM KHAN
If this is a researchcontract, indicate the source of funding/sponsorship		
Project Title		DESIGN, PROTOTYPING & TESTING OF A HIGH-SPEED SURFACE MOUNTED PERMANENT MAGNET GENERATOR

I hereby undertake to carry out my research in such a way that:

- there is no apparent legal objection to the nature or the method of research; and
- the research will not compromise staff or students or the other responsibilities of the University;
- the stated objective will be achieved, and the findings will have a high degree of validity;
- limitations and alternative interpretations will be considered;
- the findings could be subject to peer review and publicly available; and
- I will comply with the conventions of copyright and avoid any practice that would constitute plagiarism.

SIGNED BY	Full name	Signature	Date
Principal Researcher/ Student/External applicant	MAXAS NG'ONGA	Signed by candidate	**16 Nov 2017**

APPLICATION APPROVED BY	Full name	Signature	Date
Supervisor (where applicable)	PROF. AZEEM KHAN		**16 Nov 2017**
HOD (or delegated nominee) Final authority for all applicants who have answered NO to all questions in Section1; and for all Undergraduateresearch (Including Honours).	S. CHOWDHURY	Sinalo Chaudhury	8/12/17
Chair : Faculty EIR Committee For applicants other than undergraduate students who have answered YES to any of the above questions.			

Page 1 of 2